Surface engineering of multi-functional coatings to enhance the electrochemical performance

by

Mao-Chia Lin

A dissertation submitted to the Graduate Faculty of
Auburn University
in partial fulfillment of the
requirements for the Degree of
Doctor of Philosophy

Auburn, Alabama
May 6, 2023

Keywords: polypyrrole, corrosion, electrochemistry, DNA biosensor, microwave, surface engineering

Approved by

Xinyu Zhang, Chair, Professor, Chemical Engineering
Andrew Adamczyk, Assistant Professor, Chemical Engineering
Tae-Sik Oh, Assistant Professor, Chemical Engineering
Russell Mailen, Assistant Professor, Aerospace Engineering
Siyuan Dai, Assistant Professor, Mechanical Engineering

Abstract

The electrochemical behavior of functionalized composite for surface engineering and its application is described in this dissertation. The research work includes electropolymerization, microwave synthesis, characterization, and examination of prepared materials. Corrosion is a spontaneous procedure and unpreventable. The hexavalent chromate Cr^{6+} had been a promising corrosion inhibitor and the very first application can be tracked back to 1915. However, due to the negative impact on the environment and health, the use of the chromate compound had been limited. Therefore, searching for alternative materials to replace the hexavalent chromate Cr^{6+} becomes very important. Among the abundance of potential materials, conducting polymer attracts attention because of its unique characteristics.

The electrodeposition of polypyrrole onto copper and aluminum alloy was achieved by potentiostatic electropolymerization in the first section. In the first project, the passivation ability of oxalic acid and sodium salicylate for copper was studied, and then the corrosion protection efficiency. In addition, in order to improve the binding ability of the polypyrrole film, tannic acid was introduced as the adhesion promoter into the electro- polymerization process. The effect of tannic acid was demonstrated by promoting adhesion from 0B to 3B and improving the corrosion protection efficiency by 30 %. A coating with good adhesion can prevent the delamination of the protective layer and restrict the spread of the corrosive ions. The best result from each dopant was incorporated with tannic acid for improving the adhesion and anti-corrosion performance. For the second project, the aluminum alloy was investigated by the same process and intended to investigate the effect of dopants that contains the sulfonate group for electropolymerization of polypyrrole. The results illustrated that surfactant-liked dopants facilitated electrodeposition. In

addition, the dopant with a larger chemical structure provided better protection efficiency. The application of a spray paint topcoat to the entire system can result in even better protection performance. This is because the topcoat acts as a barrier, effectively preventing the penetration of aggressive ions.

In 2020, the outbreak of COVID-19 blows the whole world heavily. While people are taking measures to protect themselves from getting infected by a virus, it is also essential to improve the ability to detect the virus in people who may already be infected but are not showing symptoms. Early detection of the virus can help to prevent the further spread of the virus by allowing infected individuals to receive proper medical care and quarantine measures. This can also help identify potential outbreaks and take appropriate measures to prevent them from spreading further. So, improving the ability to detect the virus is an important aspect of managing and controlling the spread of infectious diseases. The third project focused on the development of a DNA biosensor for the detection of COVID-19. We utilized a hybrid material made from ZnS and graphene, which was prepared using a non-equilibrium heating approach based on microwave technology. The biosensor was then tested using synthetic DNA samples as well as standard samples of the SARS-CoV-2 virus. The results of the study showed that the ZnS/G hybrid material was highly effective in detecting low concentrations of the virus. The biosensor was also found to be highly sensitive, meaning it could accurately detect even small amounts of the virus. The use of microwave-based synthesis techniques allowed for the creation of a highly efficient biosensor that could be used for early and accurate detection of COVID-19. This research has potential implications for the development of improved methods for diagnosing and monitoring infectious diseases.

Acknowledgments

Firstly, I would like to express my sincere gratitude to my advisor Dr. Xinyu Zhang for his continuous support throughout my doctoral study, and for his patience, motivation, enthusiasm, and immense knowledge. His advice helped me all along of my Ph.D. research.

I would like to acknowledge the insightful comments and encouragement provided by my committee members Dr. Andrew Adamczyk, Dr. Tae-Sik Oh, Dr. Russell Mailen, and Dr. Siyuan Dai in writing this dissertation.

I would like to thank Dr. Ruigang Wang and his students Yifan Wang and Zhen Wei for helping with material characterization tests. I am truly grateful to Dr. Amit Nautiyal and Dr. Shatila Sarwar for their insight at every stage and for solving many challenges. Additionally, I would like to extend my gratitude to my lab members Dr. Miaomiao Zhang, Dr. Haishun Du, and Dr. Yue Liang for their help and support in the lab.

At last, I would like to express my sincere gratitude to my family and my friends who supported me throughout the years. I would like to express my deepest gratitude to my parents. My father, Dr. Hung-Chieh Lin, provides me with a warm and safe environment to grow. He teaches me the principles of behaving and dealing with people. His passion and attitude toward the work influenced me deeply. My mother, Chin-Lien Chung, gives me countless support while I face difficulties which comforts my nervousness.

Table of Contents

List of Tables

List of Figures

Chapter 1

Introduction

1.1. Surface engineering

The term “surface engineering” describes a broad variety of techniques intended to design and alter the surface characteristics of components. Surface engineering improves the performance of solid surface by applying thin film coating, surface functionalization and activation, and plasma treatment. Surface engineering can be dated back to Thomas Edison in 1900 with the plating of the gold films. Berghaus was one of the pioneers in the development of plasma and ion modification of surfaces in 1938 to enhance surface characteristics and properties of vacuum deposited coatings. The invention of the ion plating technique in the early 1960s marked a significant advance in plasma-assisted coating deposition. After the early 1970s, thin film deposition and plasma processing were developed, and the history of surface engineering is strongly related to the history of physical vapor deposition (PVD) coatings and processes, plasma processing, and chemical vapor deposition (CVD) techniques. Surface engineering techniques are employed in the automotive, aerospace, power, electronic, biomedical, textile, petroleum, petrochemical, chemical, steel, power, cement, machine tools, and related industries[1]. The following are the desired properties or characteristics of surface-engineered components[2]:

- corrosion resistance through barrier or sacrificial protection
- oxidation and/or sulfidation resistance
- wear resistance
- mechanical properties
- electronic or electrical properties

- thermal insulation
- aesthetic appearance

Surface coatings and surface modification are the two primary types of surface engineering strategies that can be utilized to optimize surface properties and bulk materials. Surface coating is the process of depositing a layer of molten, semi-molten, or chemical materials onto a substrate. The main function of surface coating is to change and strengthen the surface properties rather than reforming the material's composition. On the other hand, the act of changing a material's surface by adding physical, chemical, or biological properties that are not already existing on the surface is known as a surface modification.

1.1.1. Surface coatings

Coatings can be applied to a substrate using a variety of commercially available procedures and methods. For instance, PVD or CVD is used to deposit a thin film in semiconductors, flat panel displays, and solar cells. Sputtering is a plasma-based deposition procedure that accelerates energetic ions toward a target. Atoms are ejected (or sputtered) off the surface when the ions strike the target. As the film is growing, these atoms move toward the substrate and combine with it. One of the most versatile processes for applying protective coatings is thermal spraying. The heat sources utilized in thermal spraying procedures are typically used to distinguish them. The four most often utilized methods are wire arc spraying, plasma spraying, high velocity oxy-fuel spraying (HVOF), and traditional combustion spraying. The most popular coating materials are metals, polymers, and ceramics. Other techniques, such as Electroplating involves reducing the cations of a metal using a direct electric current to produce a metal coating on a solid substrate.

1.1.2. Surface modification

Shot peening is a cold forming modification procedure used to create a compressive residual stress layer and alter the mechanical characteristics of metals and composites. Throughout the procedure, a stream of round hardened steel shot or something similar is launched onto the surface. Ion implantation is a method of surface modification in which ions are implanted into the substrate's surface area. These procedures can increase the substrate material's hardness, wear resistance, corrosion resistance, and fatigue resistance, extending the service life of the final product.

One of the most important methods of creating product distinction in terms of quality, performance, and the life-cycle cost is surface engineering. It is impossible to ignore surface properties in design since they have a significant impact on a component's usability and lifespan. Environments in engineering are harsh. The surface of the component is often subjected to stress as well as chemical and physical deterioration. In order to address these issues and increase the service life and overall performance of the components, surface engineering can be used. In a word, Surface Engineering technology offers practical answers to demanding applications.

1.2. Metals and alloys

The utilization of metal can be dated back to 9000 B.C. Since then, more and more metals were found and be applied in daily life. The very first application of the metal is for good exchange and jewelry. After a while, the application of the metals starts to revolve from ornaments to the tool. Nowadays, the development of human society is mostly depending on the expansion of the metals and its alloys. However, there is a drawback, among all the advantages, about the utilization of the metals and its alloys—corrosion. Corrosion is a serious issue when applying the metals into human society. The impacts of corrosion include finance, energy, and safety. A study from the National

Association of Corrosion Engineers (NACE) in 2016 indicated that the global cost of corrosion is approximately to be $2.5 trillion US dollars, which is equivalent to 3.4% of the global GDP[3]. Also, the impact of corrosion is wide, including infrastructure, utilities, production transportation, and manufacturing. Once the failure occurs, the cost to humans and the environment would be unable to estimate which further reveals that corrosion protection is vital. **Fig 1.1.** illustrates the corrosion cycle of steel which is like many other metals. The life cycle of metal, which gives a basic illustration of metal transformation from nature to practical application, can be divided into four stages. The first stage is ore, native rock containing metals. Most of the native forms of metals existing on the earth are metal oxide. After further treatment, the ore becomes original metal which is the second stage. In this stage, the metal is basically pure with a little impurity and can be introduced into higher technology and industries after being refined. However, because of the thermodynamic process, the materials itself will start to degrade while using it, which is also known as corrosion. This process is a spontaneous procedure and it's unpreventable. So, the metals and alloys will eventually deteriorate back to its original stage, ore and metal oxide. Since this thermodynamic process can't be prevented from happening, the only thing that can be done is slowing down the rate of corrosion.

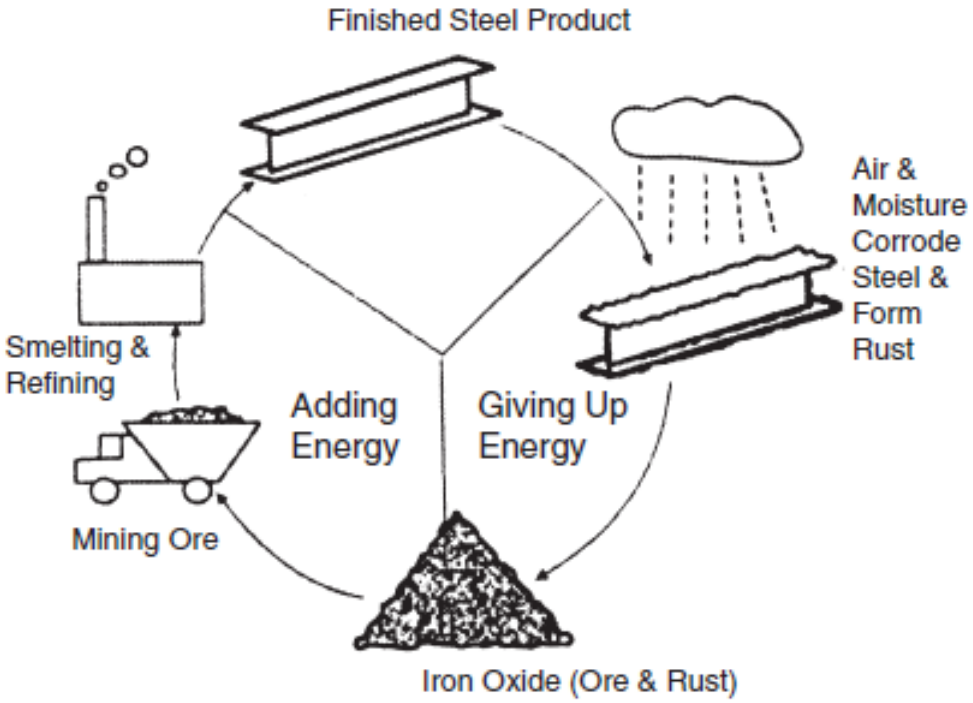

Figure 1.1. The corrosion cycle of steel[4]

In the past, enormous techniques have been revealed for protecting metals from corrosion. Basically, there are three main methods for corrosion protection—cathodic protection[5], anodic protection[6], and inhibitor protection[7]. The main goal of cathodic and anodic protection is varying the metal potential away from the corrosion potential and stay in the passive region. On the other hand, inhibitor protection is creating a protective film or adsorption layer, which affects the electrochemical reaction for the corrosion process. In practice, two or more protection methods will be applied at the same time to obtain a better anti-corrosion performance. According to the inhibitors, chromate, benzoates, and zinc salts are highly effective inhibitors and widely applied in the industry and daily life for anti-corrosion purposes. However, with the increase of the awareness of health and environment-friendly, these inhibitors are suspended or decreasingly used because of the toxicity. In order to replace toxic inhibitors, scientists and engineers have been searching

for new materials in the past decades. Among the abundance of potential materials, conducting polymer attracts attention because of its unique characteristics. Hence, the research of conducting polymer in corrosion protection becomes one of the new branches in the application of conducting polymer.

1.3. Corrosion

Corrosion is a natural process that cannot be prevented depending on the thermodynamic. In other words, metal tends to return to its original state. This tendency will lead to serious issues while utilizing in transportation, industry, and construction. Meanwhile, the corrosion can be related to the electrochemical process. There are many reasons that will lead to corrosion, e.g. temperature[8][9], pH value of the surrounding environment[10][11], the velocity of flowing material[12][13], oxygen[14], humidity[15], bacteria[16][17], and radiation[18][19], etc. For instance, in the industry, the boiler operating at extremely high temperature will release corrosive gas which further increases the rate and possibility of corrosion[20]. In another case, Bacteria and microorganisms existing in nature will build a film over the metal surface changing the pH value and oxygen ratio and creating organic acid which results in corrosion[21]. Since there have various corrosion conditions, it can be divided into different types: uniform corrosion, galvanic corrosion, crevice corrosion, pitting, intergranular corrosion, fretting, erosion corrosion, stress corrosion, dealloying, corrosion fatigue, and exfoliation, see **Fig 1.2.** The mechanisms of formatting each type of corrosion could be varied. In order to recognize the corrosion, it is vital to understand the relationship between the thermodynamic and electrochemical reactions.

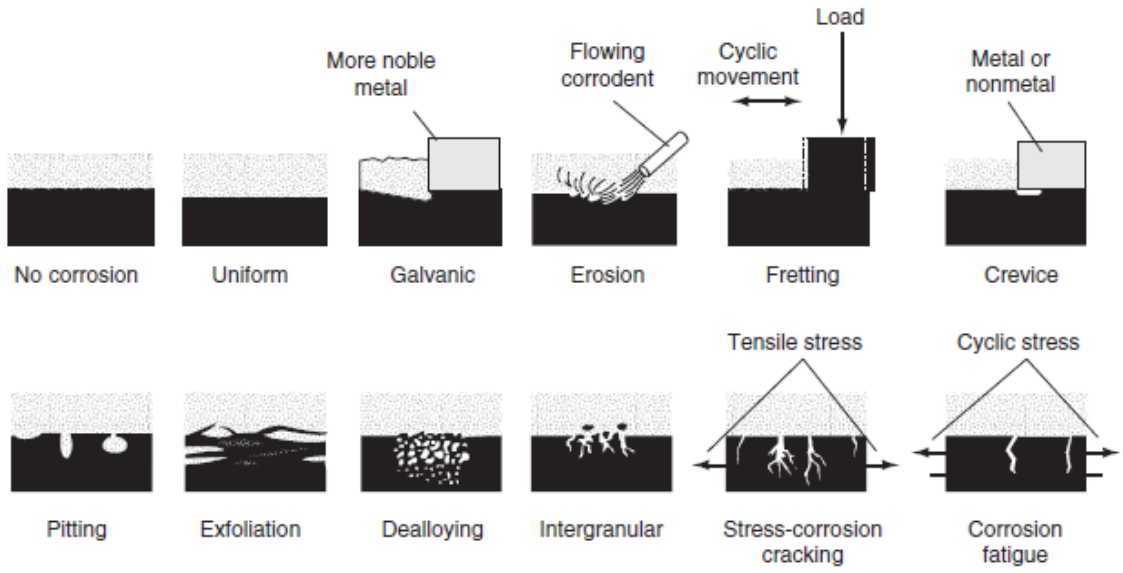

Figure 1.2. Types of corrosion[22]

The basic corrosion process on the metal surface can be described. First, the metal oxidizes to form metal ions: $M \rightarrow M^{n+} + ne^{-}$. In order to make the charges balance, the electron e^{-} will combine with oxygen and water to form hydroxide: $O_2 + 2H_2O + 4e^{-} \rightarrow 4OH^{-}$. The hydroxide will then combine with metal ion becoming metal hydroxide $M_n(OH)_m$. Taking zinc as an example, assuming a zinc rod is placed in hydrochloride solution, zinc ion will release from the zinc rod and the hydrochloride solution will give hydrogen and chloride. The chemical reactions are:

$$Zn \rightarrow Zn^{2+} + 2e^{-}$$

$$HCl \rightarrow H^{+} + Cl^{-}$$

The hydrogen will combine with electrons to create hydrogen gas. And, the zinc ion will form zinc dichloride with chloride ion.

$$2H^{+} + 2e^{-} \rightarrow H_{2(g)}$$

$$Zn^{2+} + 2Cl^{-} \rightarrow ZnCl_2$$

Complete reaction: $Zn + 2HCl \rightarrow ZnCl_2 + H_{2(g)}$

From the equations above, the oxidation reaction is $Zn \rightarrow Zn^{2+} + 2e^{-}$ and the reduction reaction is $2H^{+} + 2e^{-} \rightarrow H_{2(g)}$ which gives an example that a complete reaction should include at least two half-reactions. In the real case, for a corrosion process, the reaction would have one or more oxidation reactions, the same situation for the reduction reaction. In the next few sections, the thermodynamics, kinetics, and transport phenomena of the corrosion will be discussed.

1.3.1. Thermodynamic

1.3.1.1. General chemical reaction

For a general chemical reaction: $aA + bB \leftrightarrow cC + dD$, the forward rate is $\vec{R}$ and the backward rate is $\overleftarrow{R}$. While two rates are equal, we can obtain an equilibrium constant K_c.

$$\vec{R} = K_1 C_A^a C_B^b$$

$$\overleftarrow{R} = K_2 C_C^c C_D^d$$

$$K_c = \frac{K_1}{K_2} = \frac{C_C^c C_D^d}{C_A^a C_B^b} \ \ (while\ \vec{R} = \overleftarrow{R})$$

The relationship between activity constant (K_a) and concentration constant (K_c) can be described as $a = f\ C$, where a is activity, C is concentration, and f is the fugacity of activity coefficient. When $f = 1$, the reaction is in the dilute or ideal case, and $a = C$. Then, we can replace the equilibrium constant into K_a.

$$K_a = \frac{K_1}{K_2} = \frac{a_C^c a_D^d}{a_A^a a_B^b} = K_c (while\ f = 1)$$

Now, for a forward reaction: $aA + bB \rightarrow cC + dD$, the change in free energy can be described as $\Delta G = G_{product} - G_{reactant}$. While the free energy of the reactant is $G_{reactant} = a\mu_A + b\mu_B$ and the free energy of the product is $G_{product} = c\mu_C + d\mu_D$. μ is known as chemical potential which can also present as

$$\mu = \mu^\circ + RT \ln a$$

If replacing μ intoμ_a, $\mu_{\boldsymbol{b}}$, μ_c and μ_d , after rearranging, the ΔG will become

$$\Delta G = G_{prod} - G_{react} = \Delta G^\circ + RT \ln K_a$$

Where $\Delta G^\circ = \left(cG_C^\circ + dG_D^\circ\right) - \left(aG_A^\circ + bG_B^\circ\right)$. From the equation, the relationship between the free energy and the equilibrium constant is obtained. Three conditions of ΔG can be discussed. At $\Delta G = 0$, the rate of reduction and oxidation reaction are equal. This means that the reactions happen at both directions and the rates are equal. While $\Delta G < 0$, the reaction will spontaneously occur and toward one direction. In contrast, the reaction won't happen by itself while $\Delta G > 0$.

1.3.1.2. Thermodynamics for electrochemical reactions

Before converting the chemical energy to electrical energy, the electrochemical reaction can help to understand the basic concepts. Using zinc and copper as an example, the zinc plate is placed in a 1M $ZnSO_4$ solution and copper plate in $CuSO_4$. Without the salt bridge, both metals will have redox reaction itself which are: $Zn^{2+} + 2e^- \leftrightarrow Zn$ and $Cu^{2+} + 2e^- \leftrightarrow Cu$. When connecting two metals with a voltmeter and salt bridge, the zinc plate will give an oxidation reaction and the copper plate will have a reduction reaction. That is because of the standard reduction potential of the two metals are different. Besides, the voltmeter will record 1.1V. In this case, the two reactions represent the chemical energy, and the recorded potential is electrical energy. A good

demonstration of chemical energy transfer to electrical energy is obtained. Therefore, the relationship between these two energies can be described as $\mathrm{nFE} = -\Delta\mathrm{G}$ (the negative sign in free energy is assumed that the reaction is spontaneous).

In the equation, n is the charge number, F is the Faraday constant and E^{rev} is the reversible potential. After rearranging the equation, the potential can be written as

$$\mathrm{E}^{rev} = \frac{-\Delta G}{nF} \; or \; E^{\circ} = \frac{-\Delta G^{\circ}}{nF}$$

To calculate the standard potential, it is much easier if checking the standard reduction potential list in **Table 1.1**. Note that the form of reaction is always in the reduction form.

However, reactants and products are not always in the standard state for real applications. Therefore, if combing the change of free energy,$\Delta\mathrm{G}$, and the standard potential, E°, the combined equation is obtained, called the Nernst equation:

$$E^{rev} = E^{\circ} + \frac{RT}{nF} \ln\left\{\frac{\prod(a_{ox})^{j}}{\prod(a_{red})^{k}}\right\}$$

This equation describes the reversible potential E^{rev} for a half-reaction while the species are not in the standard state. In the dilute solution, the activity coefficient can be replaced by the concentration of the species, $a_A = [A]$. For instance, the potential of a general half-reaction, the Nernst equation can be presented as:

$$\mathrm{aA} + \mathrm{bB} + \mathrm{n}e^{-} \leftrightarrow cC + dD$$

$$E^{rev} = E^{\circ} + \frac{RT}{nF} \ln\left(\frac{[A]^{a}[B]^{b}}{[C]^{c}[D]^{d}}\right) = E^{\circ} + \left(\frac{0.059}{n}\right) \log\left(\frac{[A]^{a}[B]^{b}}{[C]^{c}[D]^{d}}\right) \quad \text{at room temperature}$$

Table 1.1. The list of standard reduction potential[23]

Standard Potentials at 25°C

Half Reaction	Potential
$F_2 + 2e^- \rightarrow 2F^-$	+2.87 V
$O_3 + 2H^+ + 2e^- \rightarrow O_2 + H_2O$	+2.07 V
$S_2O_8^{2-} + 2e^- \rightarrow 2SO_4^{2-}$	+2.05 V
$PbO_2 + 4H^+ + SO_4^{2-} + 2e^- \rightarrow PbSO_4 + 2H_2O$	+1.69 V
$Au^+ + e^- \rightarrow Au$	+1.69 V
$Pb^{4+} + 2e^- \rightarrow Pb^{2+}$	+1.67 V
$2\,HClO + 2H^+ + 2e^- \rightarrow Cl_2 + 2H_2O$	+1.63 V
$Ce^{4+} + e^- \rightarrow Ce^{3+}$	+1.61 V
$MnO_4^- + 8H^+ + 5e^- \rightarrow Mn^{2+} + 4H_2O$	+1.51 V
$Au^{3+} + 3e^- \rightarrow Au$	+1.40 V
$Cl_2 + 2e^- \rightarrow 2Cl^-$	+1.36 V
$Cr_2O_7^{2-} + 14H^+ + 6e^- \rightarrow 2Cr^{3+} + 7H_2O$	+1.33 V
$O_2 + 4H^+ + 4e^- \rightarrow 2H_2O$	+1.23 V
$MnO_2 + 4H^+ + 2e^- \rightarrow Mn^{2+} + 2H_2O$	+1.21 V
$Pt^{2+} + 2e^- \rightarrow Pt$	+1.20 V
$Br_2 + 2e^- \rightarrow 2Br^-$	+1.09 V
$2Hg^{2+} + 2e^- \rightarrow Hg_2^{2+}$	+0.92 V
$ClO^- + H_2O + 2e^- \rightarrow Cl^- + 2OH^-$	+0.89 V
$Ag^+ + e^- \rightarrow Ag$	+0.80 V
$Hg_2^{2+} + 2e^- \rightarrow 2Hg$	+0.79 V
$Fe^{3+} + e^- \rightarrow Fe^{2+}$	+0.77 V
$MnO_4^- + 2H_2O + 3e^- \rightarrow MnO_2 + 4OH^-$	+0.60 V
$I_2 + 2e^- \rightarrow 2I^-$	+0.54 V
$O_2 + 2H_2O + 4e^- \rightarrow 4OH^-$	+0.40 V
$Cu^{2+} + 2e^- \rightarrow Cu$	+0.34 V
$Hg_2Cl_2 + 2e^- \rightarrow 2Hg + 2Cl^-$	+0.27 V
$AgCl + e^- \rightarrow Ag + Cl^-$	+0.22 V
$NO_3^- + H_2O + 2e^- \rightarrow NO_2^- + 2OH^-$	+0.01 V
$2H^+ + 2e^- \rightarrow H_2$	**0.000 V**

Half Reaction	Potential
$2H^+ + 2e^- \rightarrow H_2$	**0.000 V**
$Fe^{3+} + 3e^- \rightarrow Fe$	−0.04 V
$Pb^{2+} + 2e^- \rightarrow Pb$	−0.13 V
$Sn^{2+} + 2e^- \rightarrow Sn$	−0.14 V
$Ni^{2+} + 2e^- \rightarrow Ni$	−0.23 V
$V^{3+} + e^- \rightarrow V^{2+}$	−0.26 V
$Co^{2+} + 2e^- \rightarrow Co$	−0.28 V
$In^{3+} + 3e^- \rightarrow In$	−0.34 V
$PbSO_4 + 2e^- \rightarrow Pb + SO_4^{2-}$	−0.36 V
$Cd^{2+} + 2e^- \rightarrow Cd$	−0.40 V
$Cr^{3+} + e^- \rightarrow Cr^{2+}$	−0.41 V
$Fe^{2+} + 2e^- \rightarrow Fe$	−0.44 V
$Zn^{2+} + 2e^- \rightarrow Zn$	−0.76 V
$2H_2O + 2e^- \rightarrow H_2 + 2OH^-$	−0.83 V
$Cr^{2+} + 2e^- \rightarrow Cr$	−0.91 V
$Mn^{2+} + 2e^- \rightarrow Mn$	−1.18 V
$V^{2+} + 2e^- \rightarrow V$	−1.19 V
$ZnS + 2e^- \rightarrow Zn + S^{2-}$	−1.44 V
$Al^{3+} + 3e^- \rightarrow Al$	−1.66 V
$Mg^{2+} + 2e^- \rightarrow Mg$	−2.36 V
$Na^+ + e^- \rightarrow Na$	−2.71 V
$K^+ + e^- \rightarrow K$	−2.92 V
$Li^+ + e^- \rightarrow Li$	−3.05 V

Note: all ions are aqueous (aq), many neutral species are solids (s), although some are liquids (l), gases (g), and even aqueous (aq). Use other sources for details on state. They were purposely left off here to save space and keep a cleaner looking table.

Now, by calculating the E^{rev}, the half-reaction can be predicted whether it reacts spontaneously or not (when $E^{rev} > 0$ is spontaneous and $E^{rev} < 0$ is nonspontaneous).

1.3.2. Kinetics: the corrosion rates

The previous section discussed the thermodynamics of the corrosion process. Also, the reaction can be predicted whether it is a spontaneous reaction or not by calculating the free energy and the potential. However, in the field of science and engineering, the corrosion rate is much more important. Since the corrosion process is unpreventable, the corrosion industry puts more focuses on decreasing the rate of corrosion. The corrosion rate can be measured by monitoring the mass loss or by electrochemical detection. The method of recording the mass loss is not a convenient way to apply, also the sensitivity of this method is quite low. In contrast, the electrochemical determination gives a better result and quick examination. The definition of corrosion rate can be described as the weight loss of a metal or alloy in a period while immersing in a corrosive environment. A proper unit for corrosion rate is weight loss per unit area per unit time, which is $mg/cm^2\ s^1$. Dividing by the density of the material will give a corrosion rate in the unit of thickness lost per unit time, such as mm/yr. The corrosion rate in electrochemical detection is related to the corrosion current density (i_{corr}), and the equation is:

$$r = \frac{CMi_{corr}}{\rho nF}$$

Where M is the molecular weight of the material (g/mol), ρ is the density of material (g/cm^3), and C is a constant. To calculate the corrosion rate, the corrosion current density is needed.

Firstly, consider an electrochemical half-reaction at equilibrium:

$$M^{z+} + ze^- \leftrightarrow M$$

The rate of both reactions is equal at equilibrium. No reactions are rest or inactive. This equal rate of both directions at equilibrium is defined as the exchange current density, i_0. Also, the electrode

potential is equal to the reversible potential, E^{rev}, when the reaction rate is at equilibrium. Therefore, a plot can represent the situation of equilibrium as a point in potential versus log current density, **Fig 1.3. (a)**. The exchange current density, i_0, is zero at the equilibrium. However, when applying a potential different than E^{rev} to the reaction, the reaction will react toward one direction and a net current can be obtained. The difference between the applied potential and reversible potential is called overvoltage, $\eta = E - E^{rev}$. The overvoltage will lead the reaction toward one direction. When $\eta > 0$, the current is anodic for anodic polarization. In contrast, $\eta < 0$, the current is cathodic for cathodic polarization, **Fig 1.3. (b)**. The relationship between the current density and the potential is given by the Butler-Volmer equation:

$$i_{net} = i_a + i_c$$

$$i = i_0 \exp\left[\frac{\alpha nF(E-E^{rev})}{RT}\right] - i_0 exp\left[\frac{-(1-\alpha)nF(E-E^{rev})}{RT}\right] = i_0 exp\left[\frac{\alpha nF\eta_a}{RT}\right] - i_0 \exp\left[\frac{-(1-\alpha)nF\eta_a}{RT}\right]$$

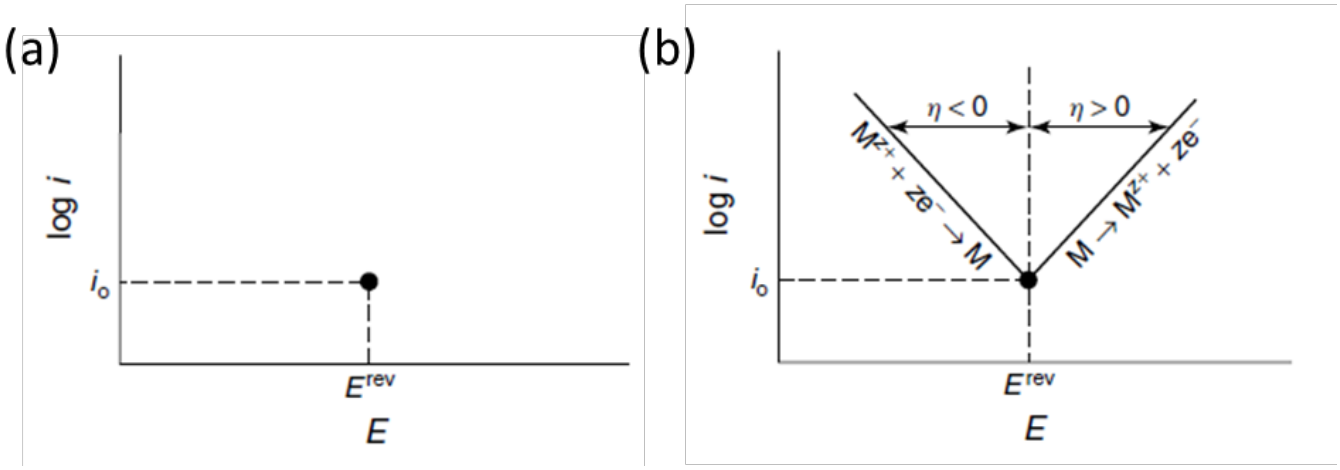

Figure 1.3. (a) a point where the half reaction is under equilbrium, (b) illustration of cathodic and anodic polarization

where α is the charge transfer coefficient and the value of α must between 0 and 1. Since the mass transfer is faster than the electron transfer at the interface of electrode and bulk solution, the Butler-Volmer equation can be developed. Also, for $\eta \gg 0$, the first term will dominates the second term. Then, the Butler-Volmer equation can be simplified into:

$$i_{net} = i_0 \exp\left[\frac{\alpha n F \eta_a}{RT}\right]$$

Also, the equation can be rearranged to get the anodic Tafel equation:

$$\eta_a = b_a \log\left(\frac{i}{i_0}\right)$$

$b_a = \frac{2.3RT}{\beta nF}$ is the anodic Tafel slope. For $\alpha = 0.5$ and $n = 1$, $b_a = 0.12V$ (or V/decade). This calculation is only for single electron reaction. Similarly, while $\eta \ll 0$, the cathodic Tafel equation is given as:

$$\eta_c = -b_c \log\left(\frac{|i|}{i_0}\right)$$

By using the Tafel equation, it is a better description of corrosion kinetics while the reaction at the interface is controlled by the charge transfer.

Previously, the exchange current density i_0 for half-reaction has been obtained. However, a complete corrosion process contains two half-reactions which are anodic reaction and cathodic reaction. To obtain the corrosion current from the electrochemical process, two half-reactions need to be put into consider at the same time. At the corrosion potential, the sum of oxidation current I_a and reduction current I_c is zero.

$$\sum I_a + \sum I_c = 0$$

Fig 1.4. is the Evans diagram for corrosion process where two half-reactions are both presenting in the diagram. The Tafel line for two different reactions, which are the hydrogen reaction and the dissolution of metal, are showing on the diagram. In the **Fig 1.4**, each of them possesses the Tafel line for the anodic and cathodic reaction. Besides, the corrosion potential E_{corr} and corrosion current i_{corr} can be obtained from the cross point between the oxidation of metal and reduction of hydrogen. The diagram reveals a possible electrochemical reaction for a metal in an acid solution which cathodic reaction is mainly the hydrogen evolution. When divide by area, $i = I/A$, the current density is obtained.

$$\sum i_a + \sum i_c = 0$$

The intersect point of the anodic line of metal dissolution and cathodic line of hydrogen evolution is where the total oxidation and reduction current are equal. Hence, the corrosion current density and the corrosion potential are obtained, the corrosion rate could be calculated as well.

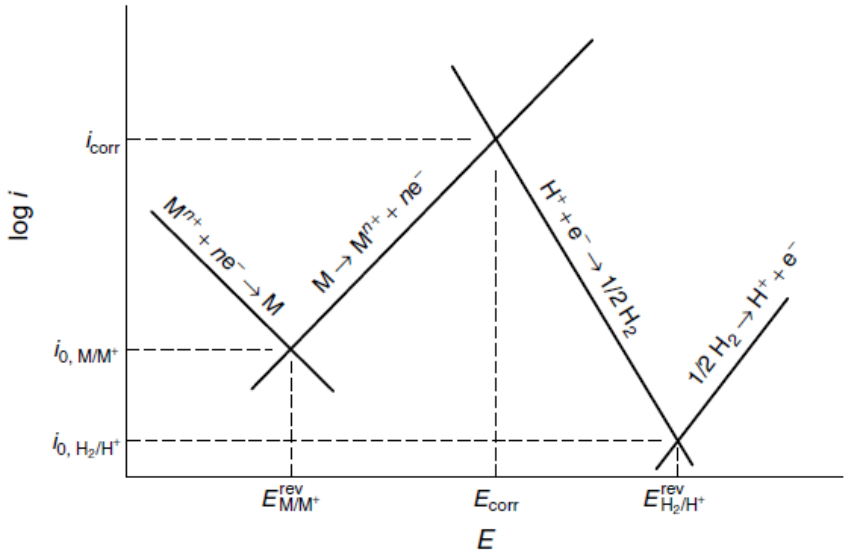

Figure 1.4. The Evan diagram of a corrosion process

1.3.3. The phenomena of the mass transport

The kinetic of an electrochemical reaction in the previous chapter can only utilize in the condition that the concentration of the surface is equal to the concentration of the bulk solution which means there is no concentration gradient between electrode and electrolyte. Under this situation, the electron transfer is the rate-determining step, and the current follows the Butler-Volmer equation:

$$i_{net} = i_a + i_c = i_0 \exp\left[\frac{\alpha n F(E - E^{rev})}{RT}\right] - i_0 exp\left[\frac{-(1-\alpha) n F(E - E^{rev})}{RT}\right]$$

On the other hand, while the rate-determining step is controlled by the mass transport, the electrochemical reaction at the electrode surface follows the Nernst equation:

$$E^{rev} = E^{\circ} + \frac{RT}{nF} \ln\left(\frac{[A]^a[B]^b}{[C]^c[D]^d}\right)$$

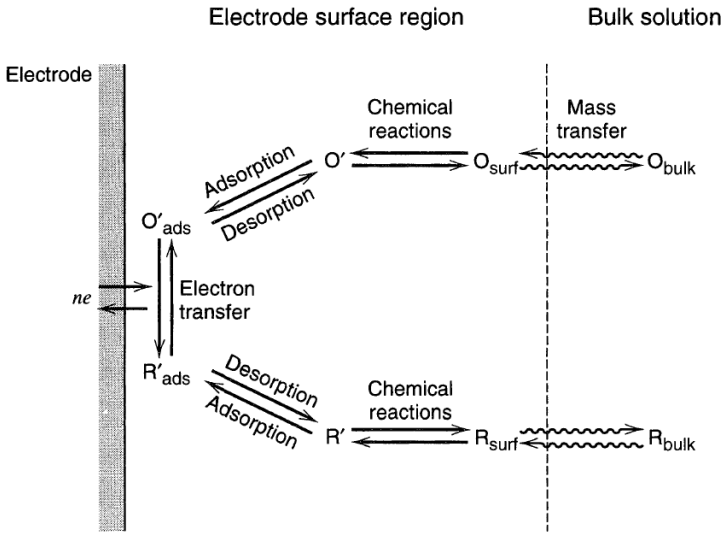

Figure 1.5. Pathway of a general electrode reaction[24]

Therefore, if the rate-determining mechanism is mass transport, the current can be described by another equation. The mass transport, which describes the movement of ions, can divide into three mechanisms including:

1. Convection: hydrodynamic flow caused by the gradient of pressure, density, or temperature. it can be expressed as $J_{conv,i} = c_i v_{sol}$.
2. Diffusion: the movement of ion due to the gradient of concentration and can express as $J_{diff,i} = -D_i(\frac{\partial C_i}{\partial x})$.
3. Migration: the movement of ion due to potential gradient and can express as $J_{migr,i} = \frac{z_i F}{RT} D_i c_i(\frac{d\Phi}{dx})$.

Where J_i is the flux of the species i, c is the concentration, v_{sol} is the solution velocity, D is the diffusion coefficient, z is the charge, F is the faraday constant, Φ is the potential, and u is the electric mobility. When combining three equations, the combined equation becomes:

$$J_i = J_{conv,i} + J_{diff,i} + J_{migr,i} = -D_i\left(\frac{\partial C_i}{\partial x}\right) + \frac{z_i F}{RT} D_i c_i \left(\frac{d\Phi}{dx}\right) + c_i v_{sol}$$

In addition, the charge per mole of any ionic species is $z_i F$(c/mol). Therefore, the current density can be presented as:

$$i = \sum z_i F J_i = -F \sum z_i D_i \left(\frac{\partial c_i}{\partial x}\right) + F^2 \sum \frac{z_i^2}{RT} D_i c_i \left(\frac{d\Phi}{dx}\right) + F \sum c_i \, v_{sol}$$

Depending on the condition and surrounding environment, the equation can be simplified into one or two items. For example, if the electrochemical cell is placed in a stationary environment, then without the flow rate, the convection item can be neglected. Also, while the concentration of the

reactant is small than the concentration of the bulk solution, the migration mechanism will be ignored. Therefore, it is important to clarify the actual mechanism in the system while studying mass transport for the electrochemical process.

1.4. Conducting Polymer

1.4.1. Introduction of Conducting Polymer

Materials can be divided into four types: insulator, semiconductor, conductor, and superconductor depending on the electrical properties. An insulator is a material whose conductivity is less than 10^{-7} S/cm. For a semiconductor, its conductivity is between 10^{-4} to 10 S/cm. And, the conductivity of metal (conductor) is greater than 10^{3} S/cm. In the organic polymers field, the polymers are usually considered as an insulator, such as plastics. As an insulator, they cannot carry current. However, the discovery of conductive polyacetylene doped with iodine breaks the rule and sets a new chapter for these synthesis metals[25]. Numerous conducting polymers had been found since that time. Some common conducting polymers include polyacetylene, polypyrrole, polyaniline, poly (3, 4-ethylenedioxythiophene), polythiophene, poly (ρ-phenylene) and so on, see **Fig 1.6**. The structure of the conducting polymer contains a conjugated backbone, which single and double bonds are connected alternatively, coupled with atoms (e.g. N, S, etc.) providing p-orbitals for a continuous orbital overlap which allow the polymer to be conductive. The overlapping π-orbitals provides the path for charge carriers to move freely throughout the polymer backbone and generate the conductivity. The conductivity can be influenced by many factors such as structure, morphology, oxidation states and functional groups.

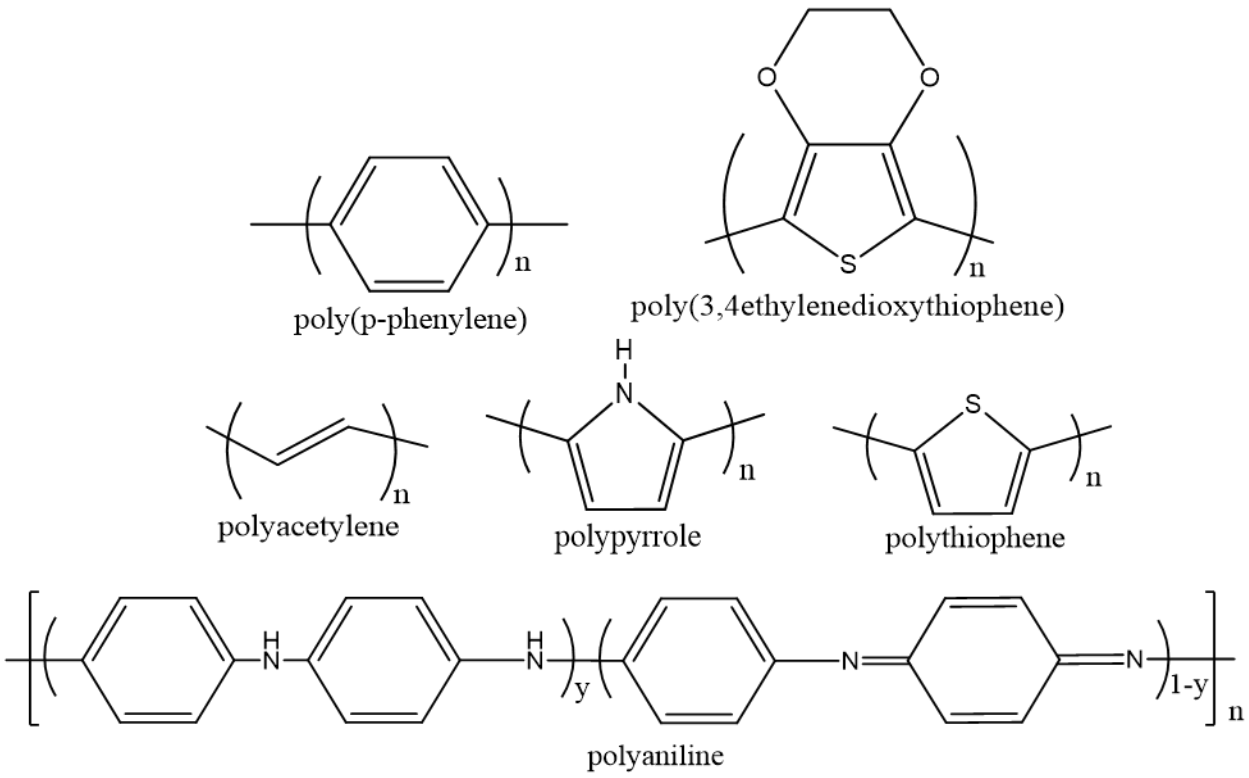

Figure 1.6. Chemical structure of common conducting polymers

The key point of transition from insulator to metal is the doping process. Two different doping processes include oxidation (p-typed doping) and reduction (n-typed doping) which can be written as below (using polyacetylene as an example):

Oxidation (p-doping): $[CH]_n + \frac{3x}{2} I_2 \rightarrow [CH]_n^{x+} + xI_3^-$

Reduction (n-doping): $[CH]_n + xNa \rightarrow [CH]_n^{x-} + xNa^+$

From the chemical or electrochemical doping process, the conventional polymer can be converted into conducting polymer. In addition, the conducting state can return to its insulating state by the de-doping process which makes the conducting polymer more attractive to the science field.

1.4.2. Synthesis of conducting polymer

The method of synthesizing conducting polymer includes chemical oxidative polymerization, electrochemical polymerization, photochemical polymerization, plasma polymerization, and organic synthesis. Among all the polymerization processes, chemical oxidative polymerization and electrochemical polymerization are the most studied and applied. For the chemical oxidative polymerization, it generally includes two steps: oxidation of the monomer and polymer chain growth. In the step of oxidation of the monomer, the oxidant extracts an electron from the monomer to form cation radicals which will then combine the other monomer cation to form a dimer. The polymer chain will keep growing until the reagents are consumed or reach equilibrium, **Fig 1.7**.

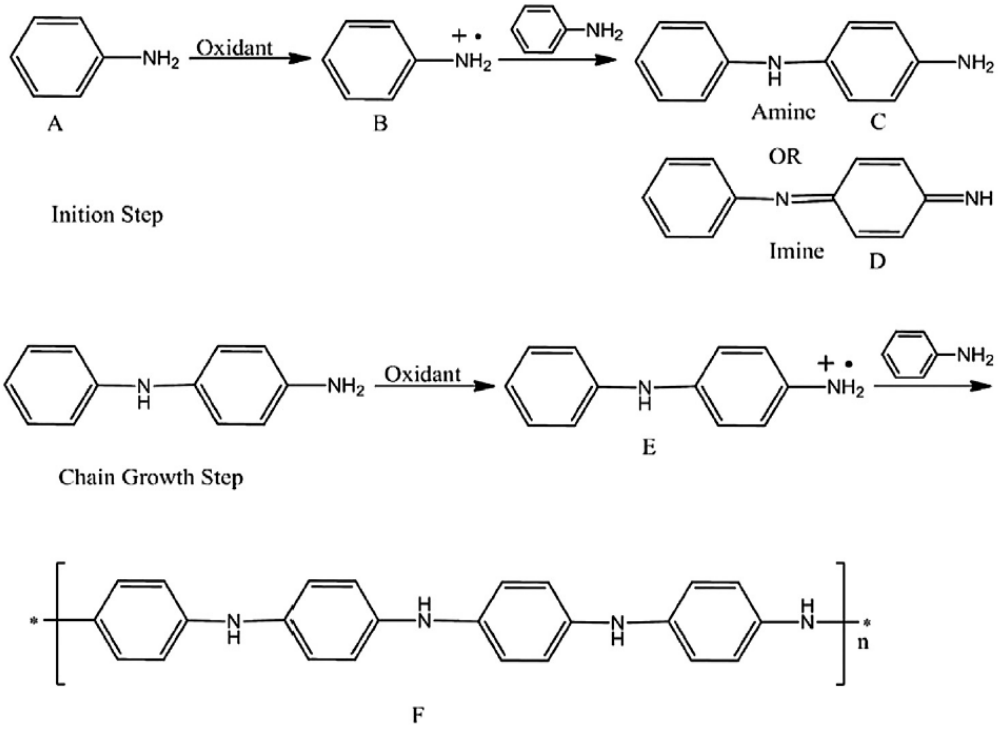

Figure 1.7. Chemical polymerization of polyaniline[26]

On the other hand, the electrochemical process is another major method to prepare the conducting polymer. The reaction is initiated by applying a potential to form cation radical. By coupling two cations radical, the dimer is formed and then keeps combining another monomer or dimer to increase the polymer chain. The polymerization of polypyrrole mechanism is illustrated in **Fig 1.8**. The preparation of the polypyrrole films in the first and second projects will be carried out using the electrochemical process.

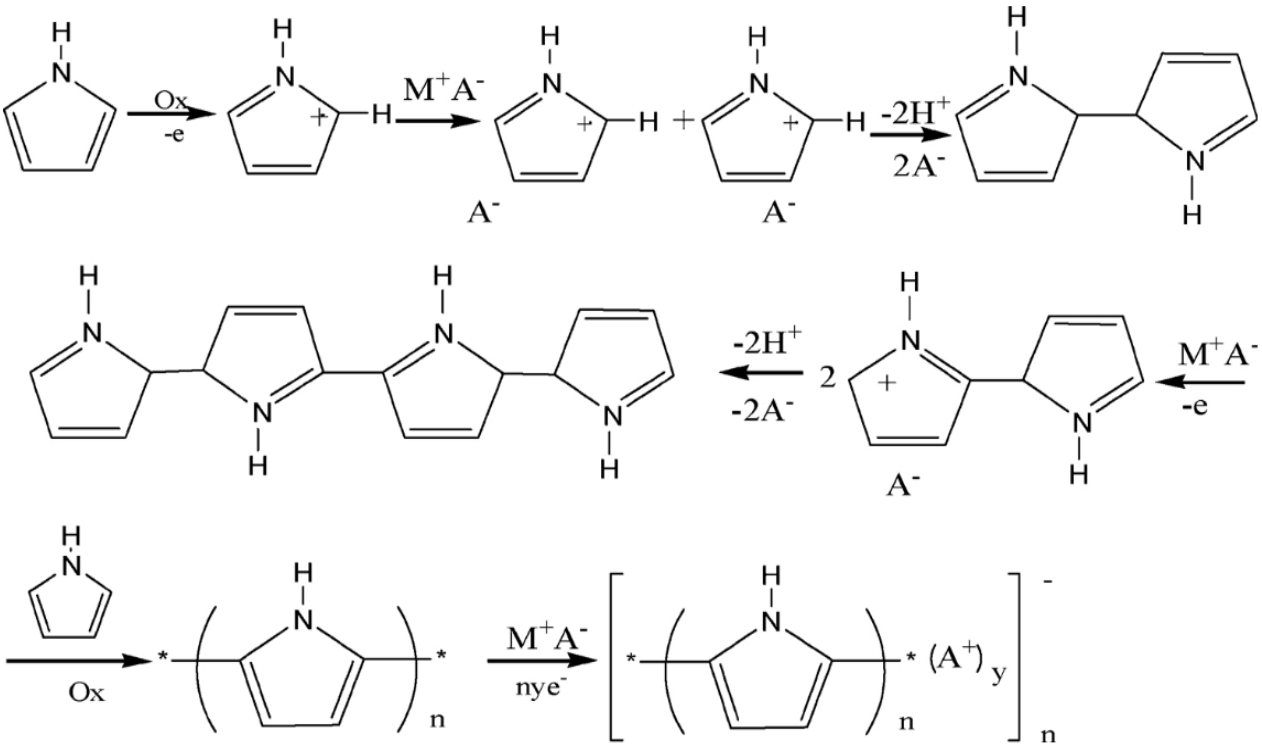

Figure 1.8. Electrochemical polymerization of pyrrole[27]

1.4.3. Application in corrosion protection

The very first application of conducting polymer in corrosion protection can be dated back to 80s[28][29]. In the past, the widely used technique in corrosion protection is an organic coating containing three layers including pretreatment, primer, and topcoat. The first layer, pretreatment,

is a conversion coating that improves the adhesion strength between the metal substrate and the second layer, primer. The primer is the principal of the anti-corrosion provider. Generally, the primer consists of either chromated or non-chromated pigments blending in a spray paint. Topcoat act as a barrier to prevent the corrosive condition from the environment, such as climate or UV light. As environmental awareness and concerns for human health continue to increase, the use of chromate-containing primers is being restricted. This has led to an important focus within the corrosion protection industry on the search for alternative materials to replace chromate. Since the first reported publication of the conducting polymer in corrosion protection is revealed, conducting polymer has been considered as a potential candidate in corrosion control coating. The mechanism of the conducting polymer in corrosion protection had been investigated as well. Many metals and alloys have been studied by using the conducting polymer as an anti-corrosion coating and obtained good results.

1.4.3.1. Polyaniline

For the application of anti-corrosion, polyaniline has been investigated and applied in various metals and alloys. Different dopants affect the structure, size, morphology, electrical properties of the conducting polymer which also have a huge impact on the anti-corrosion performance. For instance, hydrofluoric acid (HF) and camphorsulfonic acid (CSA) are used as dopants for synthesizing polyaniline and compared with emeraldine base polyaniline and emeraldine salt polyaniline[30]. Different coatings were obtained by dispersing the four different polyaniline powders in spray paint and coated on the mild steel. It revealed that polyaniline doped with CSA had higher coating pore resistance which reflects the barrier ability of a coating against electrolyte solution and could provide better corrosion resistance against the corrosive environment.

Similarly, another literature compared CSA and phenylphosphonic acid (PPA) doped polyaniline blended with poly(methylmethacrylate) (PMMA) and coated on various metals such as Fe, An, Cu, and Ni[31]. Both coatings showed the ability to passivate the metal surface. For the corrosion inhibition property, PPA doped polyaniline showed a stronger passivation ability that anions are released to form a second protective layer. To investigate the true passivation mechanism of the conducting polymer, the method of the scanning reference electrode technique (SRET) was applied to study the polyaniline coating on carbon steel and stainless steel[32][33]. The SRET can measure the variation of potential (according to the current flow) over the surface of an electrochemically active sample. The results showed that doped polyaniline coating exhibit anodic activity in the defect area which hold the metal surface in the passive region. **Fig 1.9.** illustrates a good diagram of the anti-corrosion mechanism of the polyaniline for iron.

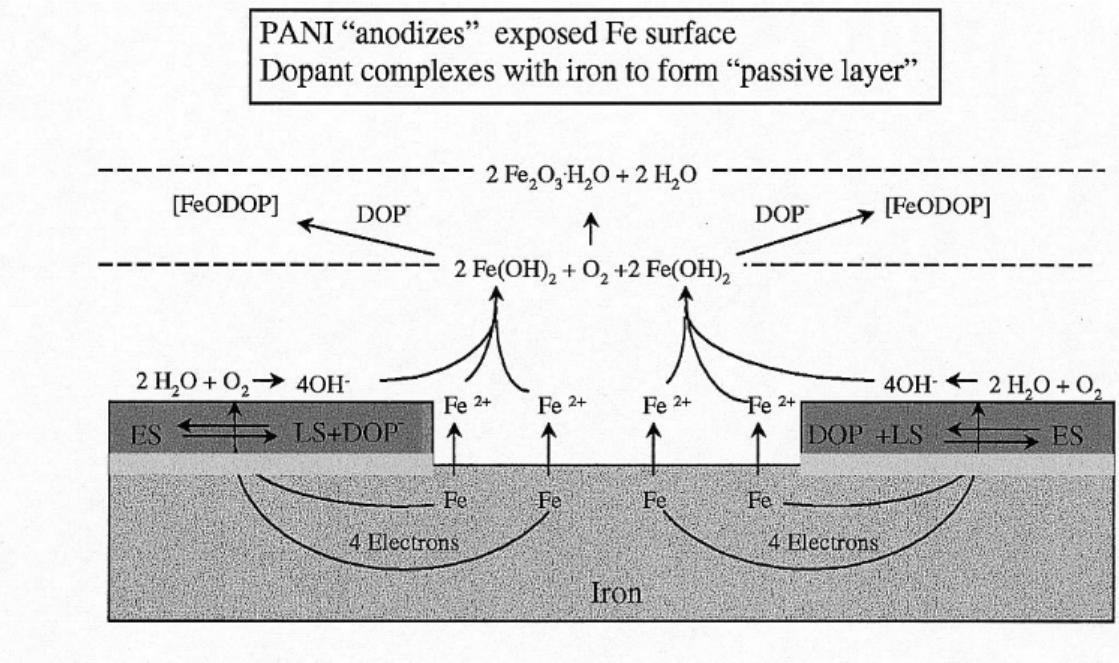

Figure 1.9. The anti-corrosion mechanism of the polyaniline for iron

Despite various dopants, different strategies are also developed including copolymerization with different compounds, multilayers, and nanocomposites, etc. M. Shabani-Nooshabadi and F. Karimian-TTaheri generated a homogeneous polyaniline/zeolite nanocomposite (PZN) on the copper substrate by electrochemical polymerization[34], **Fig1.10**. The corrosion rate of the PZN-coated copper at low zeolite loading was significantly lower than the uncoated copper and pure polyaniline coating. They concluded that the existing zeolite could increase the penetration difficulty of the corrosive agents.

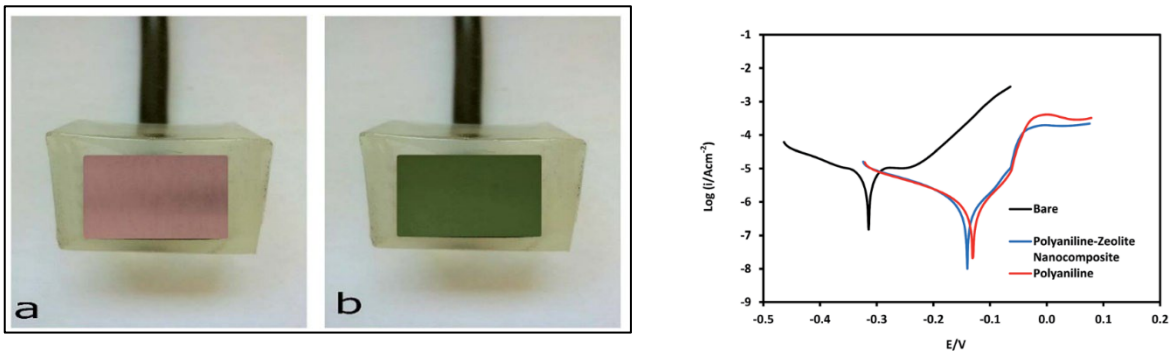

Figure 1.10. The photographs of (a) un-coated and (b) PZN-coated copper electrodes (c) Tafel plot for uncoated, polyaniline and polyaniline/ zeolite nanocomposite coated copper electrodes in 3.5 wt.% NaCl solution

Different nanocomposites were studied and applied on aluminum alloy by M. Ates et al[35]. The polyaniline was modified by TiO_2, Ag, and Zn, and electrodeposited on Al1150. All additive materials not only enhanced the electrical conductivity of the polyaniline but the corrosion resistance. The presence of TiO_2, Ag, and Zn can prevent oxygen and water from penetrating into the alloy surface. Among those additives, the best protection nanocomposite coating was polyaniline/Ag since it had the highest protection efficiency (PE=97.54%) and the lowest porosity (P=0.080). Graphene and Graphene oxide has also been utilized in the synthesizing process to obtain composite. For example, the graphene/polyaniline hybrid (GPn) was coated on copper and

act as a barrier for the substrate[36]. The coated copper was tested in sodium chloride and sulfuric acid, and it provided superior corrosion protection than pure polyaniline in both corrosive solutions. An interesting result is that the contact angle of the GPn coating is increased which prevents the water from penetration and prolongs the protection effect. In the field of corrosion protection, hydrophobicity is also important, **Fig 1.11**.

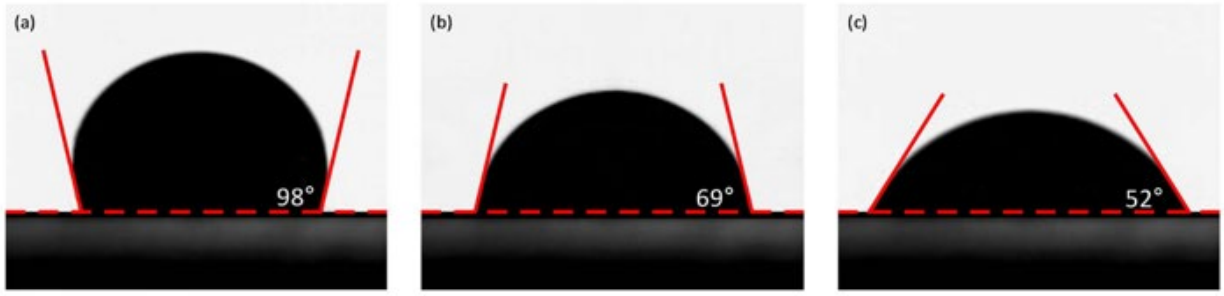

Figure 1.11. Water-droplet contact-angle test on (a) GPn-Cu, (b) Polyaniline-Cu, and (c) Bare-Cu

B. Ramezanzadeh et al. reported a new strategy for providing the zinc-rich epoxy coating (ZRC) with enhanced cathodic and barrier protection by adding GO-polyaniline nanosheets[37]. The polyaniline was synthesized on the graphene oxide surface through in-situ polymerization. In this case, the GO-polyaniline nanosheets provided additional protection time up to 2000 hours due to the porosity of ZRC coating that was filled by GO-polyaniline nanosheet which allowed the zinc particles to stay much longer from oxidation. Through the literature, the polyaniline itself can provide good corrosion protection by ennobling the metal surface. Also, making nanocomposite and filled the composite into organic coating can further enhance the resistance of corrosion.

1.4.3.2. Polypyrrole

Rather than polyaniline, another widely studied conducting polymer is polypyrrole. The research of polypyrrole are basically like the polyaniline. Different dopants, copolymers, nanocomposites, and blend with organic coatings are all been applied in investigating the corrosion protection efficiency of polypyrrole. Different solvents (water, acetonitrile, and nitromethane) had been studied for the preparation of the polypyrrole and its anti-corrosion performance[38]. The SEM results indicated that the size of the conducting polymer is strongly affected by the polymerization rate, **Fig 1.12**. The smallest and densest particles are obtained from the nitromethane solution because of the slowest polymerization speed, it also possessed the highest corrosion protective effect on stainless steel. Additionally, it is known that the dopants used in chemical and electrochemical polymerization can strongly affect the conductivity and the morphology of the conducting polymer and it affects the corrosion protection. M. Eslami et al. pointed out the polypyrrole synthesized with sodium nitrate can provide longer protection time[39].

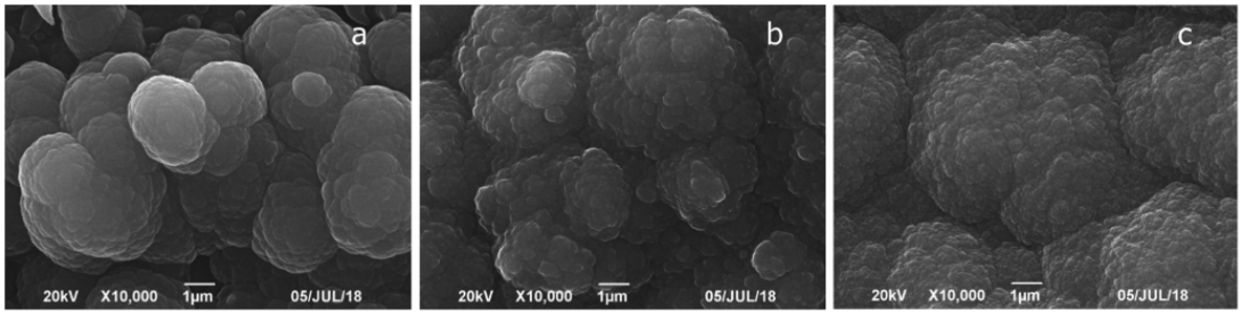

Figure 1.12. SEM of (a) SS/PPy-H_2O (b) SS/PPy-ACN and (c) SS/PPy-CH_3NO_2

H. M. Hung et al. studied two dopants (10-camphorsilfonuc acid and sodium molybdate) in the improvement of the corrosion protection for mild steel[40]. It turns out that the polypyrrole film doped with both CSA and MnO_4^{2-} ion could enhance the protection of the polypyrrole with self-healing and barrier properties. Titanium was studied by covered with polypyrrole utilizing sodium dodecyl benzene sulfonate (SDBS) and dopamine (DA) as dopants at the same time[41]. The

doped-polypyrrole film showed a higher positive shift in corrosion potential and lower corrosion rate, resulting in good corrosion protection. A.V. Syugaev et al. compared two different dopants—oxalic acid and sodium dodecyl sulfate (SDS) for their protection efficiency[42]. The result turns out that changing the dopant from oxalic acid to SDS can influence the morphology of the polypyrrole and have a huge impact on the corrosion protection time, **Fig 1.13**.

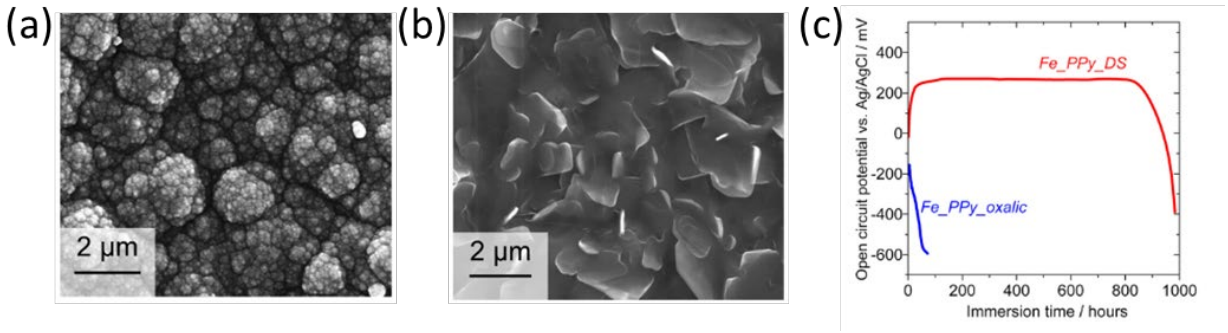

Figure 1.13. SEM images of (a) PPy_oxalic (b) PPy_DS and (c) open circuit potential evolution for iron coated with PPy film

Just like polyaniline, despite pure polypyrrole, scientists keep looking for new strategies to promote the ability of the conducting polymer in corrosion protection. Graphene and graphene oxide is added into the epoxy coating with polypyrrole to accomplish synergistic anti-corrosion properties[43][44]. Filling with graphene or graphene oxide will increase the penetration resistance of the coating to prevent corrosive media from reaching the metal surface. In addition, R. Mohammadkhani et al. utilized graphene oxide decorated by polypyrrole doped with zinc particles for protecting the carbon steel[45]. The outcome revealed that the active inhibition and the barrier property of the coating were affected. Moreover, the presence of zinc particles can interact with the hydroxide to form an insoluble zinc hydroxide film which further prevents the dissolution of

alloy. This coating showed a good protecting effect on intact and defected samples and the possible mechanism is illustrated below, **Fig 1.14**.

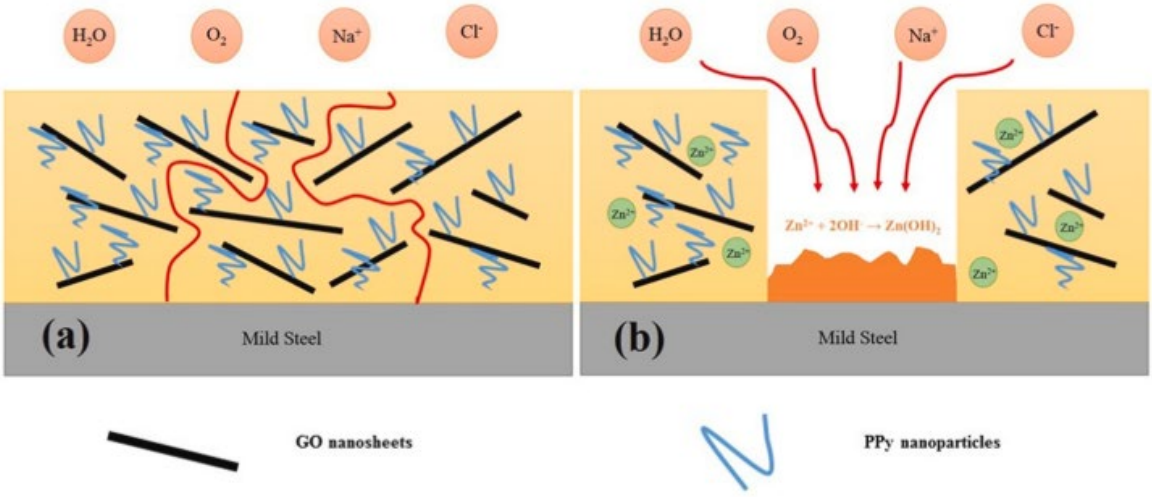

Figure 1.14. Corrosion protection mechanism of the nanoparticles for (a) intact and, (b) defected samples

Besides polypyrrole and polyaniline, other conducting polymers are also been utilized in corrosion protection, such as polythiophene[46][47][48] and poly(3,4-ethylenedioxythiophene)[49][50]. Briefly summarizing the application of conducting polymer, two approaches (chemical and electrochemical polymerization) are widely used. Adding one or more materials in conducting polymer, e.g. graphene, graphene oxide, or metal oxide, can further enhance the protection. On the other hand, mixing the conducting polymer with a small amount into the organic coating is another feasible method as well.

1.4.4. Corrosion protection mechanisms of conducting polymer

After years of investigation, the protection mechanisms of conducting polymer can be simply divided into four types, which are anodic protection mechanism, controlled inhibitor release mechanism, an electric field, and barrier effect. In the anodic protection mechanism, due to the redox nature of conducting polymer, the conducting polymer will reduce and create a passivation condition for the oxidized metal. In table 2, the conducting polymer owns a higher oxidation state compared to metals indicating the ability of the conducting polymer for stabilizing metal oxide layer and keeping passivation[51].

Table 1.2. The standard potential for metal and conducting polymer

Redox couple	Standard potential vs. SHE(V)
Mg/Mg^{2+}	-2.36
Al/Al^{3+}	-1.66
Zn/Zn^{2+}	-0.76
Fe/Fe^{2+}	-0.44
Polypyrrole	-0.1-0.3
Polyaniline	0.4-1.0
polythiophene	0.8-1.2

B. Wessling had demonstrated that the metal coating with polyaniline can shift the corrosion potential into the direction of noble metal, and passivates the metal by forming a metal oxide layer in NaCl solution[52][53]. R. Gašparac et al. investigated the mechanism of corrosion inhibition by polyaniline in sulfuric acid solution[33]. They used the scanning reference electrode technique to study the passivation of exposed stainless-steel regions and found that the polyaniline film can heal the exposed region and keep it in the passive region. As a result of a galvanic coupling, the

corroding metal and conducting polymer will have a redox reaction while the conducting polymer will reduce, and the metal will oxidize. At the same time, the dopants will be release from the conducting polymer. The released anion can stop or slow down the corrosion process, so called the controlled inhibitors release mechanism. In this mechanism, the released anion will combine the metal ion to form a metal complex and prevent the metal for further dissolution[54], see **Fig 1.15**. S. Souza et al. used acrylic as an organic coating blend with sulfonate-doped polyaniline to test the anti-corrosion performance[55]. The results showed that the dopant anion and iron will form a camphorsulfonate-iron complex as a second protective layer to passivate the metal surface. J.E. Pereira da Silva et al. applied polyaniline with two different dopants, camphorsulfonic and phenylphosphonic acid, blending with poly(methyl methacrylate) for the corrosion protection of different metal[31]. It revealed that polyaniline doped with phenylphosphonic acid had better protective coating performance. Another research also investigated the inhibitor mechanism by using polypyrrole doped with two different dopants for iron[56]. It turned out that, in the defect area, the release of the inhibitor appears from the coating and passivates the defect. A dense, low porosity, the adherent coating film can prevent the corrosive ion from penetrating the coating layer and reach the metal surface, further stop or slow down the corrosion reaction. While having a low porosity coating, the transport rate of O_2 and H_2O is lower. In addition, the reaction site of the oxygen reduction will be move from the metal/coating interface to coating/electrolyte interface[57]. On the other hand, while metal contact the conducting polymer, an electric field is generated which the flow rate of electrons will be influenced and then the corrosion is decreased.

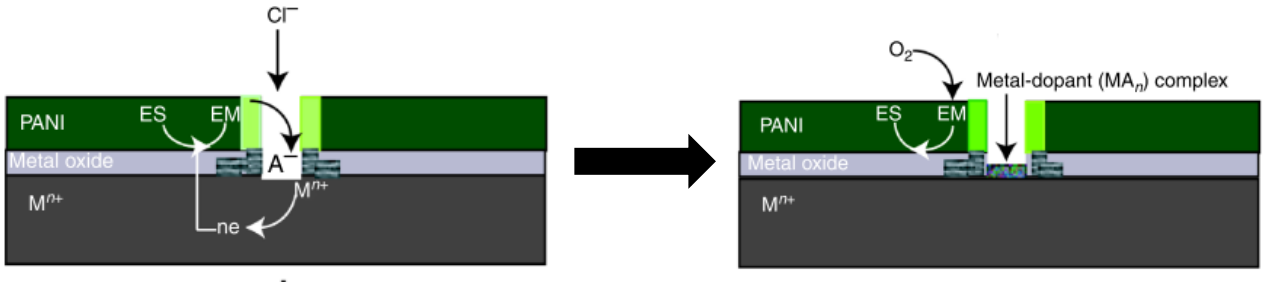

Figure 1.15. The mechanism of controlled inhibitor release

1.5. Characterization for anti-corrosion performance

Expect of the general SEM and TEM measurement to observe the morphology of the polymer, there are other methods to evaluate the anti-corrosion performance of the polymer including the Tafel test, Electrochemical Impedance Spectroscopy (EIS), salt spray test and the adhesive test, etc. The Tafel test is measuring the corrosion potential and corrosion current of the coating materials. The ESI test observes the interface behavior between two phases. For the salt spray test, the coating will be scratched a cross and put into the corrosive median to test its anti-corrosion ability. The adhesive ability between coating and substrate can be detected by the adhesive test which follows the standard procedure. Furthermore, the simplest way is immersing the sample directly into the corrosive meditate for a long period and then see the surface change.

1.5.1. The Tafel Test

In **Fig 1.16.** the theoretical current for the cathodic and anodic reaction is a straight line. However, the real test result will show a curve line. To obtain corrosion current and corrosion potential, extrapolating the straight line from each reaction to get a joint which is the value of corrosion potential and corrosion current. Comparing the uncoated and coated sample, the corrosion potential represents the performance of the corrosion resistance. With higher corrosion potential

gives better corrosion protection. And, corrosion current could be used to calculate the corrosion rate. Having a lower corrosion current indicates a slower corrosion rate which is more preferred.

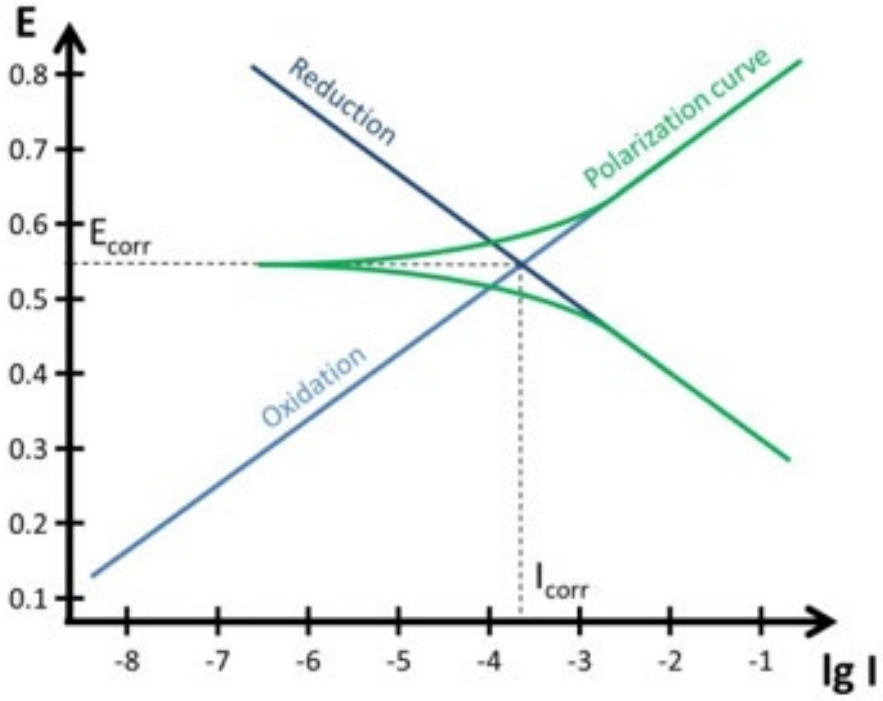

Figure 1.16. The Tafel plot

1.5.2. The Electrochemical Impedance Spectroscopy, EIS

This analytic technique is an effective way to describe the electrochemical system characteristic. By applying the concept of diffusional impedance, the relationship of potential and current controlled by mass transfer under the electrochemistry system can be described. The EIS is mostly applied in anti-corrosion, batteries, capacitor, semiconductor, fuel cell, and biomedical. In the corrosion protection, the resistance and diffusion ability between surface and coating can be detected. The typical diagram is shown in **Fig 1.17**. The semicircle represents the resistance of the charge transfer and the straight line with 45 degree represents the capacitance.

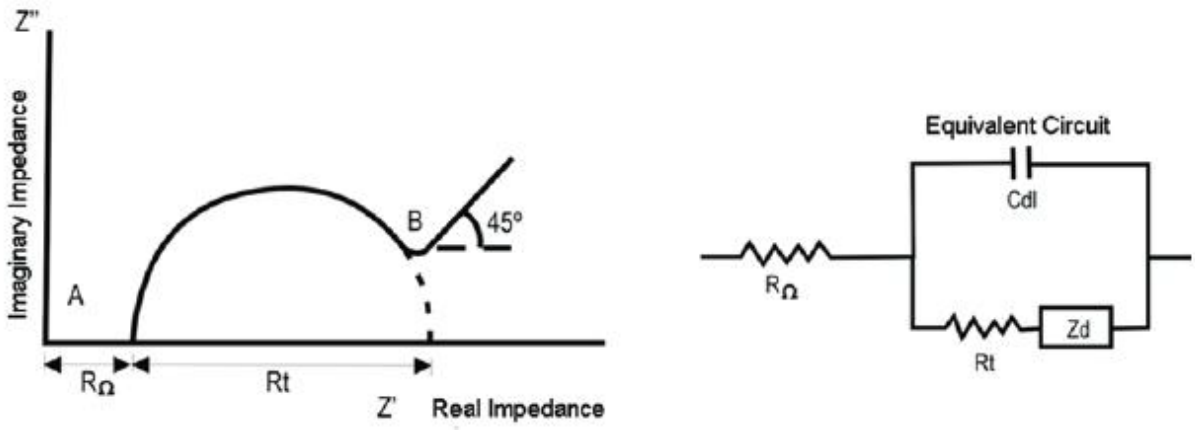

Figure 1.17. The EIS diagram

1.6. Biosensor

A biosensor is a device that detects the presence of an analyte in a biological or chemical process and produces signals corresponding to that concentration. Leland Charles Clark Jr. initially described biosensors in 1962. He created the concept of exhibiting the biosensor's components together with a strategy to integrate a bioreceptor with a transducer device[58]. Biosensors are used in various industries, including the food safety[59], environmental monitoring[60], water quality[61][62], drug discovery[63][64], toxic detection[65], the soil quality, etc., and they provide higher stability and sensitivity when compared to conventional approaches. **Figure 1.18.** indicates different areas of research where biosensors have been used.

1.6.1. Biosensor structure

A typical biosensor includes an analyte, bioreceptor, transducer, electronics, and display (**Figure 1.19.**).

Analyte: a substance of interest whose components are being identified or discovered (e.g., glucose, ammonia, alcohol, and lactose).

Bioreceptor: a bioreceptor is a molecule that specifically recognizes the analyte. Examples of biological receptors include enzymes, cells, aptamers, deoxyribonucleic acid (DNA), and antibodies. Bio-recognition is the process of signal production (in the form of light, heat, pH, charge or mass change, etc.) as a result of the interaction of the bioreceptor with the analyte.

Transducer: a device that transforms one type of energy into another. The transducer's function in a biosensor is to convert a bio-recognition event into a measured signal. Signalization is the term for this energy conversion process. Depending on the number of interactions between analyte and bioreceptor, transducers produce optical or electrical signals.

Electronics: the transduced signal is processed and prepared for the display. The transducer's electrical output signals are amplified and transformed to digital data. By the display unit, the processed signals are quantified.

Display: The display unit is made up of a user interpretation system, such as a computer or printer, that provides understandable figures or curves for the user to read. The output might be a numerical, visual, tabular, or figure depending on the end-user requirement.

1.6.2. Classification of biosensor

Classification of biosensors depending on the diverse use of bioreceptors and transducers. The main components of biosensor technology are bioreceptors. Bioreceptors are the biological molecular species that depend on the biochemical recognition process. By attaching to bioreceptors, relevant analytes can create a signal that the transducer can measure. Some common bioreceptors includes enzyme, antibody, cell, aptamer, and nanoparticles. Transducers can be classified into the following groups: electrochemical, optical, thermal, electronic, acoustic, and gravimetric.

Figure 1.18. The application for biosensor[66]

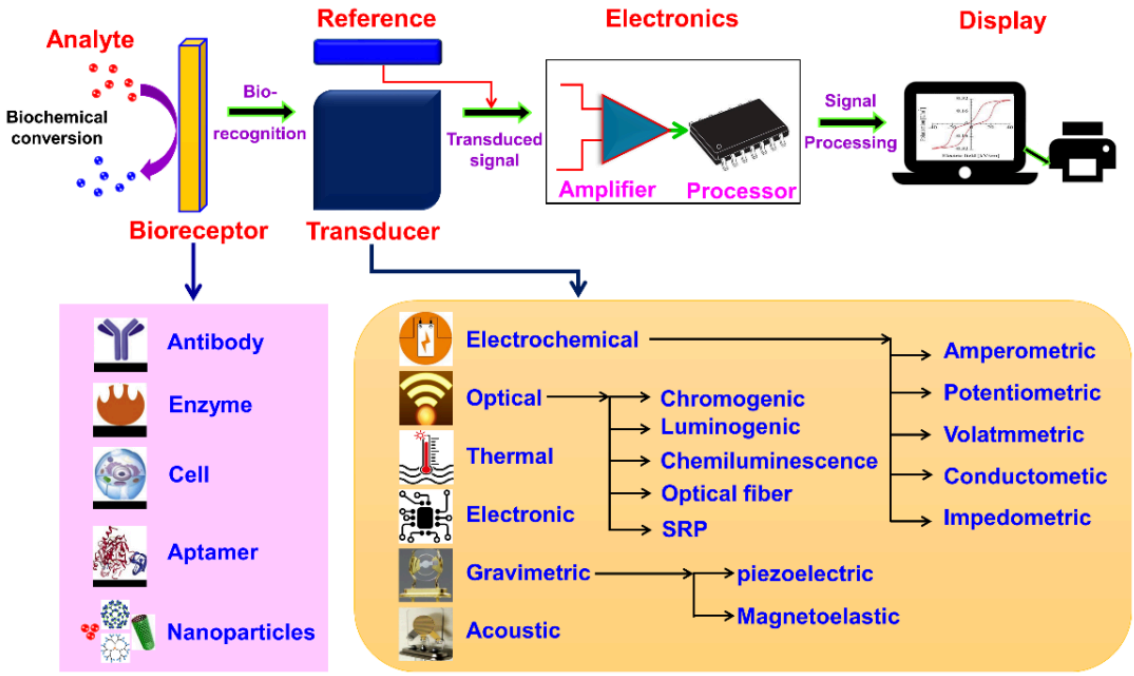

Figure 1.19. The structure for biosensor[67]

1.7. Microwave-initiated synthesis of nanocomposite

The microwave-assisted synthesis method has received many attractions due to its advantages compared to the conventional approaches. Most of the conventional approaches demand energy-intensive preparation conditions (such as high temperature and ultrahigh vacuum) and relatively signification amounts of chemicals that might be harmful to the environment. As an alternate method, microwave-driven synthesis provides a wide range of chances to create nanocomposite materials for various purposes due to its distinctive advantages, including a rapid reaction rate, cheap processing, high yields, and side reaction depression.

1.7.1. Microwave heating chemistry

A microwave is a form of electromagnetic energy which defined in a measurement of frequency as 300 MHz to 300 GHz in the range of 1 mm to 1 m, i.e. between infrared (IR) and radio frequency (RF) in the electromagnetic range. At the moment, 2.45 GHz (wavelength of 12.24 cm) is by far the frequency most often utilized for household microwave ovens. However, due to lower energy consumption, large industrial/commercial oven use 0.915 GHz (wavelength of 32.8 cm)[68].
The advantages of a microwave over traditional heating include the following[69]:

- the substance heats uniformly throughout
- increased process speed
- high heating efficiency
- reduction of unfavorable side effects
- reproducibility
- purity
- no heat loss

- reduce wastage of reaction vessel
- low cost of operation

1.7.2. The effect of "graphene" on microwave heating

The free movement of electrons on the surface of graphene in the presence of microwave radiation can result in the production of heat via a resistive heating mechanism. As the primary heat source during microwave-initiated synthesis, graphene has a high interaction with microwaves, making it an excellent susceptor for achieving quick and homogeneous heating. Several parameters affect the microwave heating process. Electronic conductivity is one of the most important factors in metallic and semiconducting materials. Experimental data demonstrated that the materials with moderate conductivity (10^{-5} to 10 Ω m) heat more efficiently than insulating or highly conducting materials[70]. Dimension is also another key component. For a thick metallic conductor, the microwave irradiation can be reflected in most of the cases due to the skin effects, while the thin conductors have a lot less reflection than the thick ones, since the skin depth is larger than the dimension of the sample, thickness, diameter, etc. Therefore, the nanoscale structures of graphene sheets operate as a potential microwave absorber, capable of efficiently and quickly converting microwave energy to thermal energy.

1.8. Research motivation and objectives

The behavior of ions between the interface of two components can be measured by using electrochemical techniques such as cyclic, voltammetry (CV), Tafel, electrochemical impedance spectroscopy (EIS), and differential pulse voltammetry (DPV). When the transport of ions penetrates through the interface, a potential difference will occur. The collection of potential differences can be interpreted to explain the performance of the surface.

In the corrosion protection project, the objective is to produce a high anti-corrosion performance PPy coating using electrodeposition, which will effectively protect against corrosion. The primary research objectives include: (i) determining the optimized concentration of dopants for electrodeposition of PPy layer on metal or metal alloy by studying the passivation ability of dopants; (ii) assessing the electrochemical performance of the PPy layer to identify its protective efficiency; (iii) improving the adhesion of the electrodepositing PPy layer by utilizing a secondary dopant as an adhesion promoter; and (iv) incorporating a conventional protection coating to mimic the practical application, where a resin topcoat and a PPy primer layer .

The objective of the biosensor project is to create an electrochemical biosensor that can detect COVID-19 with high sensitivity and selectivity. The major research objectives of this proposal are: (i) to develop a general and optimized methodology for synthesizing ZnS/graphene nanocomposites quickly and efficiently using microwave-initiated heating; (ii) to utilize a ZnS/graphene modified electrode for selecting probe DNA from artificial DNA samples; (iii) to evaluate the sensitivity and selectivity of the selected probe DNA and ZnS/graphene modified electrode using standard COVID-19 samples; and (iv) to develop a one-step hybridization process that can reduce the preparation time of the multiple-step procedure.

Chapter 2

The synergetic effect of tannic acid as adhesion promoter in electrodeposition of polypyrrole on copper for corrosion protection

2.1. Introduction

Copper, which possesses high electrical conductivity and good thermal conductivity, is utilized in many fields including electronic devices, construction, industrial equipment, and transportation. Comparing with many other metals, copper itself has good corrosion resistance due to positive standard electrode potential. However, many reports have indicated that the corrosion of copper remains possible under various situations, especially the existence of chloride ions[71][72]. To avoid the corrosion, adding corrosion inhibitors in the organic coating has been developed to prevent the degradation of copper and extend the life of its application. Although it has been a long time since these inhibitors—azole, benzotriazole, and their derivates—have been utilized, these toxic inhibitors need to be replaced because of the increase in consciousness in living (human) health and environmental impact[73][74][75]. Recently, many findings showed that conducting polymers (CPs) could be used to replace toxic inhibitors[76][54][57].

The first study of corrosion protection by CP was in 1985, DeBerry investigated the ability of polyaniline to keep passivation of stainless steel in sulfuric acid[28]. Since then, the research of CPs for corrosion protection starts growing and becomes a new branch for the application of CP. The protection mechanisms of CP were studied and demonstrated that coating with CP could protect the metal by releasing the anions to form the passive layer which stops the dissolution of the metals and metal alloys such as iron, copper, stainless steel and aluminum alloy[52][77].

Moreover, it can act as a barrier to prevent aggressive materials from reaching the metal surface[78].

In general, chemical and electrochemical synthesis are two methods used in making the protective CP film on the metal surface. The electrodeposition of CPs has been successfully operated by much research[79][80][29]. Three steps are included in the electropolymerization process: (i) the passivation of the metal surface prior to the polymerization of CPs (ii) the polymerization of CPs, and (iii) the growth of the CP film. Among these three steps, the most important one is the passivation of the metal[81][34]. The reason is that if the metal surface is not well passivated, the dissolution of the metal will keep happening during the polymerization, which leads to failure in electrodeposition of a CP film. Therefore, a suitable condition for the electrochemical cell is essential. In fact, there are a lot of studies investigating dopants' effects on passivating the metal surfaces, including oxalic acid[82], sulfuric acid[81], p-toluenesulfonic acid[83], sodium dodecyl sulfate[42][84], sodium nitrate[39], and sodium salicylate[85]. However, few focuses on finding the optimized concentration for passivating the metal. The adhesive ability of the coating was not a primary focus in another research. This work focuses on finding the optimal conditions for selected systems, which could achieve the best passivation and form a stable metal oxide layer. Oxalic acid and sodium salicylate were selected to have their experimental parameters investigated, under which the coating would possess the lowest passivation potential and highest corrosion protection efficiency. Moreover, tannic acid was added into the electrolyte as a promoter to increase the adhesion property. PPy was obtained from the electropolymerization of the pyrrole monomer during the experiment. The coatings were prepared and tested in the three-electrode system. The anti-corrosion performance of different dopants with various concentrations was compared by various measurements in 3.5 wt% NaCl solution.

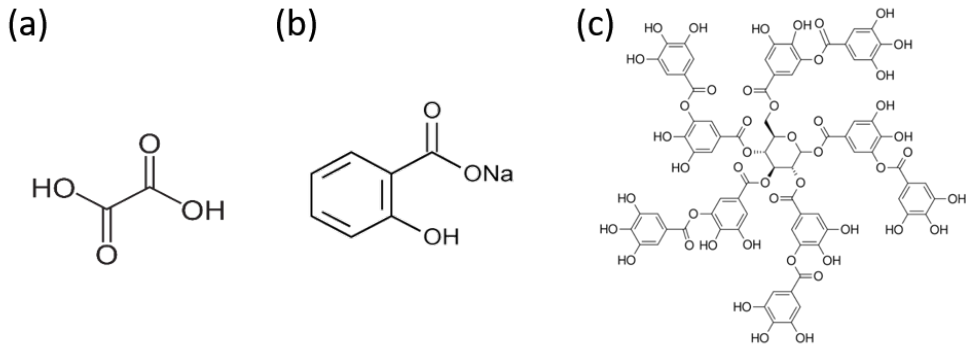

Figure 2.1. The chemical structures of (a) oxalic acid, (b) sodium salicylate, and (c) tannic acid

2.2. Experimental

2.2.1. Materials

Pyrrole was purchased from Alfa Aesar. Oxalic acid (OA) was obtained from Spectrum Chemicals. Sodium chloride (NaCl) was bought from BDH Chemicals. Tannic acid (TA) and sodium salicylate (SA) were purchased from Beantown Chemical. All materials were used as purchased without pretreatment. Copper sheets with 99.9% purity were used as received.

2.2.2. Preparation of copper electrode

The copper plate was cut into 1 x 1cm^2. After polishing one side of the copper, the wire and the polished side were connected by using the solder and placed in a mold. Then, the acrylic resin was poured into the mold and dried for 24 hours at room temperature. The cured copper electrode had then been polished by sandpaper from 800, 1000, to 1200 grits. After polishing, the electrode was washed twice with deionized water and acetone, respectively. After that, the electrode was kept in the hood to dry out before carrying out the experiments at room temperature.

2.2.3. The passivation of the copper electrode

The passivation of the copper was investigated by an electrochemical technique—linear sweep voltammetry (LSV). The three-electrode system, including copper as a working electrode, platinum mesh as a counter electrode, and Ag/AgCl as a reference electrode, was set up for the experiments. The electrolyte in the system was prepared in concentrations from 0.2 M to 1.0 M for each dopant, OA, and SA. The sweeping potential was operated from -0.1 V to 1.0 V under 10 mV/s by the CH Instrument (CHI 760D).

2.2.4. The electrodeposition of conducting polymer

For the electrodeposition process, the copper electrode was placed in the electrolyte with the dopants' optimized concentration which was obtained from the passivation results and 0.1 M pyrrole monomer. Under the optimized concentration, the copper electrode was applied at a constant potential at 1 V for 15 minutes. For the adhesion improvement investigation, 1mM tannic acid was added into OA and SA electrolytes directly before the electrodeposition, and the condition for deposition was 1 V for 15 minutes. Once the electrodeposition was completed, the electrode was washed with deionized water and dried in the oven. After drying at 60℃ for 24 hours, the modified electrode was ready for electrochemical measurements.

2.2.5. Characterization

The morphologies of the PPy films were characterized by using a scanning electron microscope (SEM) manufactured by Thermo Scientific Apreo. The coatings formed on the copper surfaces were removed from the surface to prepare KBr pellets. FT-IR (IR Prestige-21, Shimadzu) results were obtained in the range from 4000 to 500 cm^{-1}. The Tafel plot was obtained by utilizing linear sweep voltammetry (LSV) in 3.5 wt% NaCl with scan rate 1 mV s^{-1}, starting from -150 mV against

the open circuit potential (OCP) to +150mV over the open circuit potential. The electrochemical impedance spectroscopy (EIS) measurements were performed at a frequency varied from 10^5 to 10^{-2} Hz at open circuit potential and the amplitude of the sinusoidal potential signal was 5 mV. All electrochemical measurements were performed in 3.5 wt% NaCl solution. The adhesion test procedure followed the ASTM D3359 standard.

2.3. Result and discussion

2.3.1. Passivation of the copper

To synthesize the PPy coating onto the metal surface, the electrochemical technique is applied. Many literatures have revealed that the dissolution of metal will affect the electropolymerization of CPs[86][87][88]. In addition, without the formation of the passive layer, some active metals will dissolute during the electrodeposition and fail to complete the process. Therefore, the rate of forming the passive layer becomes vital, which eventually affects the electrosynthesis procedure and the final anti-corrosion performance. In this study, to understand the effect of the dopant, the experiments used OA and SA as dopants for PPy, with various concentrations to optimize the passivation condition. The potential range was set from -0.1 V to 1 V for LSV tests.

Using OA as dopant, as shown in **Fig 2.2**, a clear passivation peak is observed which reveals that the copper oxalate complex is formed[89][90]. During this process, the surface of the polished copper substrate changes its color into a hazy brown. At 0.2 M concentration, the passivation potential, where the current density drops to zero, is around 0.4 V. As concentration increases, the passivation potential shifts gradually to a lower value, from 0.4 V to 0.2 V. When the concentration is 0.9 M, the passivation potential reaches the lowest value at 0.2 V. The potential remains at 0.2 V when further increasing the concentration to 1 M. The low potential at 0.2 V implies that the

formation of the copper oxalate complex is quicker and easier when a higher concentration is applied. The fast formation of the complex can be attributed to the large amount of oxalate anions. In addition, the shift of passivation potential toward lower potential provides a wide potential window for electrodeposition.

In contrast, the SA shows a different result in the LSV as shown in **Fig 2.3**. Firstly, the current density drops for all concentrations at around 0.4 V and keeps at low current but not zero. The probable reason for this result could be the dissolution of copper is happening underneath the passive layer[85]. Also, the drop in the current density can be attributed to the formation of the Cu (II)-salicylate complex[91]. At a low concentration, the current density drops at around 0.4 V and stays flat until 0.7 V. For a higher concentration, the passivation potential shifts to a lower value near 0.3 V. After the flat current density, a second peak is formed. For this second peak, it has been demonstrated from literature that this peak belongs to the polymerization of the salicylate[92]. For the second peak, a higher peak is obtained from increased concentrations (0.7 M, 0.8 M, 0.9 M, and 1.0 M). This could result from the presence of a large quantity of salicylate anions remaining in the electrolyte. Despite the second peak, the passivation potential of the first peak shifts toward a negative direction when higher concentrations are applied, which is like OA system. The results reveal that, with higher concentration, the drop in current density appears quicker at lower potential.

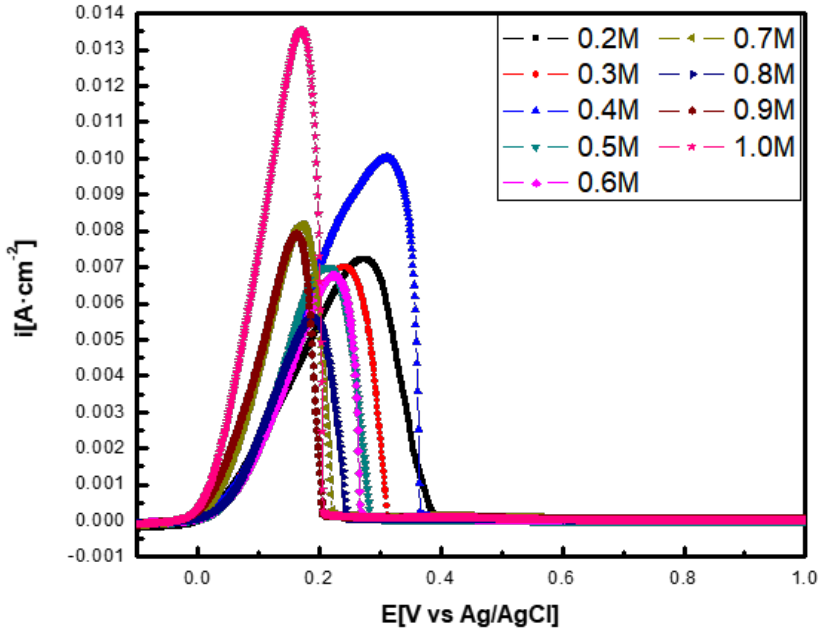

Figure 2.2. The passivation of copper by using OA as dopant with various concentrations

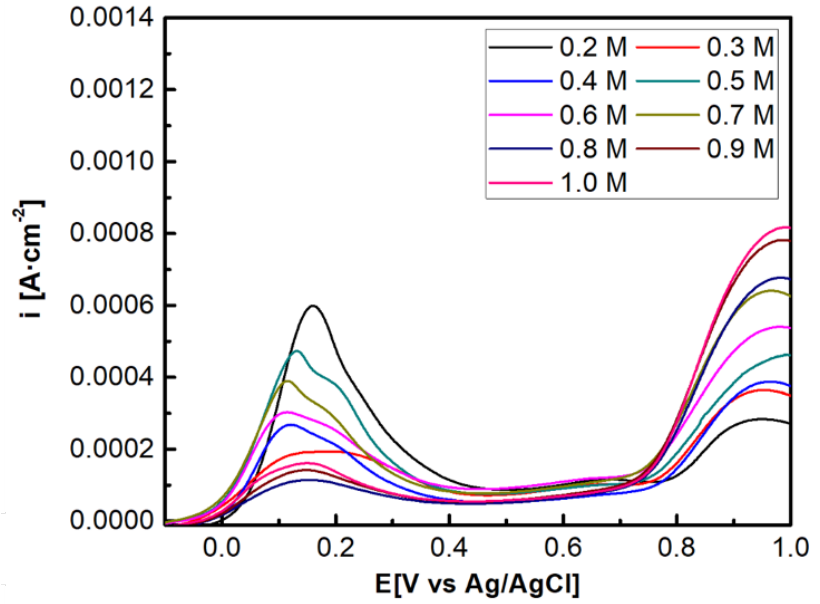

Figure 2.3. The passivation of copper by using SA as dopant with various concentrations

2.3.2. Electropolymerization of pyrrole on copper

A constant potential 1 V was chosen for electrodeposition with 15 minutes. The results were presented by current-time curve in **Fig 2.4**. In the previous passivation study, it reveals that higher concentration will have a fast passivation with low potential. Therefore, four concentrations were selected for OA from 0.7 M to 1 M in electrodeposition. **Fig 2.4(a)** shows the result of the electropolymerization with four different concentrations. At the very beginning, the current density dropped down to zero immediately in a second. This significant drop of the current density demonstrates the passivation of the copper and the development of the copper-oxalate on the copper surface. Then, as time keeps increasing, the current density starts to increase which attributes to the formation of PPy. Gradually, the current becomes flatter, which indicates the steady growth of the PPy.

However, high concentration SA system does not work for the electrodeposition of PPy, as there is no PPy coating formation observed. For example, the current density remains at zero for the entire process for 1 M SA (**Fig 2.4(b)**). A probable reason could be the formation of poly-salicylate film during passivation, which limits the polymerization of conducting polymer. In other words, the existing salicylate anions will affect the formation of the PPy when higher concentration is applied. Therefore, SA at lower concentrations from 0.05 M to 0.2 M were selected to avoid this situation. It revealed that, at lower concentration of SA, the formation of PPy is quicker as evidenced by fast enhancement in current density, indicating growth of the PPy film.

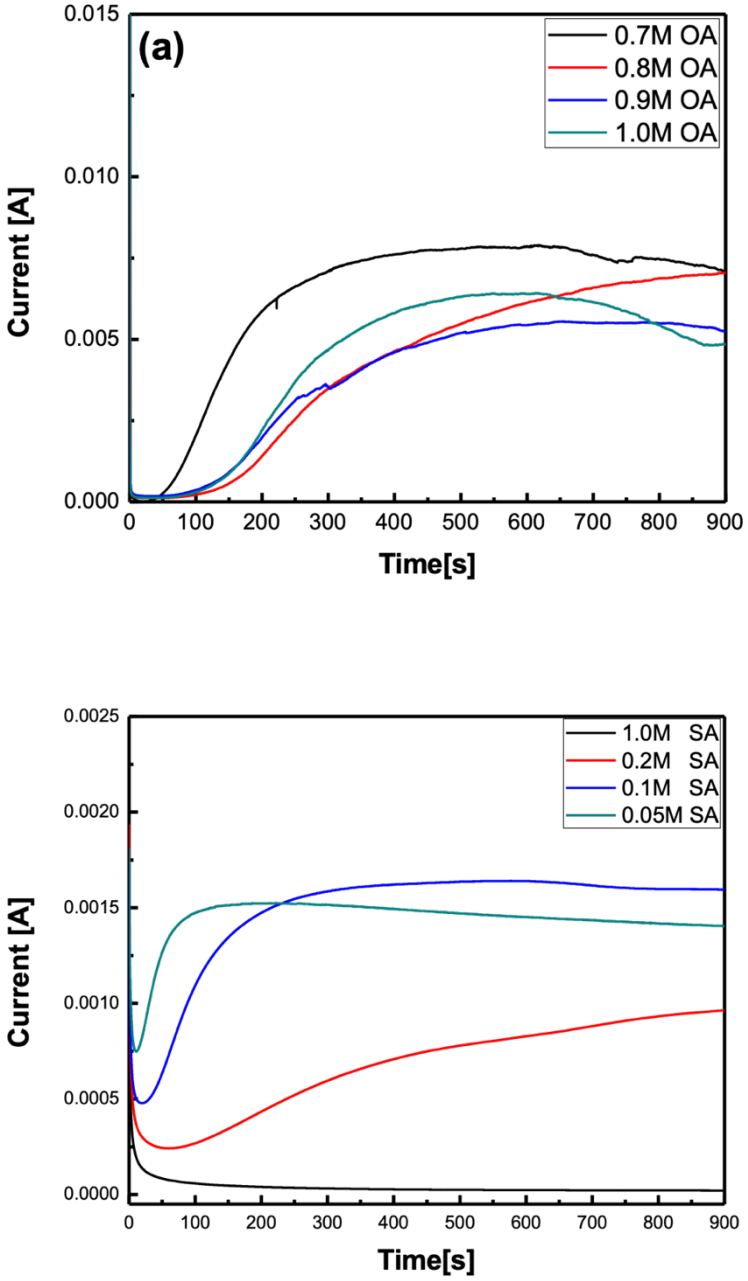

Figure 2.4. The i-t plots for electropolymerization of pyrrole on copper by using (a) OA, and (b) SA as dopants with selected concentrations

All anti-corrosion performance was obtained by using linear sweeping voltammetry in the 3.5% NaCl solution, with applied potential range at ±150 mV away from the open circuit potential. The obtained data then transferred to Tafel plot to further study and compare in **Fig 2.5**. By fitting the polarization curve, corrosion potential (E_{corr}), corrosion current (i_{corr}), corrosion rate (C.R.), and protection efficiency (P.E.) are listed in **Table 2.1**. The corrosion rate[93] is calculated by

$$C.R. = \frac{i_{\text{corr}} \times \text{K} \times \text{EW}}{\text{d} \times \text{A}}$$

Where K is constant for unit transfer, EW is the equivalent weight of the metal, d is the density, and A is the sample area. And for protection efficiency, the equation is displayed below:

$$P.E. = \frac{i_{\text{uncoated}} - i_{\text{coated}}}{i_{\text{uncoated}}} \times 100\%$$

Where $i_{uncoated}$ is the corrosion current of the bare copper, and the i_{coated} is the corrosion current of the PPy coated copper. The results reveal that the corrosion potential of all the coatings is increased. This increased corrosion potential can be attributed to the PPy film on the metal surface which shifts the corrosion potential to more positive value[89]. In addition, the corrosion current of some coatings shifts to much lower value against the bare copper. This shifting of the corrosion current to lower value means a slower corrosion rate. Among four different concentrations of OA, 0.7 M OA has the corrosion potential at 159 mV and a corrosion current of 16.69 μA, which indicates the best corrosion protection among all OA samples. On the other hand, the best corrosion protection for SA is obtained at the 0.05 M concentration, while the corrosion potential is -59.75 mV, and the corrosion current is 11.63 μA. In addition, SA provides better corrosion protection efficiency. As shown in **Table 2.1**, the protection efficiency of the 0.05 M SA (74%) is higher than the 0.7 M OA (62%). This difference could be attributed to the chemical structure of the dopants.

The mobility of the dopant anions in the PPy coating depends on their volume and mass[94]. The When applying the SA as dopant, the higher protection efficiency can be attributed to the π-π stacking of SA with PPy to form lamellar structure[81]. At the same time, the bulkier chemical anions provide resistance against the aggressive Cl^- ions from penetrating the coating and reaches alloy surface.

Table 2.1. Tafel plot results for uncoated copper and PPy-coated copper samples

		E_{corr} (mV vs Ag/AgCl)	i_{corr} (μA/cm^2)	C.R. (mm/year)	P.E. (%)
Bare Cu		-178.87	44.14	0.513	-
PPy/OA	0.7 M OA	159.03	16.69	0.194	62
	0.8 M OA	58.16	115.32	1.339	-161
	0.9 M OA	72.115	123.78	1.437	-180
	1.0 M OA	137.99	23.63	0.274	46
PPy/SA	0.05 M SA	-59.75	11.63	0.135	74
	0.1 M SA	-85.96	23.13	0.268	48
	0.2 M SA	-74.49	12.22	0.142	72

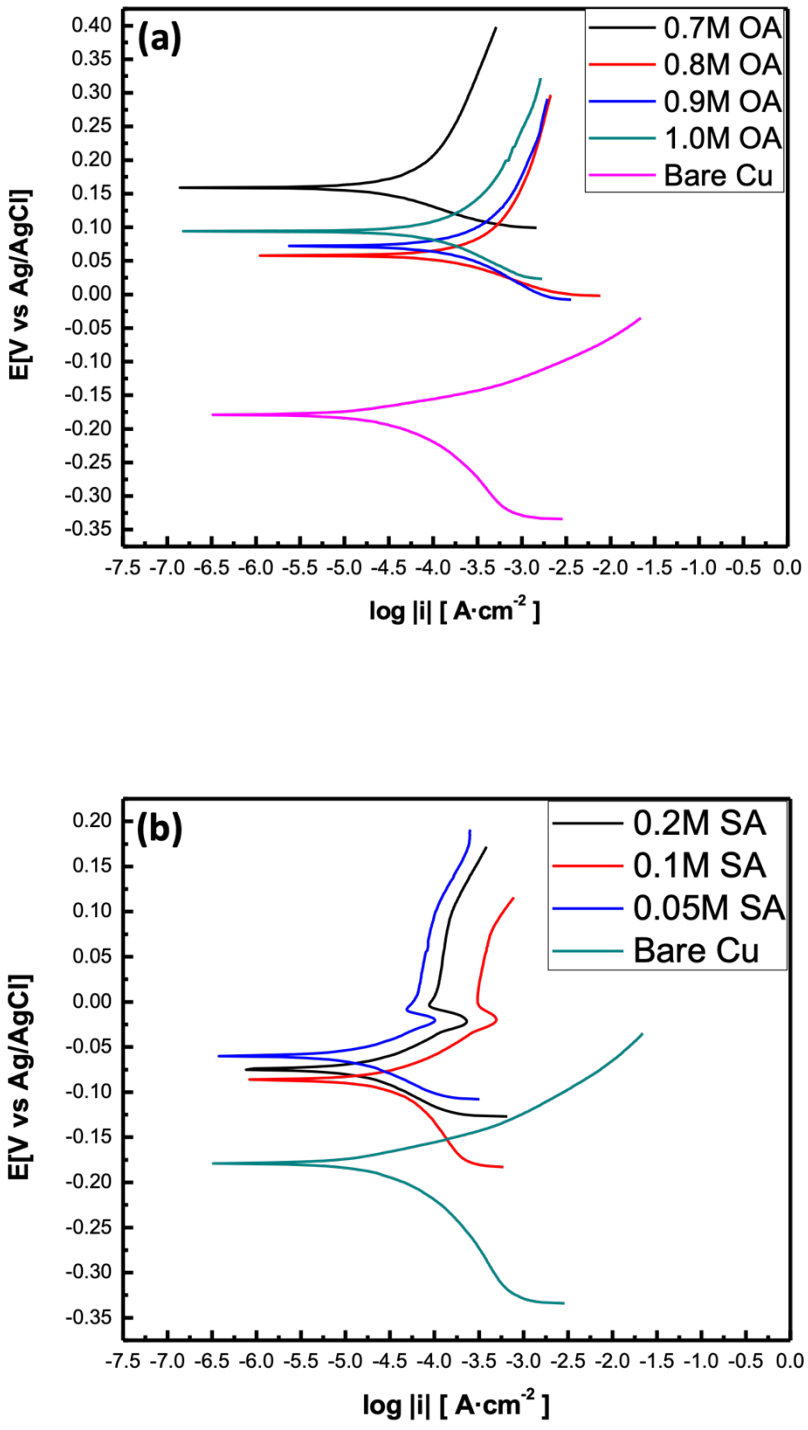

Figure 2.5. The Tafel plots for (a) PPy/OA, and (b) PPy/SA in 3.5% NaCl solution

2.3.3. Adhesion property measurements

Another challenge for the coating is the adhesion of the CP coatings on the metal surface. To provide a long-term protection, the coating should have a good adhesion property to prevent the metal surface from being exposed to a corrosive environment. Few literatures have pointed out that the adhesion promoters (dopamine, alizarin red, and chronotropic acid disodium salt) which possess a structure of catechol can promote the adhesion of the CP coatings[81][95][96][97]. The mechanism is that the phenolic hydroxyl groups interact with the metal ion forming a strong bond between the metal surface and the CP coating to improve the adhesive property. TA, which can form tannic acid-metal complex with metal ion[98][99][100] and a good corrosion inhibitor[101][102], was chosen in this project. TA has a lot of hydroxyl groups and can be considered as a potential adhesion promoter for the CP coatings (Figure 1). OA (0.7 M) and SA (0.05 M) were selected for the adhesion test according to the previous corrosion protection results. The amount for TA in OA electrolyte is 1 mM. While using the same 1 mM TA in SA electrolyte, the coating was not formed. This failure of forming the CP coatings can be attributed to the bulky structure of the TA which restricted the electropolymerization of the PPy. Therefore, the concentration of TA was adjusted to 0.1 mM in the experiment to overcome the failure.

The adhesion test was operated by following the standard ASTM D3359. All results are presented in **Fig 2.6**. For PPy/OA in **Fig 2.6 (a)**, the classification is 0B which means more than 65% of the coating was peeled off. Similarly, the test result of the PPy/SA is 0B, see **Fig 2.6 (c)**. **Fig 2.6 (b)** exhibits the effect when the PPy/OA coating contains TA. Around 85% of the metal surface is still covered by the PPy coating and the classification is upgraded to 3B. In addition, from **Fig 2.6 (d)**, it shows that the adhesion of the PPy/SA/TA coating has been promoted to 3B as well. Based on

the adhesion measurements, it reveals that the TA can be added as adhesion promoter to improve the binding property and the classification can be promoted from 0B to 3B.

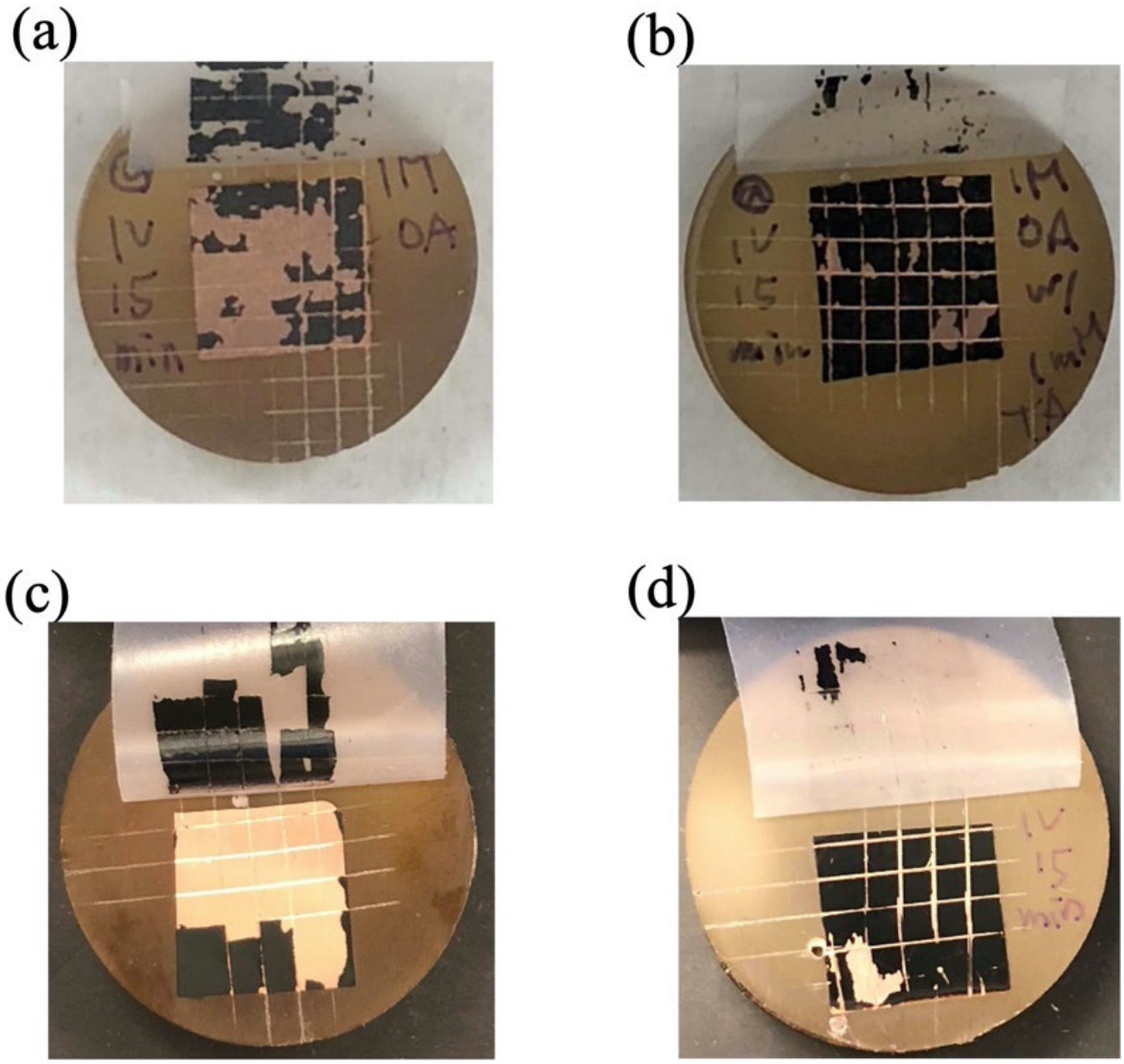

Figure 2.6. The adhesion tests for the coatings of (a) PPy/OA (b) PPy/OA/TA (c) PPy/SA (d) PPy/SA/TA

2.3.4. Characterization of the coating

The morphologies of the PPy coatings with two different dopants and the adhesion promoter were characterized by SEM and shown in **Fig 2.7**. The coating morphology of PPy without adding TA as adhesion promoter can be revealed from **Fig 2.7 (a)** and **(c)**. The flat, cauliflower-like structure can be found on the PPy/OA and the PPy/SA coating, which is similar with other report[103]. But the PPy/SA coating appears with smaller particle size. A probable reason could be the polymerization with a lower current, as shown in **Fig 2.4 (b)**. The current density is around 0.1 mA to 0.15mA. **Fig 2.7 (b)** and **(d)** provide the morphology of the PPy/OA/TA and the PPy/SA/TA coatings, respectively. For the PPy/OA/TA coating, it is clear to see that the cauliflower-like structure is replaced by a granular structure and becomes more compact. On the other hand, for the PPy/SA/TA coating, the morphology remains in a granular structure but slightly in order.

To further verify the coating materials, all samples were tested and analyzed by the FT-IR spectrum. In **Fig 2.8**, the broadband around 3400 cm^{-1} for all samples represents the N-H bond stretching vibration[104]. The peak at 1600 cm^{-1} for all samples can be attributed by the ring stretching vibrations of the C=C bond[105]. In the presence of TA, a board peak around 3200 cm^{-1} from O-H bond will overlap with the N-H bond from PPy. Since TA contains C=O bonds, the overlapping results occur and affect the peak of the C=C bond from PPy around 1600 cm^{-1}. Additionally, an observed peak at 1176 cm^{-1} is due to the C-O bond from TA[106]. Thus, the FT-IR results reveal that the coating of PPy with different dopants and the same promoter is successfully obtained on the copper surface by electrodeposition.

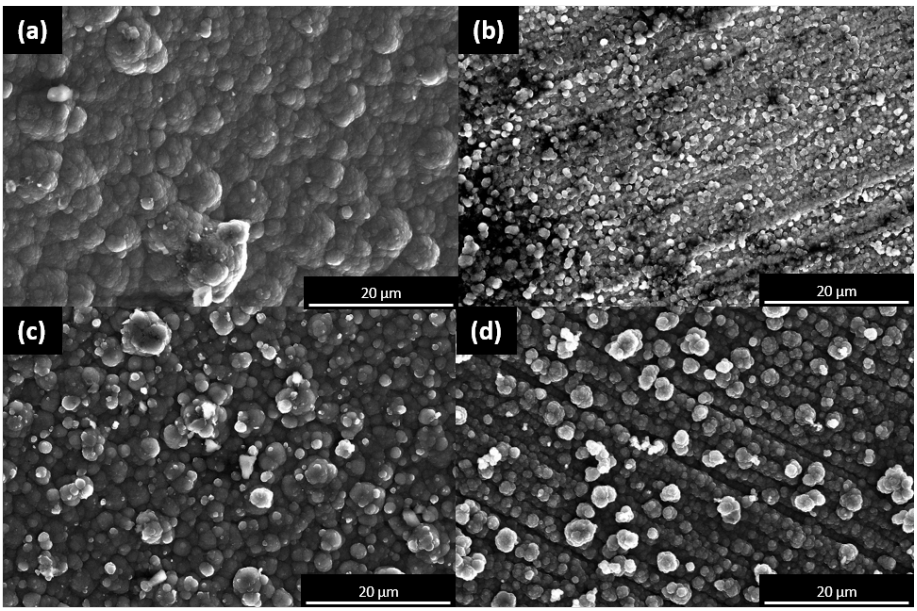

Figure 2.7. SEM images of PPy coatings with and without TA: (a) PPy/OA (b) PPy/OA/TA (c) PPy/SA (d) PPy/SA/TA

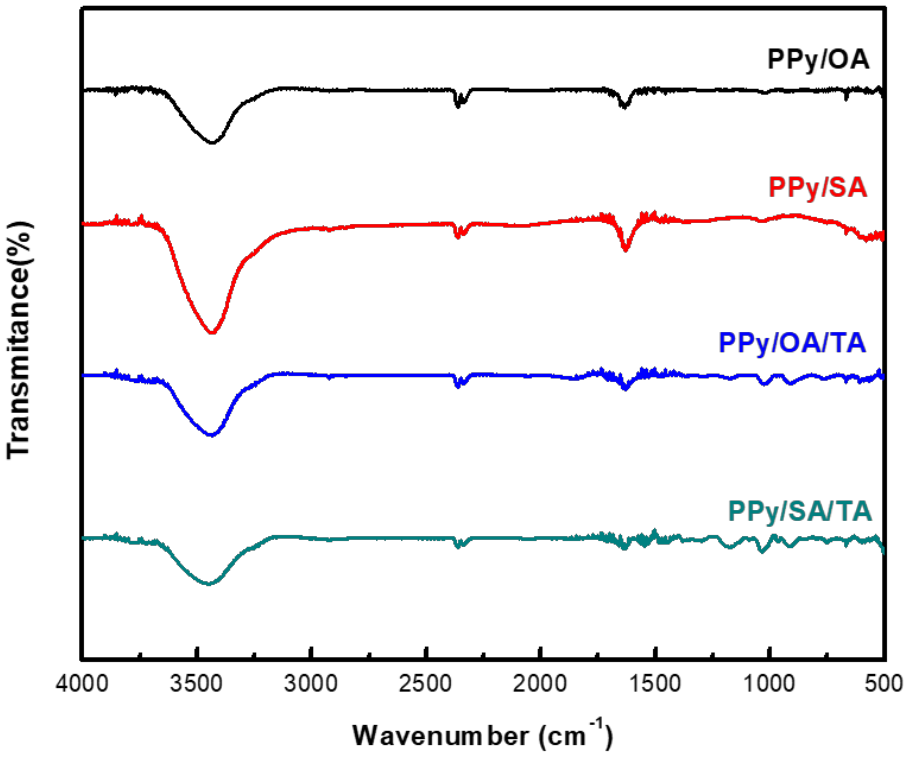

Figure 2.8. The FT-IR spectra of the PPy coatings

2.3.5. Corrosion protection after adding TA as adhesion promoter

Corrosion protection was studied after adding TA as adhesion promoter. The Tafel plots are presented in **Fig 2.9** and values are listed in **Table 2.2**. The corrosion potential of the PPy/OA/TA and the PPy/SA/TA coatings keeps at positive value against the bare copper. In addition, the protection efficiency of the PPy/OA/TA and PPy/SA/TA coatings are 94% and 85% respectively. The protection efficiency of the PPy/OA/TA coating increases 32% and reach the highest efficiency among all the coatings. The presence of the TA in the PPy coating, due to the bulky chemical structure, restricts the mobility of the corrosive ions from flowing into the metal surface. This result indicates that TA not only improves the adhesion of PPy film, but also improves the anti-corrosion performance significantly.

Table 2.2. Tafel plot results for PPy-coated sample with and without adding TA

	E_{corr} (mV vs Ag/AgCl)	i_{corr} ($\mu A/cm^2$)	C.R. (mm/year)	P.E. (%)
Bare Cu	-178.87	44.14	0.513	-
PPy/OA	159.03	16.69	0.217	62
PPy/OA/TA	127.19	2.75	0.032	94
PPy/SA	99.32	4.51	0.052	90
PPy/SA/TA	2.99	6.79	0.078	85

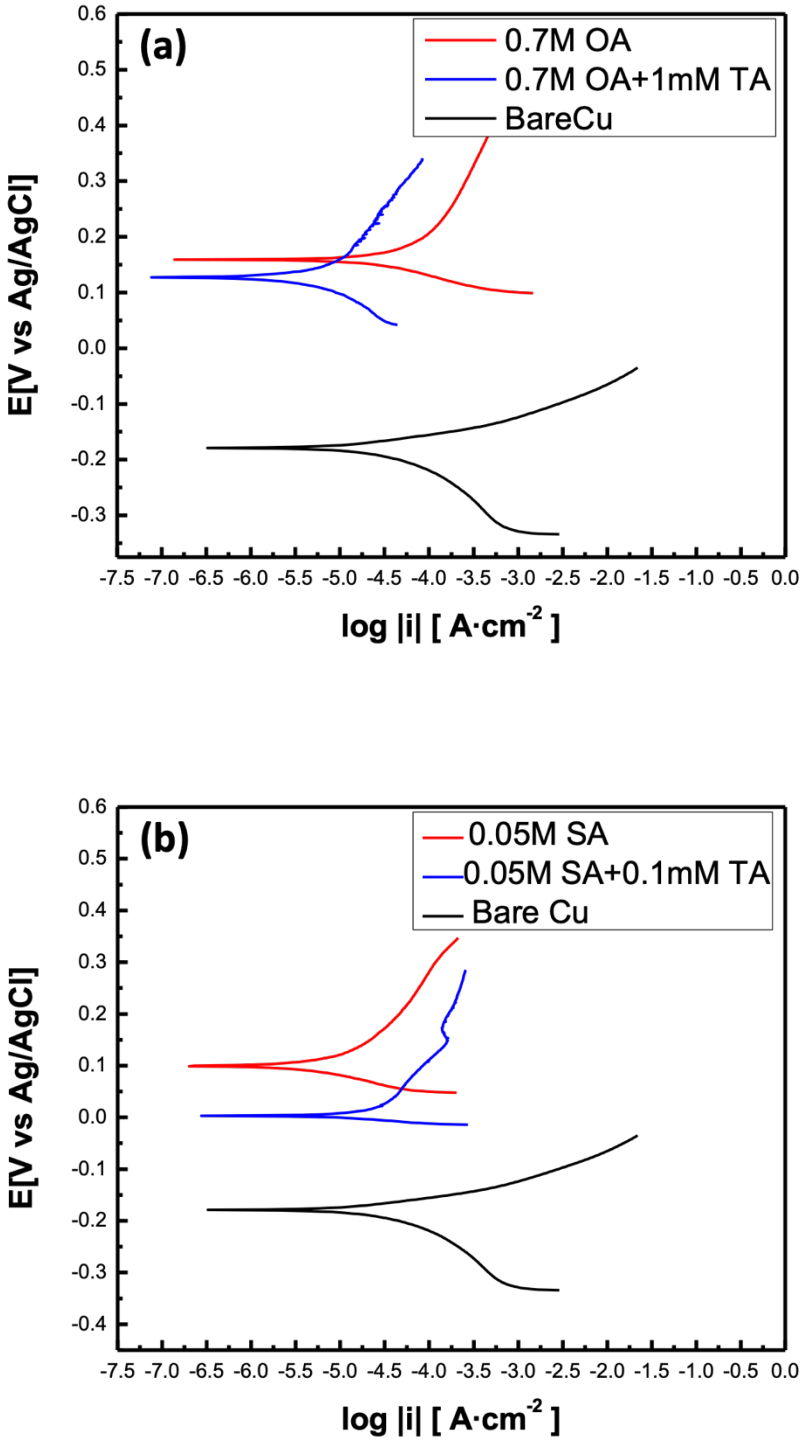

Figure 2.9. The Tafel plots for (a) PPy/OA/TA, and (b) PPy/SA/TA at 1 $mV \cdot s^{-1}$ in 3.5% NaCl

Electrochemical impedance spectroscopy (EIS) is a damage-free and versatile test. It can provide more information to evaluate the anti-corrosion performance and protection mechanism between the PPy coating and metal surface. In **Fig 2.10**, PPy/OA, PPy/OA/TA, PPy/SA, PPy/SA/TA, and bare copper were compared. The corresponding equivalent circuits are presented in **Fig 2.11**, which consists of the solution resistance (R_s), the coating resistance (R_f), the charge transfer resistance (R_{ct}). Additionally, since the behavior of the coating is uncertain, the capacitance was replaced by the constant phase element (CPE) which are coating capacitance (CPE_f) and the charge transfer capacitance (CPE_{ct}), respectively. The impedance of CPE can be written as

$$Z_{CPE} = [Y_0(j\,\omega)^n]^{-1}$$

Where, Y_0 and n ($0 < n < 1$) are frequency independent. When n = 1, the case can be considered as capacitor. On the other hand, if n = 0, the case is a resistor[107]. The R_{total} is the total impedance of the coating which can be calculated as $R_{\text{total}} = R_{\text{f}} + R_{\text{ct}}$. **Table 2.3.** showed the resistance parameters for the coated and un-coated samples obtained from the fitting data.

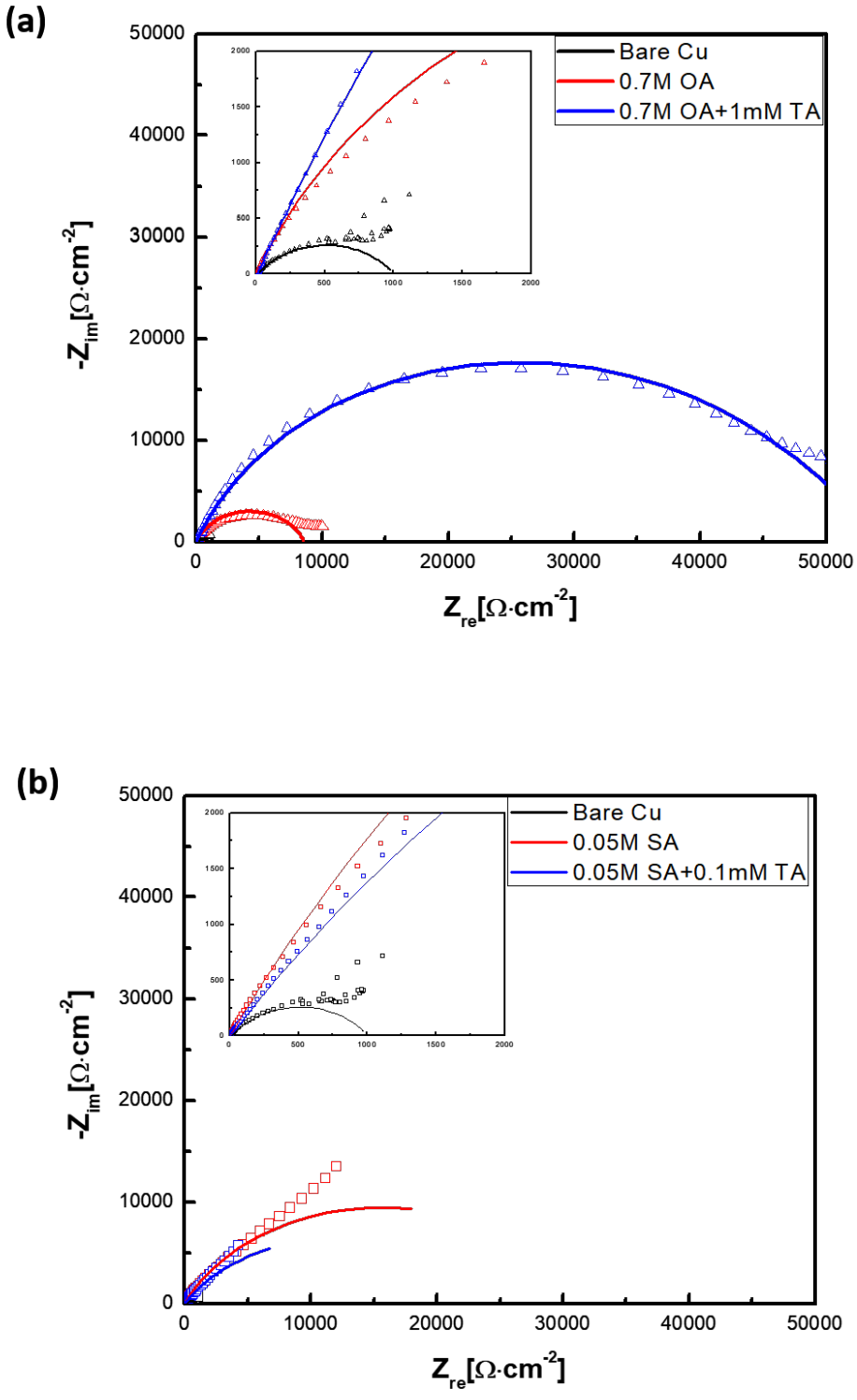

Figure 2.10. The Nyquist plots for (a) PPy/OA/TA, and (b) PPy/SA/TA in 3.5% NaCl solution

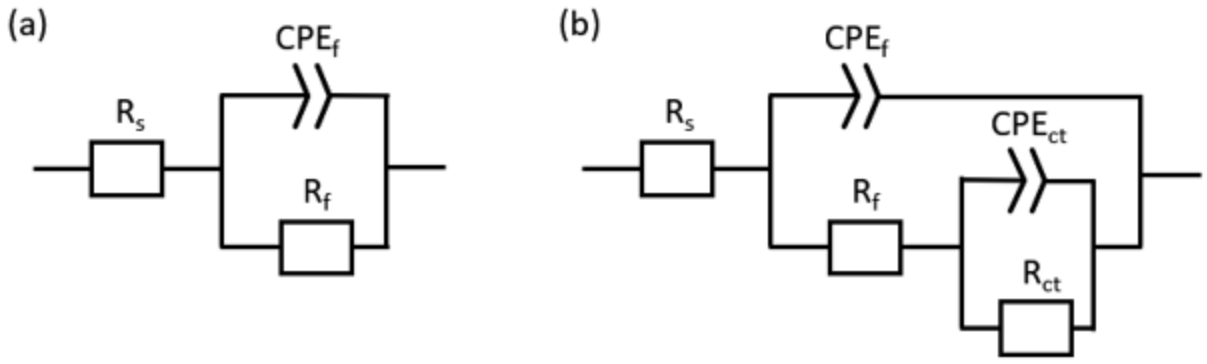

Figure 2.11. The equivalent circuit models for (a) uncoated (b) coated sample

For the bare copper, the total impedance R_{total} value is 0.98 x 10^3Ω cm^2. When comparing the bare copper with the coatings, the R_{total} of all coatings showed a better resistance indicating excellent corrosion protection of the coatings. In the OA system, the R_{ct} values increased from 9.24 x 10^3Ω cm^2 for PPy/OA coating to 2.40 x 10^4Ω cm^2 for PPy/OA/TA coating. This indicates that the presence of TA exhibited better charge transfer resistance than PPy/OA coating. The coating resistance R_f reflects the barrier ability of the coating in the corrosive environment. Therefore, the R_f value is a significant value to evaluate the anti-corrosion performance of the coating. Likewise, the R_f of the PPy/OA/TA coating showed higher resistance than the PPy/OA coating indicating a better barrier effect against the electrolyte due to the addition of the TA dopant. The result showed that the TA as an adhesion promoter in the OA system could further improve the corrosion protection of the coating. On the other hand, in SA system, the Rct of the PPy/SA/TA coating decreased from 4.51 x 10^3Ω cm^2 to 8.43 x 10^3Ω cm^2 for the PPy/SA coating. The declining charge transfer resistance indicated the TA adhesion promoter did not provide better protection but improved the adhesion only. The R_f values of the PPy/SA and the PPy/SA/TA coatings remain with a close coating resistance and not be affected by the TA adhesion promoter which indicated

the barrier effect is stable. Overall, The PPy/OA/TA coating obtained the highest R_{total} resulting in better corrosion protection among all coatings.

Table 2.3. EIS fitting data

	R_s (Ω cm^2)	CPE_f (F cm^{-2})	n	R_f (Ω cm^2)	CPE_{ct} (F cm^{-2})	n	R_{ct} (Ω cm^2)	R_{total} (Ω cm^2)
Bare	16.60	2.54×10^{-4}	0.612	-	-	-	0.98×10^{3}	0.98×10^{3}
PPy/OA	7.43	2.05×10^{-6}	0.827	1.59×10^{3}	1.79×10^{-6}	0.433	9.24×10^{3}	1.08×10^{4}
PPy/OA/TA	10.63	1.89×10^{-6}	0.779	4.99×10^{4}	1.96×10^{-4}	0.794	2.40×10^{4}	7.39×10^{4}
PPy/SA	6.53	1.71×10^{-4}	0.720	1.81×10^{4}	5.00×10^{-9}	0.339	8.43×10^{3}	2.65×10^{4}
PPy/SA/TA	7.47	5.07×10^{-4}	0.645	1.75×10^{4}	1.32×10^{-6}	0.438	4.51×10^{3}	2.20×10^{4}

2.3.6. The comparison of protection efficiency

The corrosion protection of this work is further compared with other reports shown in **table 2.4**. All materials used in the coating were polypyrrole or polyaniline. In the corrosion current density, this work did not give the lowest value which indicated the protection efficiency is relatively low. In other words, the low protection efficiency represents a higher corrosion rate. However, when comparing with the corrosion potential, this work presented the highest corrosion potential 127.19 mV vs Ag/AgCl which indicated the coating keeps the metal surface in passivation and provides the protection to the surface before it starts to corrode. In other words, the tendency of corrosion in this work is relatively low.

Table 2.4. The comparison of corrosion protection efficiency with existing reports

Authors	Materials	Technique	E_{corr}	i_{corr}	P.E.(%)
Annibaldi et al.[108]	PPy/SA	CV	-76 (mV vs SCE)	5.17 ($\mu A/cm^2$)	--
Jafari et al.[109]	PAni/graphene	CV	-0.234 (mV vs Ag/AgCl)	0.1 ($\mu A/cm^2$)	98
Carragher et al.[110]	PPy/DBS and PPy/Tar bilyer	Potentiostatic	-65 (mV vs SCE)	0.12 ($\mu A/cm^2$)	94
Wan et al.[111]	PPy/ BTA/silica	CV	0.0724 (mV vs SCE)	0.091 ($\mu A/cm^2$)	98
This work	PPy/OA/TA	Potentiostatic	127.19 (mV vs Ag/AgCl)	2.75 ($\mu A/cm^2$)	94

∗BTA = benzotriazole; Tar = tartrate; DBS = dodecylbenzene sulfonate

2.4. Conclusion

The PPy had been successfully electrodeposited on the copper surface using two different dopants (OA and SA). The potentiodynamic scan was utilized for studying the behavior of the copper passivation. The Tafel plots showed that all PPy-coated samples performed better corrosion protection. When comparing two dopants, the PPy/SA has higher protection efficiency revealing that bigger dopant anions, which contained benzene ring, and π-π stacking of the aromatic rings provide better corrosion protection efficiency and lower corrosion rate. Furthermore, the adhesion strength was discussed due to the poor adhesion property of the PPy/OA and the PPy/SA coatings. In this research, the TA was introduced into the electrolyte with the monomer directly to investigate the promotion of the adhesion enhancement. After adding TA as promoter, the adhesion test for both dopants can be improved from 0B to 3B, which promotes around 50% adhesion strength. Also, the corrosion protection is not affected by the promoter and even provides better corrosion efficiency. The EIS measurement confirms that TA provides a better corrosion resistance for the coating due to its large chemical structure which can prevent the penetration of the corrosive species. In FT-IR of PPy/OA system, there is no obvious change for the peaks after addition of

TA. However, the total resistance of PPy/OA/TA coating increased, compared to PPy/OA coating, indicating better corrosion protection with addition of TA. In contrast, there is a change for the peak after addition of TA in FT-IR of PPy/SA system. The total resistance of PPy/SA/TA coating decreased, compared to PPy/SA coating which indicated the weaker corrosion protection after adding TA. Among all the coatings, the PPy/OA/TA coating gives the highest protection efficiency at 94% and keeps a good adhesion. Overall, the electropolymerization of the PPy on copper by dual dopants is successful. TA, as adhesion promoter, can improve the adhesion of the coating and provide a better anti-corrosion performance.

Chapter 3

The sulfonic acid doped polypyrrole on the influence of the corrosion protection for AA2024-T3

3.1. Introduction

The demand for aluminum alloy in the aerospace industry is enormous due to its superior properties such as light weight, high strength, and fabricability[112]. However, the major issue in the application is the prevention of corrosion. To survive corrosive conditions, a typical coating system is applied including three layers[113]. The first layer is the pretreatment of the substrate with the function of corrosion protection and adhesion improvement. A common technique is chromate conversion coating (CCC). The following layer contains hexavalent chromium Cr (VI) is the primer that provides the major corrosion protection for the substrate. The final layer, the topcoat, serves as a barrier to overcome the influence of the environment. Due to the carcinogenic effects and toxic nature, the utilization of hexavalent chromium, or chromate, has been restricted[114][115]. Recently, new alternative materials have been developed including conducting polymers (CPs). The application of CPs in anti-corrosion performance for various metals and alloys has been widely studied[37][30][116][117][118][48]. Most of the proposed mechanisms for CP coating is the anodic protection which allows the alloy surface to remain passive. Also, the coating can act as a physical barrier to prevent the penetration of aggressive elements[119]. The application of polypyrrole includes batteries[120], supercapacitor[121], sensor/biosensor[122], biomedical[123][124], and corrosion[125]. Among different synthesis processes, the advantage of the electrochemical synthesis is the direct formation of a film on the substrate without any additives. The morphology and roughness of the coating are also controlled

by dopants, electrochemical method, monomer concentration, and pH value[126]. Liu and Oliveira investigated the effect of electrolytes on the electrochemical synthesis of PPy and its corrosion protection[127]. Scanning Electron Microscopy (SEM) revealed that the morphology of the coating was affected by different electrolytes. Among the three electrolytes, PPy film containing tartaric acid had a better corrosion protection due to the highest uniformity of the surface. Jiang et al. prepared PPy coating doped with camphorsulfonic acid (CSA) on 304SS by galvanostatic method[128]. The PPy-CSA coating exhibited better corrosion resistance in comparison with small dopant (SO_4^{2-}). Furthermore, the PPy-CSA coating preserved a robust corrosion resistance after 660 h in Sulfuric acid solution. Vera et al. evaluated the corrosion performance of different bulky anions (p-toluenesulfonate, benzebesulfonate, and dodecylsulfonate) doped PPy on stainless steel[129]. The result demonstrated that the surface roughness was affected by the molecular size of the dopant which influence the corrosion protection. Another study focused on the corrosion behavior of Q235 steel by PPy film doped with different dopants was presented by Zhou et al[130]. Dopants included oxalic acid, p-toluenesulfonic acid, sulfamic acid, phytic acid, and sodium dodycylbenzenesulfonate. The corrosion resistance of all PPy-coated samples showed a significant improvement than bare Q235 steel. And, the PPy doped with sodium dodycylbenzenesulfonate presented the smallest particle size with the highest film density then gave the best anti-corrosion performance.

2-naphthalenesulfonic acid (2NS) has been recognized as a good corrosion inhibitor in aggressive environments. Vračar and Dražić found three naphthalenesulfonic acids blocked hydrogen evolution reaction and acted as corrosion inhibitors[131]. The difference number of functional groups substituted on benzene and the concentration of the acids affected the inhibitive efficiency. The corrosion inhibiting mechanism of benzotriazole (BTA) and 2NS were studied by Hu et

al[132]. The combination of BTA and 2NS presented high charge density and large conjugate π bond to achieve the most effective inhibitor. On the other hand, the influence of the 2NS as dopant for electrodeposition was reported[133][134][135]. Yet, the anti-performance of 2NS-doped PPy coating has not been fully investigated. The present study will therefore focus on the electrodeposition of PPy by applying 2NS as dopant. In order to compare the influence of chemical structure, sulfuric acid and p-toluenesulfonic acid were selected. The AA2024-T3 has been chosen as working electrode with applying a constant potential for electrodeposition of PPy.

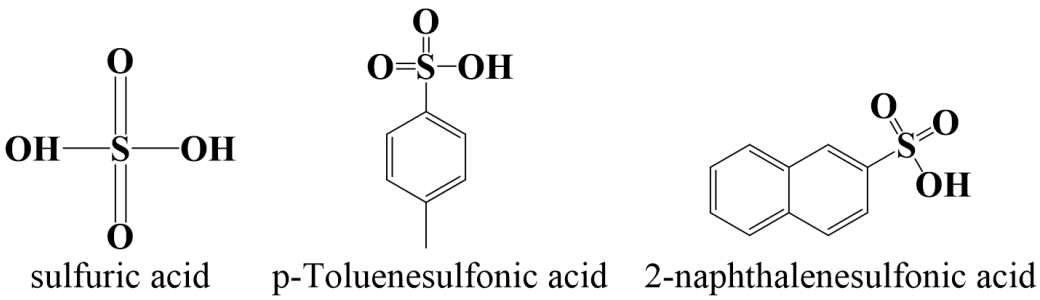

Figure 3.1. The chemical structure of three dopants used in the electrodeposition of PPy

3.2. Experimental

3.2.1. Reactants and Materials

The AA2024-T3 was purchased from Online Metals and the size was cut into 1 cm × 3 cm× 0.1 cm. The AA2024-T3 composition includes 93.5% Al, 0.1% Cr, 3.8-4.9% Cu, 1.2-1.8% Mg, 0.5% Fe, 0.3-0.9% Mn, 0.5% Si, 0.25% Zn, and 0.15% Ti. Pyrrole (Py) was purchased from ACROS ORGANICS. Sulfuric acid (SA) and sodium chloride (NaCl) were purchased from VWR chemicals. p-Toluenesulfonic acid monohydrate (pTSA) was purchased from Beantown Chemical. 2-Naphthalenesulfonic acid (2NS) was purchased from Thermo Scientific. All solutions were prepared by using deionized water.

3.2.2 Electrodeposition of PPy on AA2024

Three dopants were selected including SA, pTSA, and 2NS. Prior to electrodeposition, sandpaper from 800, 1000, to 1200 grits was used to polish the AA2024-T3 and then masked with adhesive tape to get a 1cm^2 surface area exposed on both sides. The electrolyte contains 0.1M pyrrole with different concentrations of dopant 0.05M, 0.1M, and 0.2M, respectively. The three-electrode system, including AA2024 as a working electrode, platinum mesh as a counter electrode, and Ag/AgCl as a reference electrode, was applied for the electrodeposition. A constant potential at 1V for 15 min was utilized during the electrodeposition by the CH Instrument (CHI 760D). The PPy-coated electrode was rinsed by DI water after electrodeposition and then placed into the oven for 24 hours at 60 ℃.

3.2.3. Topcoat with spray paint

The PPy-coated samples were sprayed with spray paint. After the curing process, the samples were masked with adhesive tape to get a 1 cm^2 surface area exposed for both sides and then ready for electrochemical measurement.

3.2.4. Characterization of PPy coating

Scanning electron microscope (SEM), Thermo Scientific Apreo, was used to study the morphologies of the PPy films. The coatings formed on the AA2024 surfaces were collected from the surface to prepare KBr pellets. FT-IR (IR Prestige-21, Shimadzu) results were obtained in the range from 4000 to 500 cm^{-1}.

3.2.5. Electrochemical measurement of PPy coating

The protective properties of the PPy coatings were examined by applying linear sweep voltammetry (LSV) at a 1 mV s^{-1} scan rate. A potential range of ± 150 mV versus the open circuit potential (OCP) was applied in 3.5 wt% NaCl. The long-term durability test was tested by detecting the fluctuation of open circuit potential (E_{ocp}) in NaCl solution for 48 hours. The electrochemical impedance spectroscopy (EIS) measurements were carried out at open circuit potential in a frequency range from 10^5 to 10^{-2} Hz, with a 5 mV amplitude sinusoidal signal. All electrochemical measurements were performed in 3.5 wt% NaCl solution. All measurement was carried out by the CH Instrument (CHI 760D) using Electrochemical Analyzer software.

3.3. Result and discussion

3.3.1. Electrodeposition of different dopants with various concentrations on AA2024-T3

Three dopants that contain sulfate were studied and the chemical structures were presented in **Fig. 3.2**. Experiments involving different concentrations (0.05M, 0.1M, and 0.2M) for each dopant have been carried out to determine optimized conditions for pyrrole electrodepositing on the AA2024-T3 surface. In the electrodeposition, a constant potential of 1V was applied for 15 minutes and the result was displayed by the current-time plot. In general, the curve can be separated into three parts: (1) a quick drop in the current value at the beginning of the experiment which indicates the passivation of the alloy surface, (2) follow by the growth of the current representing the oxidation of pyrrole and polymerization of the pyrrole, and (3) a flat curve after the increase of current reveals the growth of the PPy film. For SA as the dopant in **Fig. 3.2(a)**, there was no significant increase in current after the quick drop which reveals the failure of PPy electrodeposition. Only a few PPy can be seen from the 0.2M SA but the surface is not fully covered by the polymer. On the other hand, pTSA and 2NS, in **Fig 3.2 (b)** and **(c),** showed a current

increase after the quick drop giving evidence of the PPy electrodeposited on the AA2024-T3 successfully. A higher current value achieved from 0.2M pTSA and 0.2M 2NS can be attributed a higher concentration of dopant favor diffusion and a lower induction time is obtained[136].

The unsuccessful result of SA is attributed to the presence of Al2O3 which limits the electron transfer and then causes the failure of the formation of PPy[137][138]. On the other hand, the anionic mediators structure of pTSA and 2NS acted like a surfactant, helping entree of the PPy monomer into the defect and/or pores of oxide layer[139].

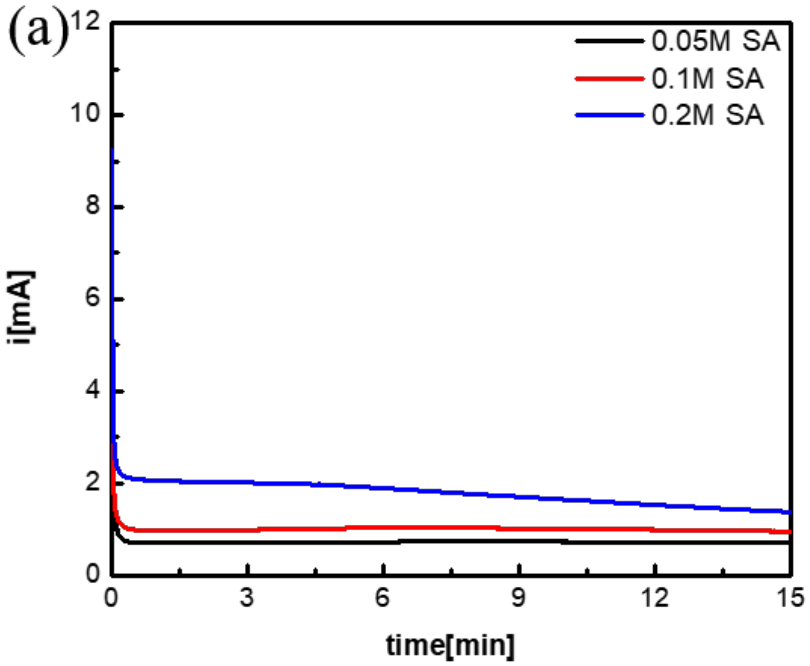

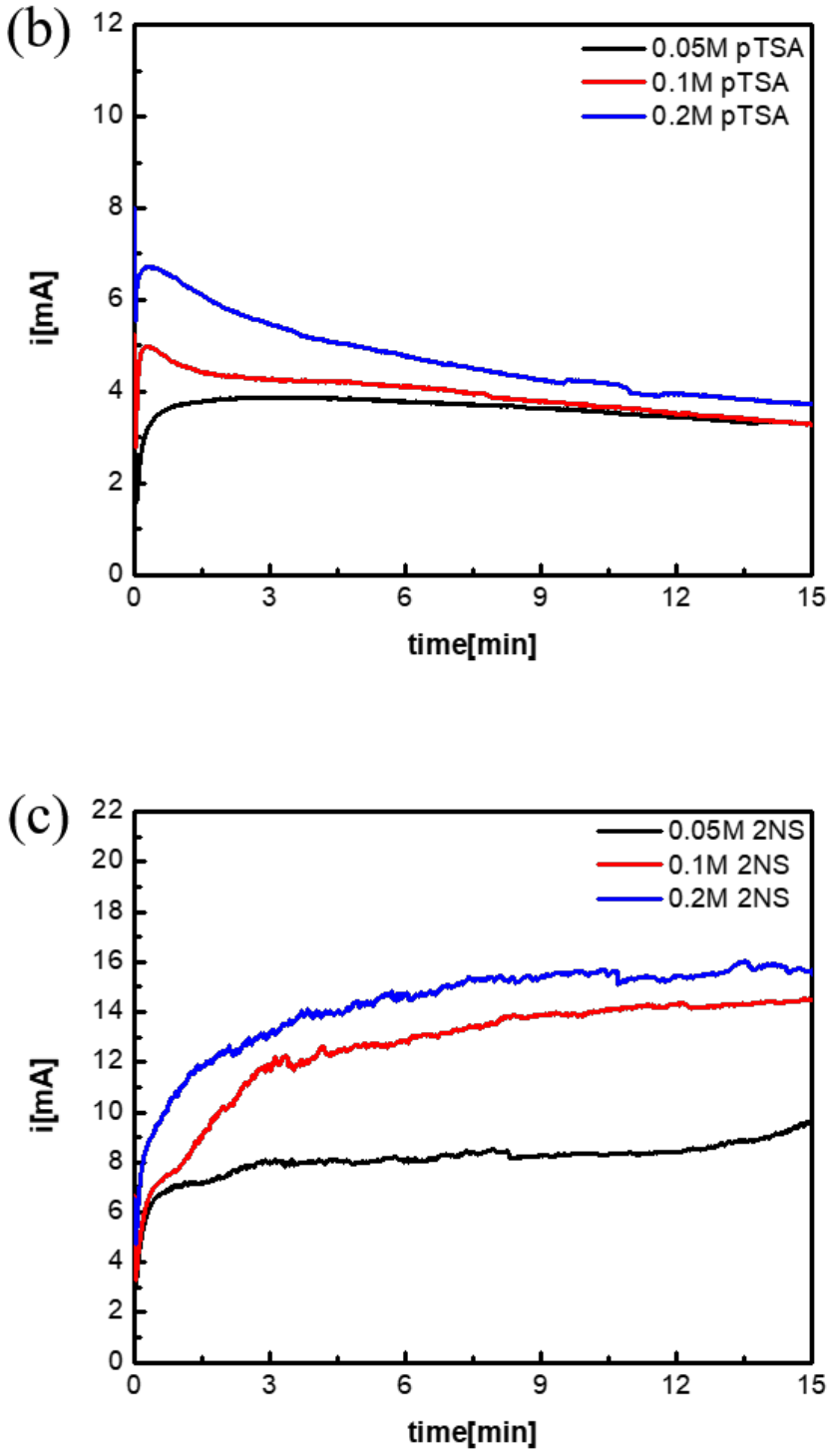

Figure 3.2. The result of electrodeposition presented in the i-t curves with different dopants (a) SA (b) pTSA and (c) 2NS

3.3.2. Characterization of the coating

The modification of the AA2024-T3 surface by PPy was measured utilizing FT-IR and the spectra result is shown in **Fig. 3.3**. It showed that two dopants exhibited similar curves in the spectra. The broad band around at 3452 cm^{-1} and 3442 cm^{-1} of two samples were attributed to the N-H stretching vibration[140]. Additionally, peak at 1594 cm^{-1} and 1595 cm^{-1} are corresponded to the C-H stretching[141]. The peak at 580 cm^{-1} was attributed to the C-S and C-O stretching vibrations. The peak at 1406 cm^{-1} was corresponded to S=O stretching vibrations of sulfonate group[142]. Peaks around 700-900 cm^{-1} are attributed to C-H bending.

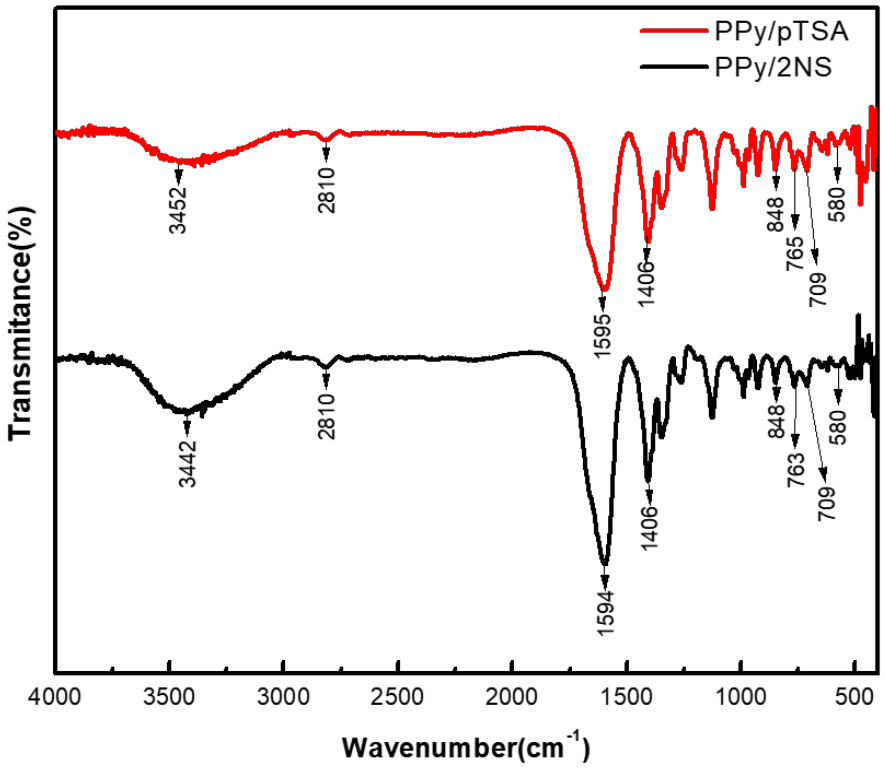

Figure 3.3. FT-IR spectrums of PPy/pTSA and PPy/2NS

Fig 3.4. presents the SEM images of the deposited polypyrrole film prepared with two dopants. Both samples displayed a typical cauliflower-shaped structure with microscopic grains which agree with other reports[130]. The difficulty of dopant intercalation in the disordered polymeric chain led to the formation of the cauliflower structure[143]. The PPy/2NS has more aggregated grains, see **Fig. 3.4(c)**.

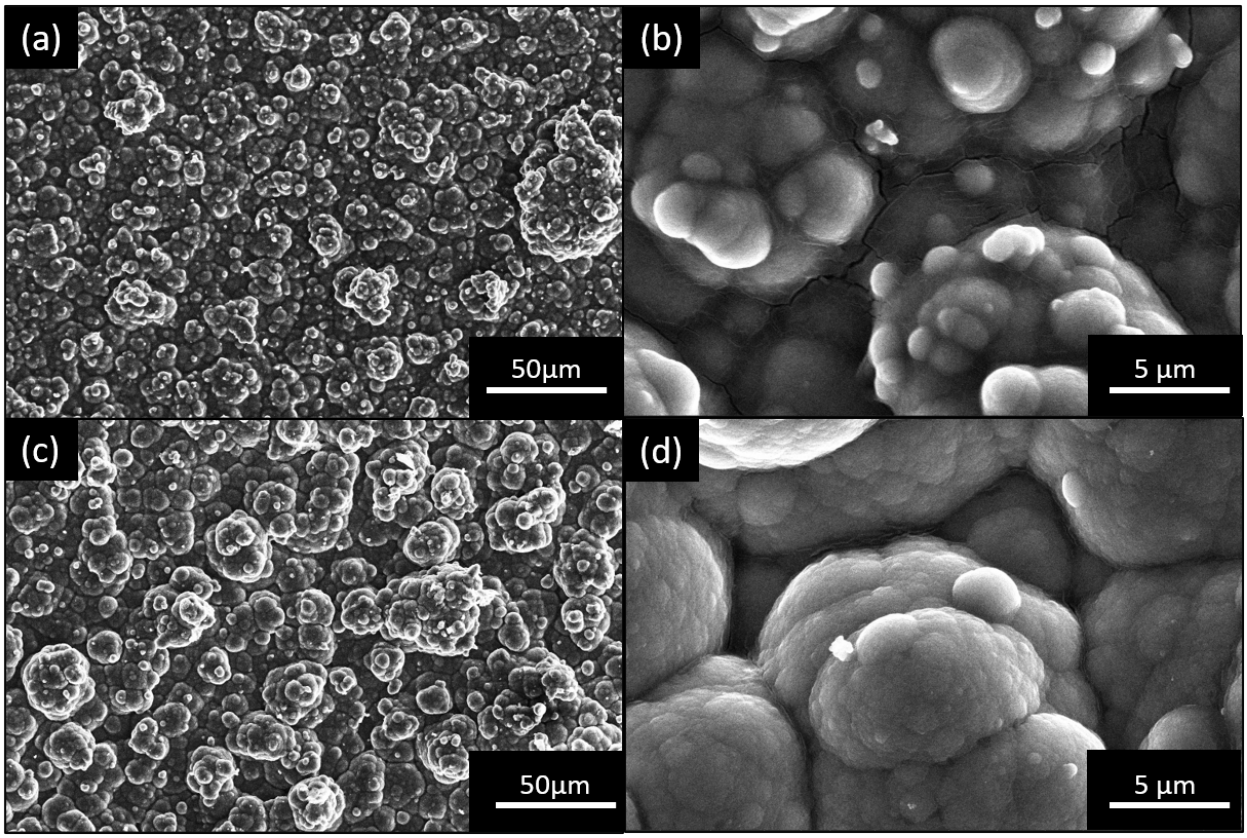

Figure 3.4. SEM images of the PPy coating with different dopants (a-b) PPy/pTSA and (c-d) PPy/2NS

3.3.3. The corrosion protection of different dopants

Potentiodynamic polarization curves of PPy/pTSA and PPy/2NS are showed in **Fig. 3.5**. **Table 3.1** presented the Tafel parameters after fitting the polarization curves including corrosion potential

(Ecorr), corrosion current (Icorr), corrosion rate (C.R.), and protection efficiency (P.E.). All corrosion protection was tested in the 3.5 wt% NaCl solution, with potential scanned at ±150 mV versus open circuit potential at a scan rate of 1 $mV \cdot s^{-1}$. The corrosion rate is calculated by following equation:

$$C.R. = \frac{i_{\text{corr}} \times \text{K} \times \text{EW}}{\text{d} \times \text{A}}$$

Where K is constant for unit transfer, EW is the equivalent weight, d is the density, and A is the area of the sample. And for protection efficiency, the equation is displayed below:

$$P.E. = \frac{i_{\text{uncoated}} - i_{\text{coated}}}{i_{\text{uncoated}}} \times 100\%$$

Where $i_{uncoated}$ is the corrosion current of the Pure AA2024-T3, and the i_{coated} is the corrosion current of the PPy coated sample. For PPy/pTSA in **Fig. 3.5(a)**, the corrosion potential of three concentrations shifted to more positive value against pure AA2024-T3 indicating the PPy coating facilitated the anodic protection. At the same time, the corrosion currents decreased implying a better corrosion resistance. It is clear that 0.2M PPy/pTSA exhibited the best corrosion protection efficiency (41.10%) with the lowest corrosion rate (0.466 mm/yr) among three concentrations. On the other hand, the PPy/2NS with different concentrations are presented in **Fig. 3.5(b)**. In contrast to the pTSA, superior results are obtained from the 2NS dopant. Clearly, corrosion potential and corrosion current had significantly improved when applying 2NS as dopant. The 0.1M 2NS presented the best anti-corrosion performance with the corrosion potential at -15.86 mV and a corrosion current of 5.53 $\mu A \cdot cm^{-2}$. Together, the results demonstrate two things. First, all coated samples showed more positive corrosion potential and more negative corrosion current value than pure AA2024-T3, revealing that PPy coating act as an effective barrier and enhances the corrosion

resistance of the AA2024-T3. Second, the protection efficiency of 0.1M 2NS (96.19%) is higher than 0.2M pTSA (41.10%) indicating the chemical structure of the dopant has an impact on the corrosion protection. The studies we have performed showed that, with a larger chemical structure, the resistance of the 2NS coating has better anti-corrosion performance against aggressive ions. Consequently, the 0.2M pTSA and the 0.1M 2NS were selected for additional investigation.

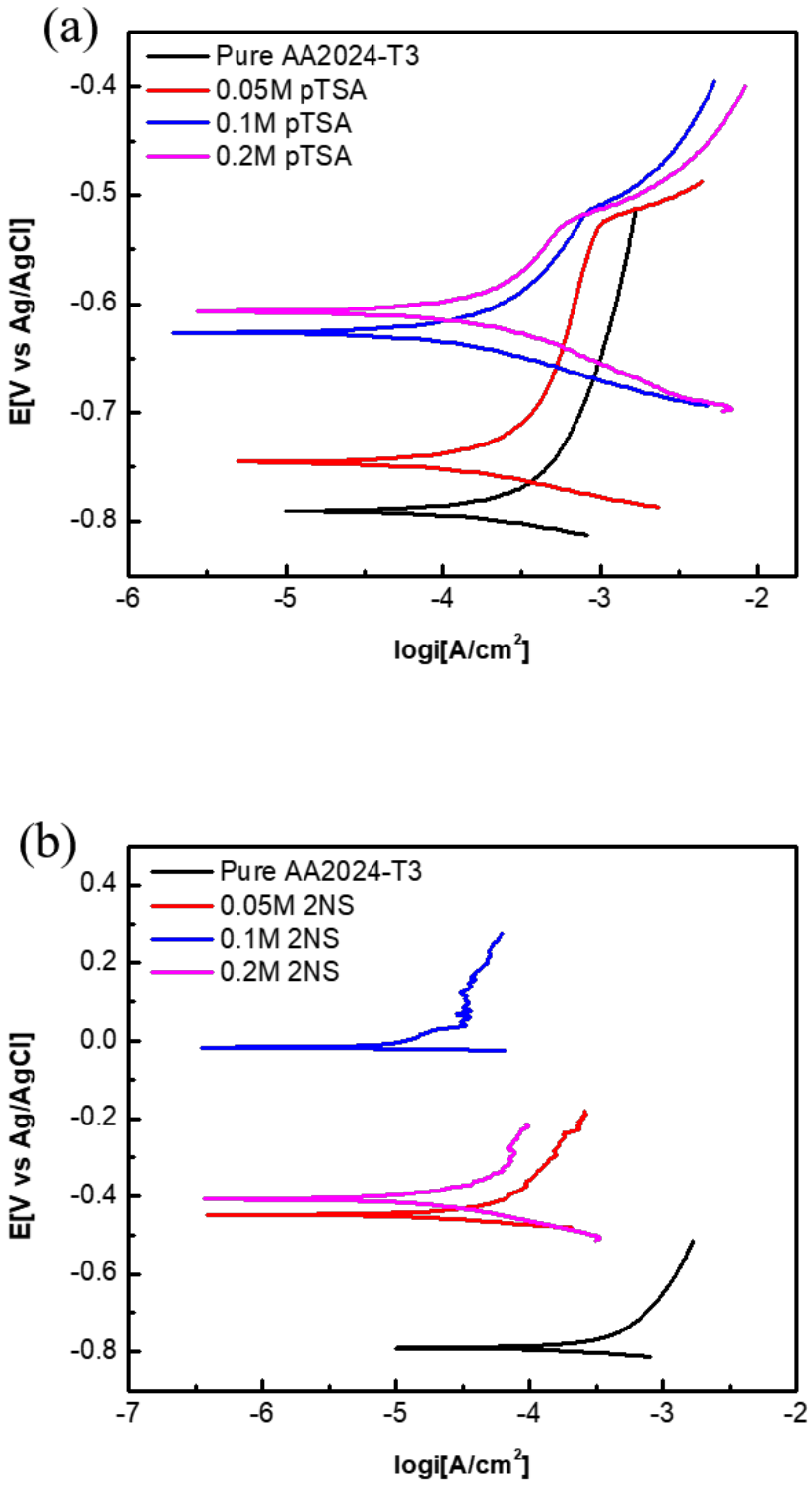

Figure 3.5. The Tafel plots with different dopants (a) pTSA and (b) 2NS

Table 3.1. The corrosion protection results of PPy coatings in the 3.5 wt% NaCl with pTSA and 2NS as dopants

	E_{corr} (mV)	I_{corr} ($\mu A \cdot cm^{-2}$)	C.R. (mm/yr)	P.E. (%)
Pure AA2024-T3	-790.51	145.28	0.791	-
0.05M pTSA	-745.31	97.39	0.531	32.96
0.1M pTSA	-626.43	89.25	0.486	38.57
0.2M pTSA	-606.88	85.57	0.466	41.10
0.05M 2NS	-447.92	14.51	0.076	90.01
0.1M 2NS	-15.86	5.53	0.030	96.19
0.2M 2NS	-406.63	13.17	0.072	90.93

3.3.4. The effect of electrodeposition time

The corrosion protection was further studied by extending the electrodepositing time from 15 minutes to 30 and 60 minutes. As discussed above, the optimized concentration for each dopant is 0.2M pTSA and 0.1M 2NS. The thickness of the coating can be estimated from following equation[144][145]:

$$d = \frac{QM}{2F\rho}$$

Where Q is overall charge for electrodeposition, M is the molar mass of the pyrrole (65 g/mol), ρ is the density (1.5 g/cm^3) and F is the Faraday constant (96,500 C/mole). From the equation above, the thickness depends on overall charge for electrodeposition which related to the coating time.

The thickness will increase with longer deposition time. **Fig 3.6.** presented the Tafel plot of 0.2M pTSA and 0.1M 2NS with different electrodeposition time.

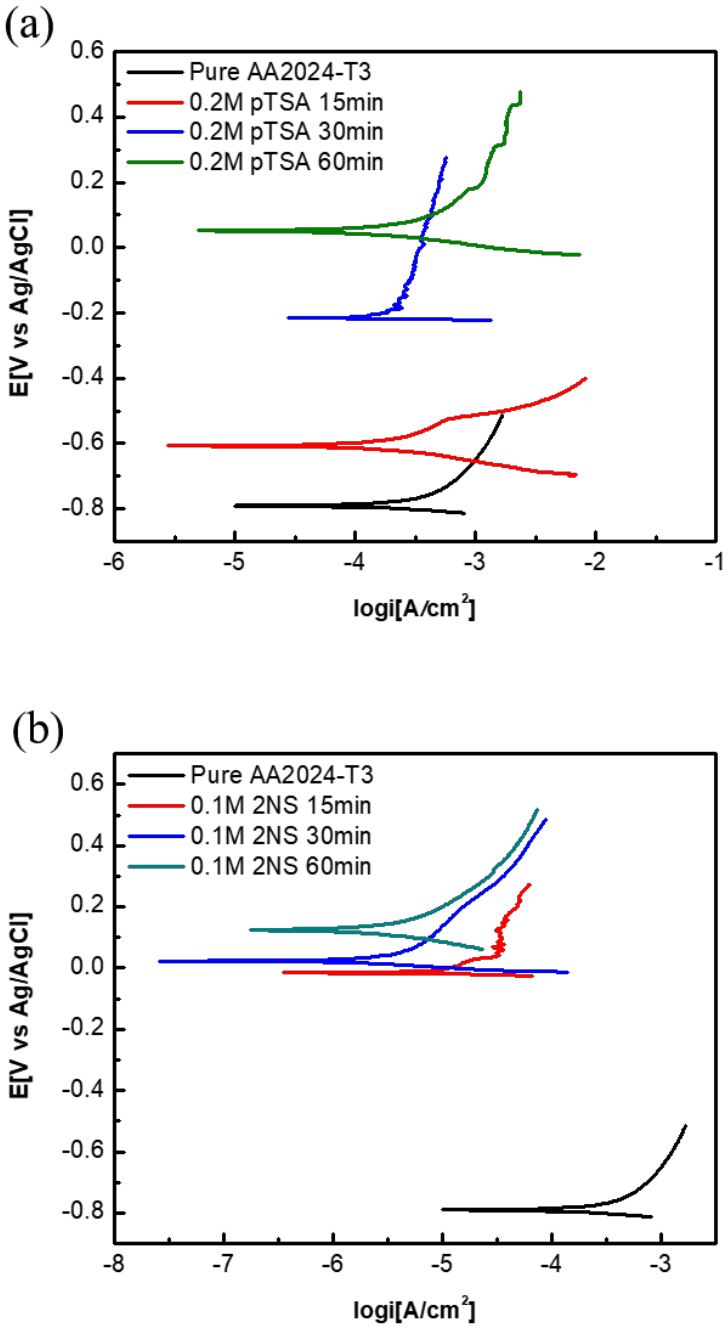

Figure 3.6. The Tafel plots with different dopants (a) pTSA and (b) 2NS under 15, 30, and 60 minutes of deposition time

In **table 3.2**, the Tafel parameters were listed to compare the effect of the thickness. Superior corrosion potentials were found while electrodepositing for 60 minutes for both dopants. The corrosion potentials increased 658.49 mV for 0.2M pTSA and 139.93 mV for 0.1M 2NS. However, for 0.2M pTSA, the corrosion current raised which affects the corrosion protection indicating the reduction of corrosion resistance. In contrast to pTSA, the corrosion current of 0.1M 2NS kept at a high and stable value where the protection efficiency achieved at 98.10%. The investigation carried out by different electrodeposition times has revealed that the effect of electrodeposition time promotes the corrosion potential but a minor degradation of corrosion current. Several coating options have been developed with varying degrees of protection efficiency. For example, Kumara et al achieved a protection efficiency of 99.58% with their polypyrrole-CeO2 coating[107], while Kartsonakis et al developed a hybrid organic-inorganic multilayer coating made of Polyaniline, polypyrrole, and CeO2 that exhibited a protection efficiency of 95.77%[146]. Additionally, Menkuer and Ozkazanc developed a PPy/ZrO2 coating with a protection efficiency of 99.7%[147]. Comparing the protection efficiency of the 0.1 M 2NS to published results can provide insights into its effectiveness. In comparison, the PPy/2NS coating developed in this study demonstrated a competitive protection efficiency of 98.10%.

Table 3.2. The corrosion protection results of PPy coatings in the 3.5 wt% NaCl with pTSA and 2NS as dopants under different coating time

		E_{corr} (mV)	I_{corr} ($\mu A \cdot cm^{-2}$)	C.R. (mm/yr)	P.E. (%)
Pure AA2024-T3		-790.51	145.28	0.791	-
0.2M pTSA	15 min	-606.88	85.57	0.466	41.10
	30 min	-216.47	104.07	0.567	28.36
	60 min	51.61	95.52	0.520	34.25
0.1M 2NS	15 min	-15.86	5.53	0.030	96.19
	30 min	22.88	1.14	0.006	99.22
	60 min	124.07	2.76	0.015	98.10

3.3.5. Topcoat with spray paint and its anti-corrosion performance

The conventional coating of corrosion protection includes (i) pretreatment (ii) primer coating and (iii) topcoat. The function of the primer is corrosion protection. The topcoat provides UV, abrasion, and mechanical resistance. A topcoat of spray paint was added on top of the PPy coating for 0.2M pTSA and 0.1M 2NS. **Fig 3.7.** and **table 3.3** exhibited the Tafel curves and the data after topcoat with spray paint. For the pure AA2024-T3 sample, the corrosion current had a significant decrease corresponding to the barrier effect of the spray paint. From **table 3.3**, only spray paint itself had the protection efficiency of 99.46% indicating the barrier effect of the spray paint prevent the diffusion of aggressive ions. The decrease of corrosion potential of uncoated AA2024-T3 can be attributed to the alloy surface being topcoat right after the polish process while the surface is still active. When comparing PPy-coated samples with pure AA2024-T3, 0.2M pTSA and 0.1M 2NS exhibited better corrosion protection which indicated a synergetic effect of the PPy layer and spray paint topcoat was obtained. For 0.2M pTSA, the corrosion efficiency reached 99.98% which is a 65.73% improvement. The corrosion current of 0.1M 2NS reached 10 times lower than the 0.2M pTSA with a protection efficiency of 99.99% which showed the best anti-corrosion performance. The result of the experiment indicates that the topcoat of spray paint positively affects the corrosion protection. Furthermore, the incorporation of PPy coating and topcoat gave an excellent corrosion protection efficiency.

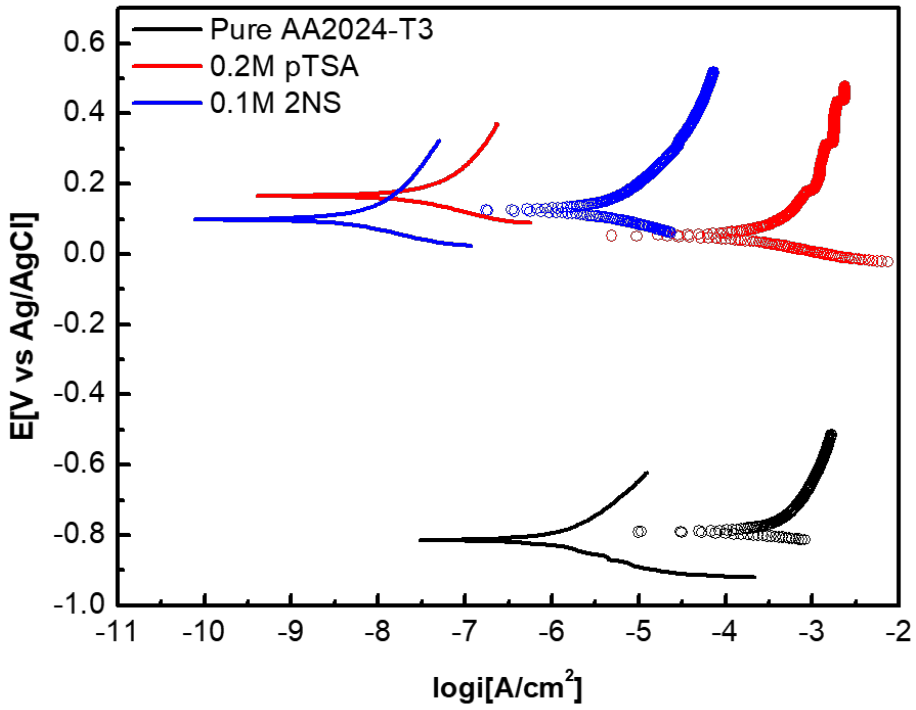

Figure 3.7. The result of Tafel plots with and without spray paint (- with topcoat; ○ without topcoat)

Table 3.3. Tafel corrosion protection results of PPy topcoat with spray paint in the 3.5 wt% NaCl with pTSA and 2NS as dopants

	E_{corr} (mV)	I_{corr} ($\mu A \cdot cm^{-2}$)	C.R. (mm/yr)	P.E. (%)
Pure AA2024-T3	-790.51	145.28	0.791	-
Pure AA2024-T3/Spray paint	-813.39	0.78	0.004	99.46
0.2M pTSA	51.61	95.52	0.520	34.25
0.2M pTSA/Spray paint	165.79	0.02	0.001	99.98
.1M 2NS	124.07	2.76	0.015	98.10
0.1M 2NS/Spray paint	98.63	0.003	0.0001	99.99

The corrosion behavior of pure AA2024-T3 and PPy-coated samples was investigated by EIS. **Fig. 3.8** and **Fig. 3.9** illustrated the EIS spectra of the AA2024-T3 coated by doped PPy with and without a topcoat of spray paint, respectively. The EIS curves were further analyzed using an equivalent circuit model shown in **Fig. 3.10**. The AA2024-T3 uncoated with PPy coating and/or topcoat is represented by **Fig. 3.10(a)** where R_s the solution resistance, CPE_{ct} the constant phase element of charge transfer capacitance, R_{ct} the charge transfer resistance, and Z_w the Warburg impedance. On the other hand, any coated samples were corresponding to **Fig. 3.10(b)** where CPE_f and R_f represented the constant phase element of coating capacitance and the coating resistance, respectively. For pure AA2024-T3, the Warburg impedance was introduced due to the 45° straight line after the semicircle indicating the diffusion behavior in the interface between electrolyte and alloy.

Table 3.4 listed the EIS fitting data from **Fig. 3.8** and **Fig. 3.9**. Firstly, although the resistance of coatings is small, the total resistance of PPy-coated samples without a topcoat is at least 3 magnitudes larger than pure AA2024-T3. The results suggested that the resistance of charge transfer was attributed to the PPy layer. After the topcoat process, the total resistance of pure AA2024-T3 was improved from 1.554×10^3 Ω to 2.915×10^7 Ω showing the barrier effect of the topcoat contributed to the total resistance. On the other hand, the total resistance of 0.2M pTSA and 0.1M 2NS did not change a lot. The barrier effect was shown in the resistance of the coating which improved 1.118×10^2 Ω and 9.407×10^2 Ω for 0.2M pTSA and 0.1M 2NS, respectively. From the EIS results, it is concluded that the charge transfer resistance corresponded to the PPy layer, and the coating resistance was influenced by the topcoat.

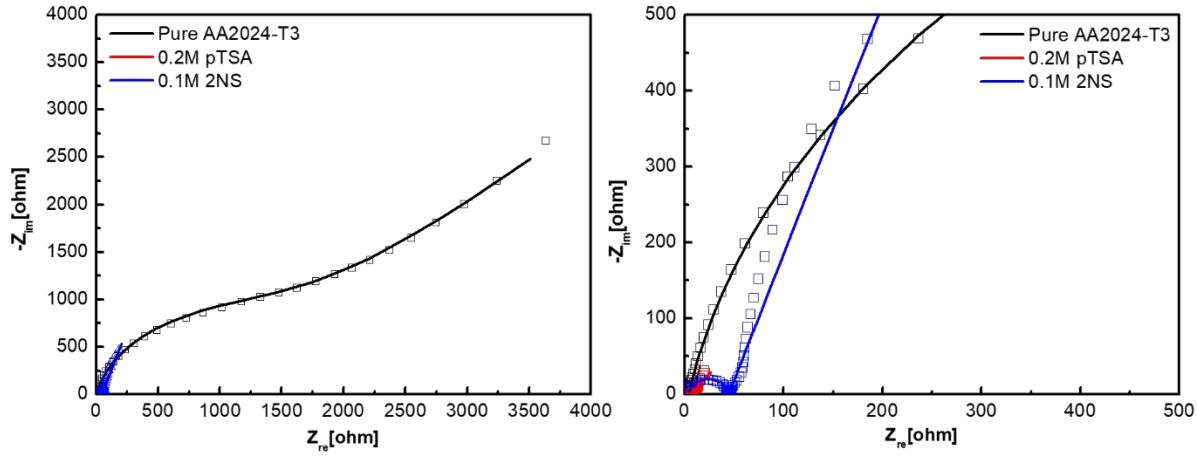

Figure 3.8. The result of EIS plots without topcoat (- fitting data; □ original data)

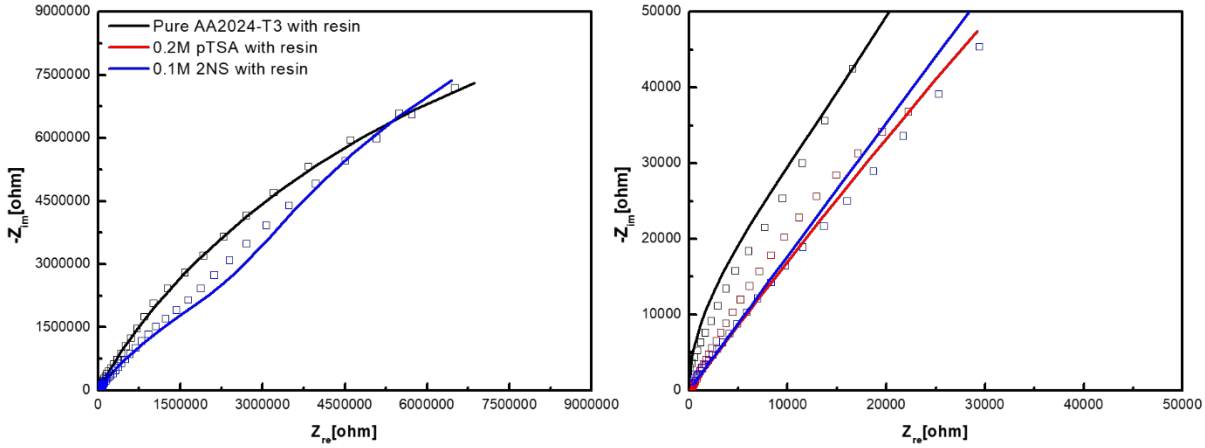

Figure 3.9. The result of EIS plots with topcoat (- fitting data; □ original data)

Table 3.4. EIS fitting data for Pure AA2024-T3, 0.2M pTSA, and 0.1M 2NS with and without topcoat of spray paint

	R_s (Ω)	CPE_f (F)	n	R_f (Ω)	Z_w ($Ω/s^{1/2}$)	CPE_{ct} (F)	n	R_{ct} (Ω)	R_{total} (Ω)
no topcoat									
Pure AA2024	4.382	32.37×10^{-6}	0.893	-	1887	-	-	1.554×10^{3}	1.554×10^{3}
0.2M pTSA	3.708	11.57×10^{-6}	1	2.369	-	1.520×10^{-1}	0.608	7.767×10^{6}	7.767×10^{6}
0.1M 2NS	3.744	19.40×10^{-8}	1	40.52	-	6.875×10^{-3}	0.798	1.274×10^{7}	1.274×10^{7}
topcoat									
Pure AA2024	0	7.316×10^{-9}	1	5.310×10^{4}	-	7.429×10^{-10}	0.698	2.910×10^{7}	2.915×10^{7}
0.2M pTSA	5.603	19.22×10^{-6}	0.593	1.142×10^{2}	-	9.383×10^{-7}	0.689	1.588×10^{6}	1.588×10^{6}
0.1M 2NS	0	1.362×10^{-7}	0.674	9.408×10^{6}	-	1.494×10^{-7}	1	2.449×10^{7}	3.389×10^{7}

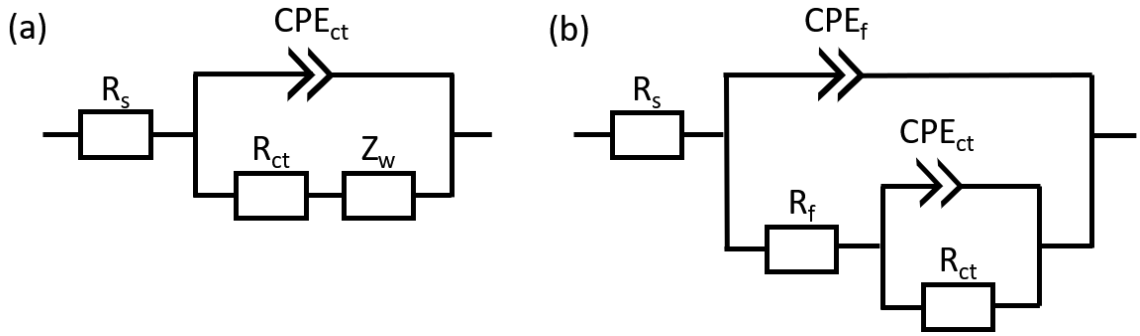

Figure 3.10. The equivalent circuit models for (a) Pure AA2023-T3 (b) samples with coating

The long-term durability test was performed by 48 hours of immersion in 3.5 wt% NaCl. **Fig. 3.11** illustrated the OCP vs time of all samples. Both 0.2M pTSA and 0.1M 2NS started with a positive OCP value accompanied by a decreasing trend of OCP indicating the degradation of the PPy layer due to anion exchange between PPy and the surrounding environment where the corrosion of AA2024-T3 occurred at the same time[148][149]. The pure AA2024-T3, with and without topcoat, showed a low potential of -550 mV. There is a clear advantage in combing PPy coating with topcoat which both 0.2M pTSA/spray paint and 0.1M 2NS/spray paint exhibited a stable and positive OCP value indicating the best anti-corrosion performance.

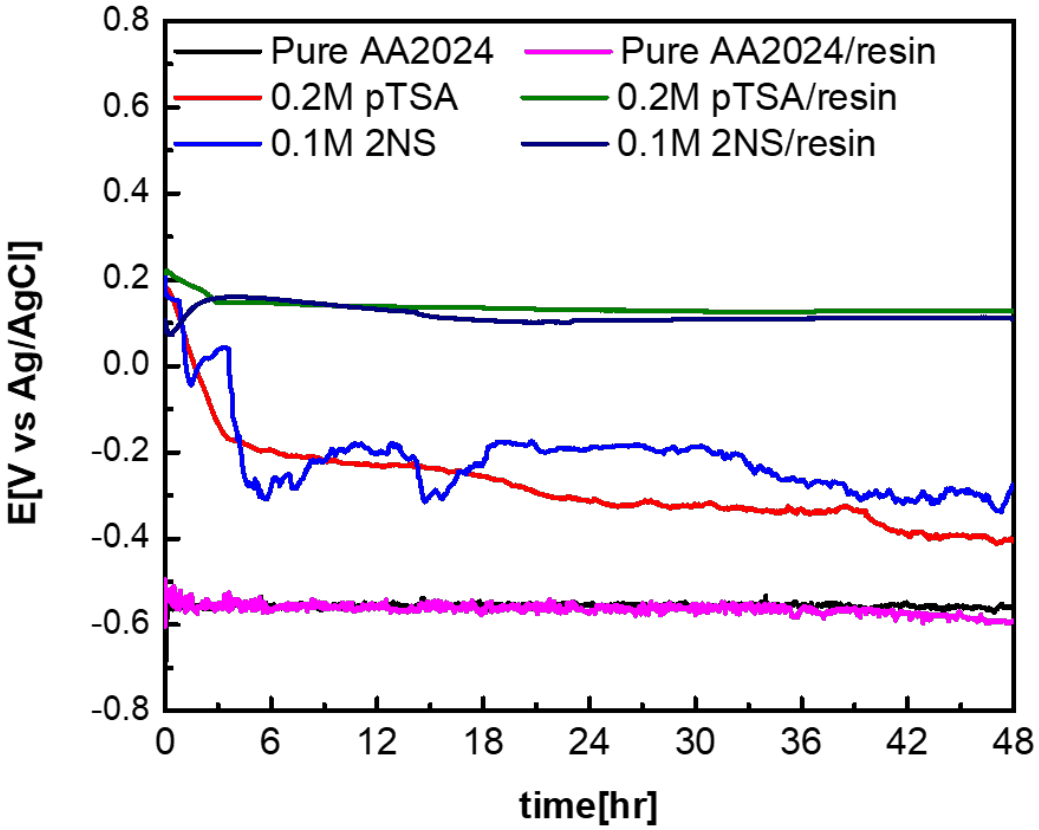

Figure 3.11. OCP vs time of all samples

3.4. Conclusions

Three dopants including sulfuric acid, p-toluenesulfonic acid, and 2-naphthalenesulfonic acid were introduced in the electrodeposition of polypyrrole on AA2024-T3. The FTIR and SEM confirmed the PPy film was successfully deposited on the alloy. By comparing with different concentrations, 0.2M pTSA and 0.1M 2NS performed a good anti-corrosion performance. 0.1M 2NS presented a better behavior with a corrosion potential of -15.86 mV and a corrosion current of 5.53 $\mu A \cdot cm^{-2}$ indicating the influence of chemical structure size. These two samples, 0.2M pTSA and 0.1M 2NS, were further optimized by increasing deposition time. It turned out that the corrosion potential was improved and further decreased the risk of corrosion by increasing the thickness of PPy layer. A practical application was studied by adding a topcoat on top of the PPy layer. The combined effect of the PPy layer and the topcoat generated an excellent outcome in which the protection efficiency of 0.2M pTSA/spray paint and 0.1M 2NS/spray paint are 99.98% and 99.99%, respectively. This significant improvement can be further interpreted by EIS result and OCP vs time. The EIS result proved different protection functions of the PPy layer and topcoat. The PPy coating acts as a primer and can provide corrosion protection while the topcoat of spray paint acts as a barrier to reduce the penetration of aggressive ions. The OCP vs time displayed a stable and positive OCP value allowing the AA2024-T3 to stay in a positive potential like a notable metal away from corrosion.

Chapter 4

Ultrasensitive electrochemical biosensors based on zinc sulfide/graphene hybrid for rapid detection of SARS-CoV-2

4.1. Introduction

Since the first case was confirmed from east Asia, the coronavirus disease 2019 (COVID-19) has been striking the world in the past two years[150][151][152][153][154]. People who got infected will have various symptoms including fever, cough, headache, loss of smell, loss of taste, fatigue, and breathing difficulties[155][156][157]. The major diagnostic methods to detect the disease include computed tomography (CT) scan, nucleic acid amplification test (NAAT), and serological techniques[158]. Today, NAAT using the quantitative reverse transcription polymerase chain reaction (qRT-PCR) is the most widely used method for detecting the COVID-19. However, the qRT-PCR is a time consuming and expensive test which also requires trained personnel. Therefore, the development of highly sensitive and quick detection methods is urgently needed. And the electrochemical DNA biosensors have received a lot of attraction for being a good detecting device[159][63][160][161].

Biosensor is an analytical device detecting biological or chemical reactions and then generating reliable data for several fields such as gene analyze[160][162], food safety[163][164], disease diagnosis[165], environmental monitoring[60], drug discovery[166], and water quality screening[62]. A typical biosensor consists of biological receptor, transducer, amplification, and signal processing. Based on different transducers, biosensors can be divided into electrochemical, optical, thermal, electronic, acoustic, and mass-based biosensor[167]. Among different transducers, the electrochemical biosensor is the most widely studied and applied biosensor due to the

advantages of low-cost, simplicity, portability, sensitivity, and rapid detection[162],[168]. It is critical to develop an appropriate composite for the signal amplification platform.

In practice, materials such as metals, metal oxides, graphene, conducting polymer, and their composite have been studied as signal amplifier for the electrochemical biosensors[169][170]. For instance, Saber et al. fabricated a gold electrode decorated by gold nanorods (GNRs) for detecting hepatitis B virus[171]. Due to the large surface area of the GNRs, the modified gold electrode can assemble more probe DNA and exhibit higher sensitivity with a detection limit of 2×10^{-12} M. Similarly, a hybrid nanocomposite containing copper oxide nanowires and carboxyl-functionalized single-walled carbon nanotubes was developed by Chen et al. for detecting the target DNA[172]. The performance of the modified electrode was benefited by the nanocomposite which provides a large surface area, fast electron transfer, and good electrical conductivity with the limit detection of 3.5×10^{-15} M. Graphene also shows a great potential in DNA detection due to its astonishing properties in electrical, optical, mechanical, and chemical aspects[173]. Pumera et al. reported a graphene-based electrode immobilized with hairpin-shaped probe DNA for detecting Alzheimer's disease[174]. The triple and quadruple layer graphene electrodes presented the best sensitivity with the detection limit of 6.6×10^{-12} M. All cases above show that the modified electrode provides a larger surface area and low charge transfer resistance for superior sensitivity compared to the raw electrode.

In the detection of COVID-19, the antibody testing, also known as serology testing, can check the antibodies to COVID-19 after a person has been infected or vaccinated. For instance, a paper-based biosensor modified by ZnO nanowires showed enhanced sensitivity for detecting antibody of COVID-19 with human serum samples[175]. In addition, Seo et al. reported a graphene-based biosensor functionalized with SARS-CoV-2 spike antibody as a receptor which demonstrated

highly sensing detection for the target SARS-CoV-2 antigen protein with a detection limit of 1×10^{-15} g/mL[176]. On the other hand, the molecular test detects the virus's genetic material to determine if a person has an active infection of COVID-19. Song et al. utilized polyaniline nanowires to modify the glassy carbon electrode for the detection of the COVID-19 N gene, resulting in a detection limit of 3.5×10^{-15} M[177]. This demonstrated that the electrochemical biosensor has the potential as a detection method for COVID-19. In many cases, the process of making the composite takes multiple steps with long preparation time and high cost. Therefore, developing a quick and one-step process is in need.

In this paper, we present a one-step and ultrafast microwave-initiated manufacturing process to prepare the electrical interface containing zinc sulfate and graphene (ZnS/graphene). Compared with the conventional heating method under thermodynamic equilibrium conditions, the microwave reaction method under non-equilibrium conditions can provide low-cost and time-saving process[70][178][179]. Most importantly, the ZnS/graphene DNA biosensor provides highly sensitivity. The graphene which accelerates the reaction rate by absorbing the electromagnetic energy acts as a heat resource during the microwave preparation. Different ratios of zinc precursors were investigated to obtain the optimized conditions and compared with commercial ZnS mixed with graphene without microwave reaction. The obtained ZnS/graphene sample was drop cast onto a glassy carbon electrode (GCE) surface for further electrochemical experiment. The probe DNA (pDNA) was successfully immobilized with GCE and then hybridized with different concentrations of target DNA (tDNA) to perform self-signal regeneration during the releasing process (**Scheme 1**). Three-electrode system was utilized while the ZnS/graphene modified electrode acted as the working electrode. The performance of the modified electrode was characterized by cyclic voltammetry (CV) and differential pulse voltammetry (DPV).

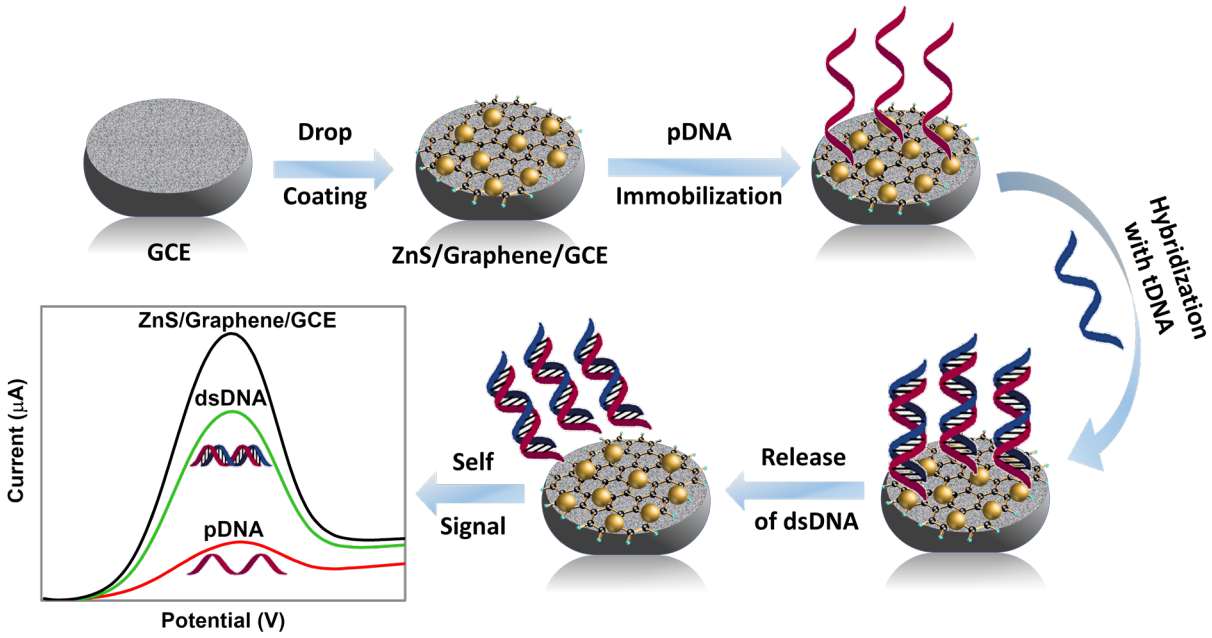

Scheme 1. Schematic illustration of detecting the SARS-CoV-2 by microwave-synthesized ZnS/graphene nanocomposite.

4.2. Methodology

4.2.1. Materials

Zinc acetate (GR, 99.5% purity) was obtained from BeanTown Chemical Inc. Graphene substrate was obtained from Magnolia Ridge Inc. Sulfur powder (GR, 99.5% purity) was provided by Alfa Aesar, America. The detection samples included artificial DNA probes, artificial DNA targets and SARS-CoV-2 standard were obtained from Eurofins Genomics LLC (Louisville, Kentucky).

4.2.2. Preparation of ZnS/graphene composites

For the preparation of ZnS/graphene nanocomposites, $ZnAc_2.2H_2O$, graphene, and sulfur powder were transferred into a 20 mL scintillation vial and mixed thoroughly to get a homogeneous mixture. The precursor ratios and synthesis parameters are described in **Table 4.1**. Subsequently,

the vial was placed inside microwave oven and irradiated with a high-power level (~1250 W) for 90 s. After the vial was cooled down to room temperature, the obtained powder was taken out. For comparison, the mixture of graphene and commercial ZnS nanoparticles were also prepared under the same microwave experimental conditions.

Table 4.1. Precursor mass ratios for different ZnS/graphene nanocomposites and their reaction parameters.

Samples	**$Zn(Ac)_2.2H_2O$ (mg)**	**Graphene (mg)**	**Sulfur (mg)**	**Microwave power (W)**	**Microwave time (s)**
ZnS/graphene-1	300	50	50	1250	90
ZnS/graphene-2	200	50	50		
ZnS/graphene-3	100	50	50		
ZnS/graphene-4	300	100	50		

4.2.3. Preparation of detection electrodes

The surface of glassy carbon electrode (GCE) was sequentially polished with 0.3- and 0.05-mm alumina slurries, then immersed in Piranha solution (conc. H_2SO_4: 30 % H_2O_2; 3: 1) for 30 min, followed by rinsing with DI water, and vacuum dried at 60 ºC. To prepare the coating paste, 100 mg of hybrid powder was suspended in 5 mL of isopropyl alcohol. Then, 0.1 mL of Nafion was added into the suspension following 20 min of sonication. Finally, 20 µL of the suspension was added to the prepared GCE surface and vacuum dried at 60 ºC.

4.2.4. Nanocomposite-based DNA biosensor probe and target sequences

The entire genetic sequence of SARS-CoV-2 was uploaded to the Global Initiative on Sharing All Influenza Data (GISAID) platform on January 10, 2020. The sequence data was used as reference for the design of oligos/probes needed for the development of SARS-CoV-2-specific testing. As

shown in **Table 4.2**, the probe and target DNA oligonucleotides were complementary to the specific target gene sequences and purchased from Eurofin Genomics.

Table 4.2. List of probe and target DNA sequences.

Gene (s)	**Synthetic base-pairs of DNA templates**	
S	Probe	GACATGTATAGCATGGAACC
	Target	GGTTCCATGCTATACATGTCTC
ORF 1b	Probe	CTTTAATGTTTTATTCTCTA
	Target	TAGAGAATAAAACATTAAAG
Mis-matched negative control	Probe	TTCACAAGTGCCGTGCCTAC
	Target	GGGTACTTAACAATGATTATT

4.2.5. Immobilization and hybridization of DNA

20 μL of probe-DNA solution (1.0×10^{-6} M pDNA) was added dropwise to the surface of modified GCE and dried at temperature below the melting T_m (temperature of melting) of corresponding probe sequences. After pDNA immobilization, following by rinsing with DI water, the GCE was dried again. Then, 20 μL of target DNA (tDNA) was added onto the pDNA-modified GCE surface and the corresponding electrode was dried at room temperature to form the hybrid double-stranded DNA (dsDNA). Subsequently, the electrode was kept at − 0.5 V for 300 s in 1.0 M KCl solution containing 0.2 M $K_3[Fe(CN)_6]$ to release the dsDNA into the electrolyte. After rinsing the surface of GCE with DI water, the electrode was ready for electrochemical tests.

4.2.6. Materials characterization

The surface morphology of the ZnS/graphene nanocomposite was characterized using scanning electron microscope (SEM) on JEOL JSM-7000F coupled with an energy dispersive X-ray

spectrometer (EDS, EDAX Instruments). The crystalline phase characteristics of the microwave samples was examined using the X-ray diffraction (XRD) (Philips X'pert MPD diffractometer) under Cu Kα radiation (λ=1.5405 Å) at 2θ range of 20-70°.

4.2.7. Electrochemical measurements

All the electrochemical tests were conducted in a mixture of 1.0 M KCl and 0.2 M $K_3[Fe(CN)_6]$ at room temperature. Cyclic voltammetry (CV) experiments were carried out at a scan rate of 100 mV s^{-1} from −0.4 to 0.8 V for different ZnS/graphene composites. The differential pulse voltammetry (DPV) tests were taken by using parameters as follows: pulse amplitude, 0.05 V; pulse width, 0.05 s; pulse period, 0.5 s. The peak current difference (ΔI_p) was calculated according to the relation of $\Delta I_p = I - I_0$. Where, I_0 represents the peak current for the modified electrodes immobilized with pDNA, and I represents the peak current for the resulting dsDNA after being released into the electrolyte. The calibration plot, ΔI_p vs. −log C was drawn by calculating the negative logarithmic values of target samples concentrations, where C is the concentration of target sample. Furthermore, the *LOD* (limit of detection) was measured using the following equation:

$$LOD = \frac{3 \times Standard\ deviation\ of\ blank\ solution, \sigma}{Slope\ of\ the\ callibration\ plot}$$

The standard deviation of blank solution was measured by running the DPV tests on pDNA-modified GCE for 10 times.

4.3. Results and discussion

4.3.1. Optimizing the precursor ratio

The electrochemical properties of different modified electrodes with different mass of precursors were investigated by CV technique. Among the four different mass ratios (see **Table 4.1**), as displayed in **Fig. 4.1a**, ZnS/graphene-1 has the prominent redox peaks with the anodic peak to cathodic peak separation of potential, ΔE_p ($\Delta E_p = E_{anodic\ peak} - E_{cathodic\ peak}$) of 130 mV. For the samples of ZnS/graphene-2 and ZnS/graphene-3, the redox peaks are not prominent, may be due to the incomplete reaction taking place during the microwave-assisted synthesis with the less amount of Zn-precursor. In addition, although ZnS/graphene-4 provides much higher current due to the presence of high amount of conductive graphene, the ΔE_p is as much as 330 mV, which indicates a sluggish kinetic transfer process of electrons.

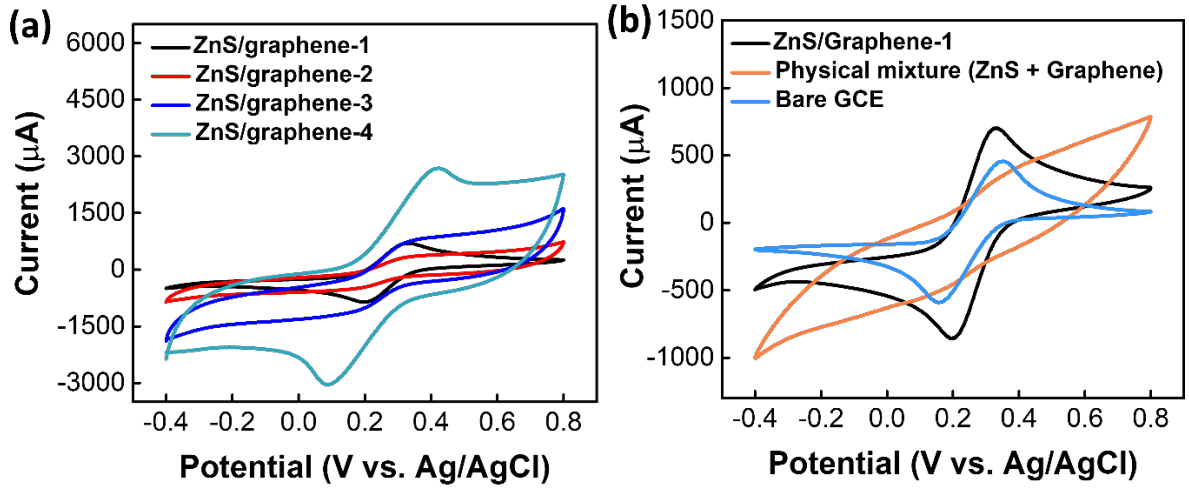

Figure 4.1. (a) CVs of different electrodes in a solution containing 1.0 M KCl and 0.2 M $K_3[Fe(CN)_6]$ as a redox probe at scan rate of 100 mVs^{-1}. $Zn(Ac)_2{\cdot}2H_2O$, graphene, and S

precursors have a mass ratio of 6:1:1, 4:1:1, 2:1:1, and 6:2:1, respectively. (b) CV curves of different electrodes in a solution containing 1.0 M KCl and 0.2 M $K_3[Fe(CN)_6]$.

Moreover, the electrochemical property of ZnS/graphene-1 was compared with a physical mixture of ZnS and graphene with a mass ratio of 6:1, and with the bare GCE. From **Fig. 4.1b**, it can be clearly observed that the physical mixture does not show prominent redox peaks. For ZnS/graphene-1 and bare GCE, ΔE_p values are 130 mV and 190 mV, respectively. Moreover, the ZnS/graphene-1 yields the maximum peak current, possibly because of the accelerated $[Fe(CN)_6]^{3-}$ diffusion towards the surface by a layer of graphene. Apparently, the ZnS/graphene-1 sample exhibited much higher electrochemical activity, and faster electron-transfer kinetics (reflected in the lower peak to peak separation) compared to all other modified electrodes including bare GCE. Therefore, for further studies, the detection of DNA samples was carried out on the surface of ZnS/graphene-1 modified GCE which was denoted as ZnS/G/GCE thereafter.

4.3.2. Characterization of the modified electrode

The morphology and distribution of the ZnS/graphene composite was shown in **Fig. 4.2a-e**. The SEM image was utilized to characterize the prepared ZnS/graphene composite (**Fig. 4.2a**). It can clearly be seen that the graphene substrate was fully decorated by ZnS. The EDS spectrum of ZnS/graphene exhibited the existence of the Zn and S elements. **Fig. 4.2b-e** illustrated the EDS elemental mapping of ZnS/graphene composite which clearly showed the evenly dispersed elements of Zn and S on the graphene surface. In addition, the C, Zn, and S components were closely stacked, indicating the formation of the hybrid composite. The XRD diffractogram of ZnS/graphene was shown in **Fig. 4.2f**. The strong peaks appeared at 2θ around 26.68°, 28.56°, 30.86°, and 51.1° are assigned to (100), (002), (101), and (103) reflections of hexagonal wurtzite

ZnS (JCPDS 36-1450), respectively. The overall XPS spectrum for the ZnS/graphene composite was shown in **Fig. 4.2g**. The spectrum showed the presence of C 1s, O 1s, Zn 2p, and S 2p peaks. The characterized results confirmed the successful synthesis of ZnS/graphene composite. Since microwave-initiated synthesis does not have any inert gas protection during the heating process, the EDS spectrum showed the presence of ZnO. However, the ZnO does not contribute much to DNA detection.

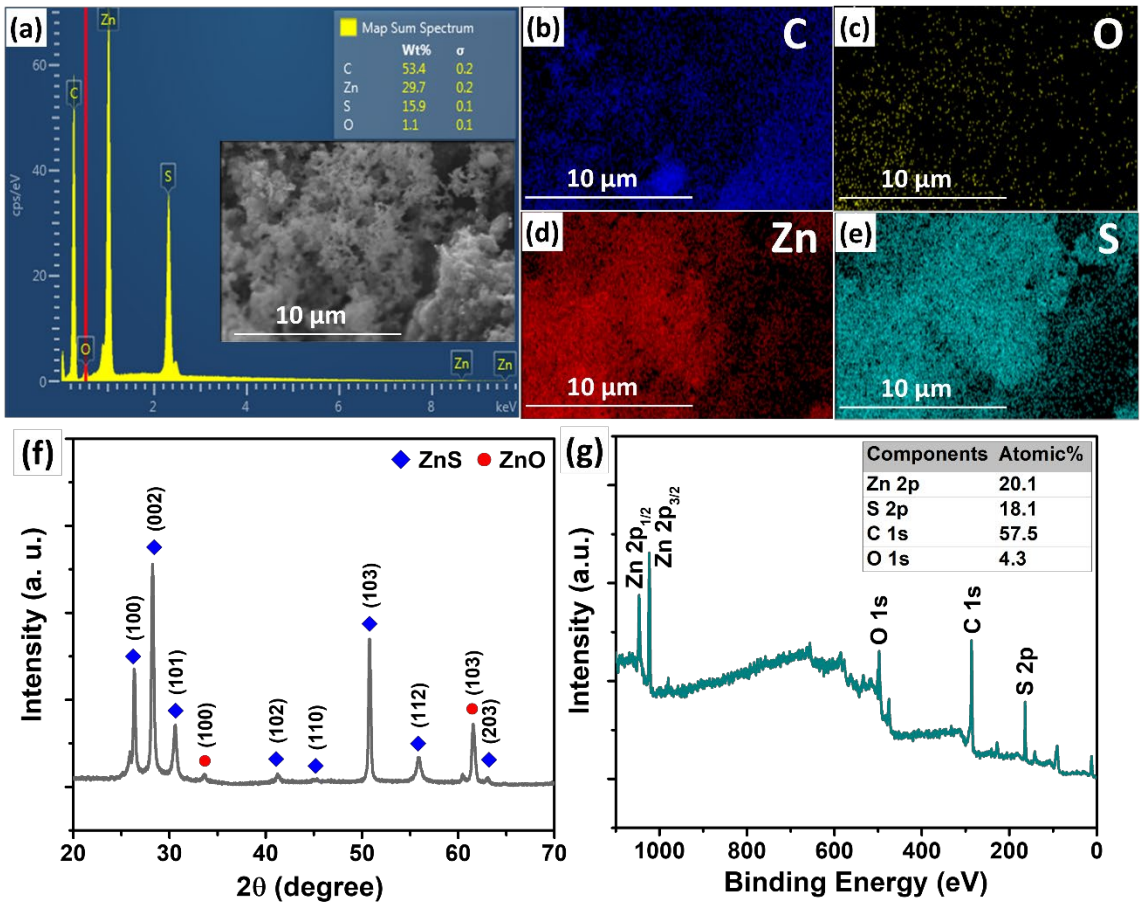

Figure 4.2. (a) SEM image and EDS spectrum; (b)-(e) the EDS elemental mapping; (f) XRD pattern and (g) XPS spectrum of ZnS/graphene composite.

The CV and DPV comparison between ZnO and ZnS have been discussed and shown in **Fig. 4.3**. Since the microwave heating process was operated without gas protection. It is common to get oxide compounds. In **Fig. 4.3 (a)**, ZnO/graphene does not show prominent redox peaks when compare with ZnS/graphene. In addition, the current peak for ZnO/graphene is small at the value of 142 µA in **Fig. 4.3 (b)**. Therefore, the ZnO does not contribute to the DNA detection.

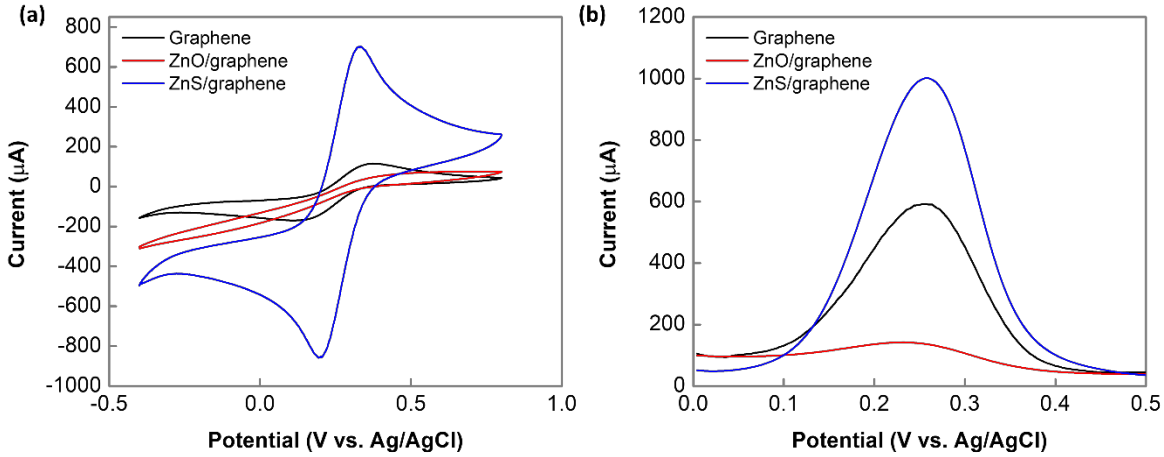

Figure 4.3. (a) CV plot and (b) DPV plot of different electrodes in a solution containing 1.0 M KCl and 0.2 M $K_3[Fe(CN)_6]$ as a redox probe at scan rate of 100 mVs^{-1}

4.3.3. Detection of synthetic target DNA samples

To explore the analytical characteristics of the optimized ZnS/G/GCE for the detection of synthetic gene DNA sequences, DPVs were performed in an electrolyte solution of 1.0 M KCl containing 0.2 M $K_3[Fe(CN)_6]$. Initially, the sensor electrode of ZnS/G/GCE was attached with the 1.0×10^{-6} M probe DNA (pDNA) and treated for different concentrations of target DNA (tDNA) solutions as depicted in **Fig. 4.4a**. After immobilizing the pDNA on the surface of ZnS/G/GCE, the oxidation or anodic peak current (I_{pa}) decreases significantly because the nonconductive pDNA blocks the

effective electron transfer through the coating surface. However, when the pDNA was hybridized with the tDNA, the peak currents were enhanced linearly with the enhancing concentrations of tDNA from 1.0×10^{-18} M to 1.0×10^{-7} M. The release of the resulted dsDNA from the ZnS/graphene/GCE surface occurs because of hybridization with complementary targets, accompanied with the self-signal regeneration of the ZnS/graphene/GCE. With an increase in tDNA concentration, more of the pDNA can get hybridized, and then release into the electrolyte. Therefore, the electron transfers as well as the peak currents increase. Furthermore, the regression calibration plot was drawn from ΔI_p vs. −log C with the correlation coefficient estimated as R^2 = 0.96 as shown in **Fig. 4.4b**. Thus, the limit of detection (LOD = 3σ/slope) was determined, which was found to be 4.453×10^{-20} M.

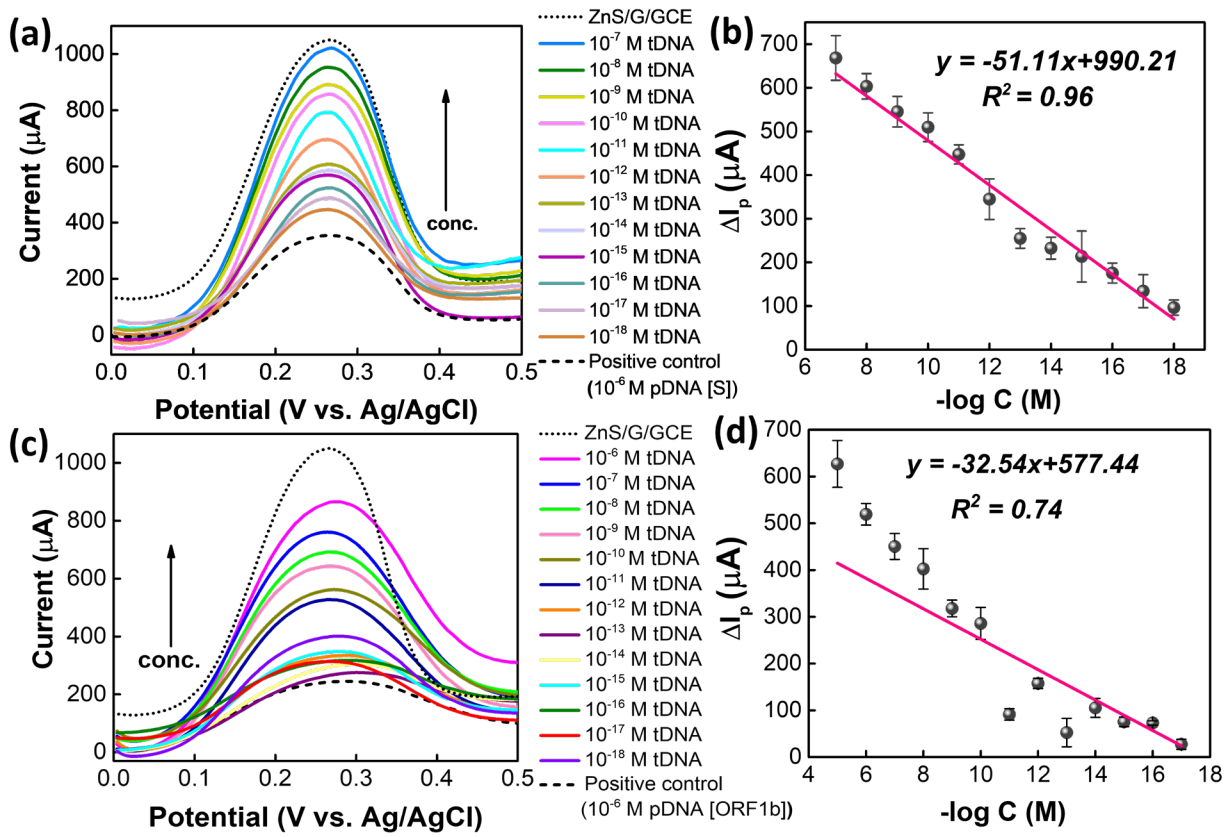

Figure 4.4. (a) DPV plots and (b) the regression calibration plots. [Note: probe and target DNA samples are for S-gene]. (c) DPV plots and (d) the regression calibration plots. [Note: probe and complementary DNA samples are for ORF 1b-gene].

In addition, the DPV tests were performed for the ORF 1b-gene. As displayed in **Fig. 4.4c**, the results follow a similar trend like S-gene. However, at the lower concentrations of cDNA samples from 10^{-12} M to 10^{-18} M, results showed arbitrary currents, and therefore the regression coefficient is only 0.74 (**Fig. 4.4d**). Based on these findings, the LOD was measured to be 2.013×10^{-18} M.

Following the same steps and procedures, DPV tests were also performed for mis-matched negative control sample, as displayed in **Fig. 4.5a**. Since there is only a few of matched sequences present in these samples (**Fig. 4.5b**), the tDNA cannot hybridize successfully with the pDNA. Therefore, although after hybridization the currents get increased from the pDNA-modified electrode, there is no particular trend found for these samples. The matched sequence of S and ORF-1b genes are shown in **Fig 4.6**.

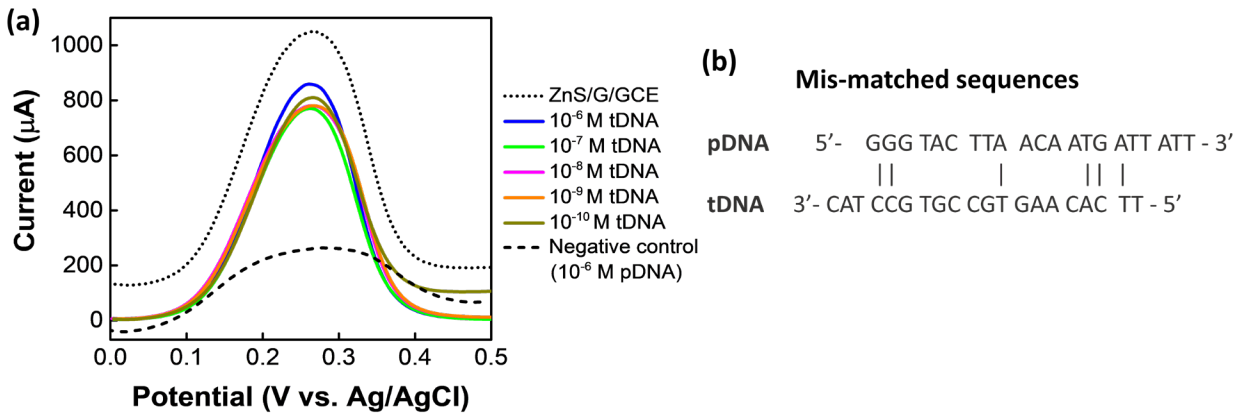

Figure 4.5. (a) DPV plots of synthetic samples. (b) Mis-matched sequences of pDNA and tDNA. [Note: probe and target DNA samples are negative control]

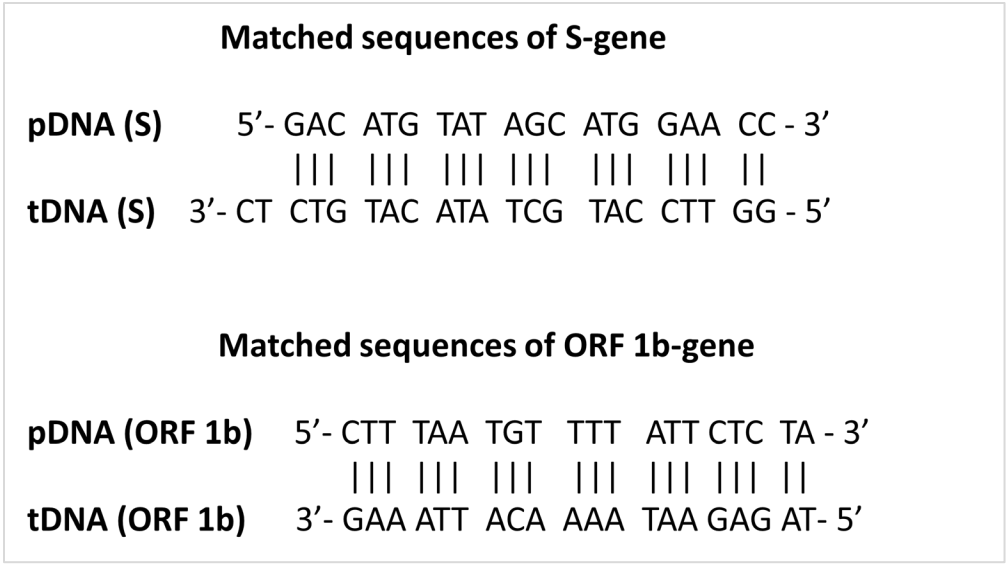

Figure 4.6. Mis-matched sequences of pDNA and tDNA of S and ORF 1b genes.

4.3.4. Detection of SARS-CoV-2 standard samples

Following the similar DPV characterization technique, the detection of SARS-CoV-2 standard samples was performed. The positive control from TaqPath™ COVID-19 Fast PCR Combo Kit 2.0 was diluted to a working stock of 20 copies/µL on ice, (ThermoFisher). This Fast PCR kit Positive Control consists of several different gene templates (200,000 copies/1 mL), such as S, N, ORF1ab etc., which is widely used by CDC CLIA certified laboratories. Any of the probe templates targeting these genes can be used to perform the validation of the detection tests, therefore, we tested the S and ORF1b probes used in **Fig. 4.2**. As shown in **Fig. 4.7a**, S-probe can detect from 20 copies up to 1 copy. The corresponding concentrations of different number of copies are displayed in supporting information, **Table 4.3**. From these results, one thing is noticeable that the low concentrations at the range of 10^{-18} M to 10^{-20} M can be detected. Despite of the presence of all different genes in a standard solution, only a single probe template was used to detect the hybridized dsDNA. Hence, there is a huge chance of some target templates remain immobilized

on the surface of ZnS/graphene/GCE even after rinsing with DI water, which eventually may hinder the electron transfer process resulting arbitrary change in peak currents. Similar to the results for synthetic base-pair DNA samples, the detection of SARS-CoV-2 standard sample also provides the similar trend of increase in peak currents by increasing the concentration of target samples. Moreover, the regression calibration plot (**Fig. 4.7b**) was drawn and LOD values were calculated to be 2.068×10^{-20} M ($R^2 = 0.98$) for S-probes. These results clearly indicate a good performance from S-probe to detect the SARS-CoV-2 standard solutions.

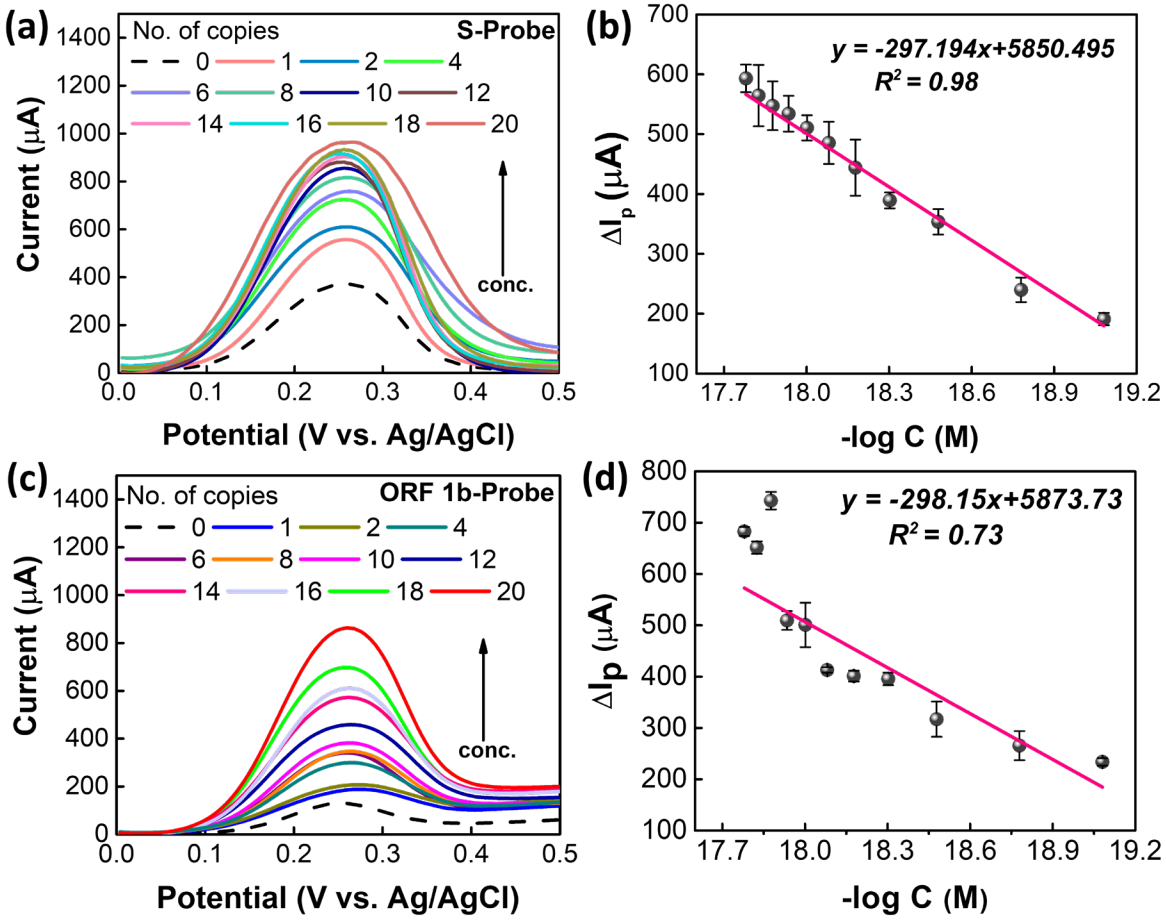

Figure 4.7. (a, b) DPV and calibration plots for the detection of SARS-CoV-2 standard using S-probe. (c, d) DPV and calibration plots for the detection of SARS-CoV-2 standard solutions using ORF 1b-probe in a solution containing 1.0 M KCl and 0.2 M $K_3[Fe(CN)_6]$.

Table 4.3. The corresponding concentrations of different number of copies for SARS-CoV-2 standard solution.

No. of Copies	Concentration (M)
1	8.30289×10^{-20}
2	1.66058×10^{-19}
4	3.32116×10^{-19}
6	4.98173×10^{-19}
8	6.64231×10^{-19}
10	8.30289×10^{-19}
12	9.96347×10^{-19}
14	1.16240×10^{-18}
16	1.32846×10^{-18}
18	1.49452×10^{-18}
20	1.66058×10^{-18}

Moreover, the SARS-CoV-2 standard solutions were also detected using the ORF 1b-probes. For ORF 1b-probe (**Fig. 4.7c**, **4.7d**), the results followed the trend from 1 to 20 copies, which has superior sensitivity as RT-PCR detection method using the TaqPath™ COVID-19 Combo Kit. Additionally, the performance of the DNA biosensor for the detection of SARS-CoV-2 was compared with previously published studies. According to **Table 4.4**, the proposed ZnS/graphene modified GCE achieved a lower detection limit which has 5 orders of magnitude less than the other reports.

Table 4.4. Comparison of the designed biosensors for the detection of SARS-CoV-2

Platform	Detection Method	LOD	Reference
Pt/Ti/Glass Wafer	Impedance	1×10^{-8} M	[180]
Co-TNTs	Amperometry	7×10^{-10} M	[181]
Graphene	SWV	2.6×10^{-7} M	[182]
Au IDE	EIS	3.9×10^{-16} M	[183]
CSPE/CNF-AuNP	EIS	7×10^{-13} M	[184]
rGO-Au	EIS	13×10^{-15} M	[185]
PANI/GCE	DPV	3.5×10^{-15} M	[177]
MIP/Au-TFE	DPV	15×10^{-15} M	[186]
AuNPs/FTO	DPV	10×10^{-15} M	[187]
ZnS/graphene/GCE	DPV	2.1×10^{-20} M	This work

Co-TNTs: cobalt functionalized TiO_2 nanotubes; IDE: interdigitated electrode; CSPE: carbon-based screen-printed electrode; CNF: carbon nanofibers; MIP: molecular imprinted polymer; TFE: thin film electrode; FTO: fluorine doped tin oxide electrode

4.3.5. Investigating the detection of synthetic DNA samples by one-step hybridization

Besides investigating the detection of DNA samples following the multiple-step procedure, the one-step hybridization technique was also applied in this study. The major steps are displayed in **Fig. 4.8a**, where instead of drop coating the DNA samples onto the surface of ZnS/graphene-modified GCE, the probe and target DNA samples were directly mixed into the electrolyte solution. Subsequently, the DPV tests were performed using the ZnS/graphene/GCE as the working electrode. From the results displayed in **Fig. 4.8b**, at high concentration range from 1×10^{-6} M to 1×10^{-10} M of cDNA, the results showed the similar trend as before. However, the samples with low concentrations from 1×10^{-11} M to 1×10^{-15} M, the results are inconsistent. These results can be improved by handling the samples more carefully. Moreover, this one-step hybridization can save a lot of sample-preparation time comparing to the multiple-step procedure.

Further optimizations are still required to establish a stable detection method using one-step hybridization.

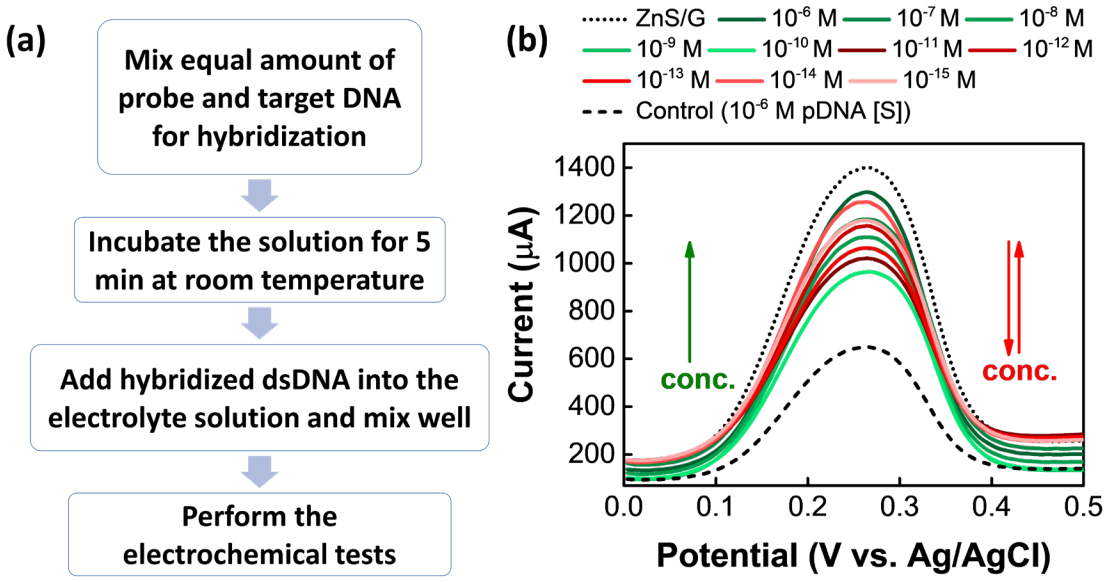

Figure 4.8. (a) Detection steps of synthetic DNA samples *via* one-step hybridization method. (b) DPV plots to detect S-gene by one-step method. [Note: probe and complementary DNA samples are for S-gene].

4.4. Conclusions

In conclusion, we report the construction of novel electrochemical sensing nanohybrid of ZnS/graphene for detecting SARS-CoV-2 nucleic acids by a one-pot and ultrafast microwave-controlled synthesis approach. The ZnS/graphene modified GCE exhibited promising electrochemical property and faster electron transfer kinetic which improved the detection performance. When the pDNA was immobilized on the surface of ZnS/graphene/GCE, the peak current decreased due to the obstruction of electron transfer process. Hybridization between the

probe and target DNA caused the regeneration of the self-signal of ZnS/graphene. The peak current showed linear trend with decreasing the concentration of target DNA. Among different pDNA sequences, S-gene provides a better detection result when hybridized with target DNA or standard SARS-CoV-2 controls where the limit of detection are 4.453×10^{-20} M and 2.068×10^{-20} M, respectively. In addition, we presented a one-step hybridization to save the multiple-step procedure. A similar result was obtained only at high concentrations from 1×10^{-6} M to 1×10^{-10} M. The investigation of the one-step hybridization could be further studied. Overall, the microwave-synthesized composite of ZnS/graphene coating on the GCE electrode showed superior sensitivity and low-concentration detection limit. Our strategy and assays developed here could be useful for rapid virus infection screening, public health surveillance and in the settings with limited laboratory resources and utilized by users with limited training. Our platform will enable robust, low-cost, multiplex, and quantitative DNA/RNA analysis tools for field-deployable detection devices.

Chapter 5

Summary and outlook

The main goal of this dissertation is to study how surface modification affects the electrochemical performance of the substrate and explore its potential use in corrosion protection and biosensor technology. Firstly, in the corrosion protection, we have shown and examined the effectiveness of a conducting polymer that can serve as anti-corrosion material with one layer of coating. The type of dopants employed during electrosynthesis has a significant impact on the electrochemical performance of conducting polymers. Incorporating dual dopants into the PPy coating produces a synergistic effect, improving both its anti-corrosion performance and adhesion property. On the other hand, to further examine the distinct protection mechanisms of the topcoat and primer (PPy layer), a conventional coating method was employed using spray paint as a topcoat. In the last project, an electrochemical biosensor based on a ZnS/graphene nanocomposite with exceptional sensitivity is described, which enables rapid and direct detection of SARS-CoV-2 nucleic acids. Using an ultrafast (90 sec) microwave-based non-equilibrium heating approach, we exhibited a simple one-step process for the production of ZnS/graphene. The experimental findings indicated that the proposed biosensor could detect all different SARS-CoV-2 samples, even at low concentrations. The following sections will provide separate summaries of the main findings and future work for each project.

The first project involved analyzing the ability of a PPy coating to protect copper (Cu) surfaces from corrosion through electrochemical techniques. To optimize the electrochemical deposition of the PPy coating onto the copper surface, we investigated the passivation ability of oxalic acid and sodium salicylate. Both dopants (oxalic acid and sodium salicylate) were capable of creating non-

reactive layers on the copper surface before PPy deposition. The effectiveness of the PPy coating in preventing corrosion was then assessed using Tafel plot and electrochemical impedance spectroscopy, with the sodium salicylate-doped PPy coating providing a higher corrosion protection efficiency of 90% compared to the oxalic acid system. After adding tannic acid as an adhesion promoter during the electrodepositing process, the adhesion performance was enhanced from 0B to 3B with 85% of the coating remaining on the substrate after peeling the testing tape. Surprisingly, the corrosion protection efficiency for the oxalic acid system is increased to 94%. The type of dopants utilized during electrosynthesis has a significant impact on the physical and electrochemical performance of conducting polymers. Additionally, the size of the dopants prevent the aggressive chloride ions from penetrating the coating. Lamellar structures are created when aromatic ring forms π-π stacking within the molecule along the polymer chain to stop chloride ions from entering the coating system.

In the second project, the process of depositing PPy onto AA2024-T3 through electrodeposition involved the use of three different dopants - sulfuric acid (SA), p-toluenesulfonic acid (pTSA), and 2-naphthalenesulfonic acid (2NS) - by applying a constant potential. Utilizing pTSA and 2NS dopants, the process of electrodeposition of PPy onto AA2024-T3 was accomplished, resulting in superior corrosion protection in comparison to untreated AA2024-T3. The findings indicated that 2NS-doped PPy exhibited superior behavior with a corrosion potential of -15.86 mV and a corrosion current of 5.53 $\mu A \cdot cm^{-2}$. Additionally, the practical application of a topcoat layer on top of the PPy layer was investigated. The synergistic effect of the PPy layer and the topcoat layer produced remarkable results, with the pTSA-doped PPy/spray paint and 2NS-doped PPy/spray paint exhibiting protection efficiencies of 99.98% and 99.99%, respectively. According to the EIS

result, the PPy coating functioned as a primer, offering corrosion protection, whereas the spray paint topcoat functioned as a barrier, decreasing the infiltration of aggressive ions.

For the future work of this project, the condition during the electrodeposition can be further investigated especially the applied potential. The applied potential in the current projects was 1 V whereas the oxidation potential of pyrrole is 0.8 V[119]. Additionally, the anti-corrosion performance of the PPy layer could be further enhanced by incorporating metal/metal oxide nanoparticles, including Ag[188], TiO_2[189], ZnO[190], ZrO_2[191], and SiO_2[111]. An optimized electrodeposition method is employed for the electrochemical synthesis of PPy/metal or PPy/metal oxide composite coatings on copper or AA2024 from an aqueous solution containing pyrrole and dopant. It is worth noting that experimental variables such as dopant, solvent, and applied potential have a strong influence on morphology.

In the third project, our biosensor project introduces a one-pot and rapid microwave-controlled synthesis approach for creating novel electrochemical sensing ZnS/graphene nanohybrids that can detect SARS-CoV-2 nucleic acids. The GCE modified with ZnS/graphene showed remarkable electrochemical characteristics and faster electron transfer kinetics, which enhanced the detection performance. The microwave-assisted composite ZnS/graphene coating on the GCE electrode demonstrated better sensitivity and low-concentration detection limit of 2.068×10^{-20} M. To progress this study in the future, comprehending the mechanisms underlying the electrochemical activities of ZnS/graphene nanocomposite is crucial. The same detection technique could be utilized in studies to identify diverse bioreceptors, such as enzymes, antibodies, cells, aptamers, and nanoparticles. Also, this straightforward microwave-irradiation method can be utilized to produce a range of nanostructures, such as ZnSe and ZnTe, by modifying the reaction precursors, experimental conditions, and microwave parameters. To summarize, the findings of this

dissertation will contribute to advancing the understanding of material interfaces and will serve as a basis for further exploration of both fundamental and applied sciences and technologies.

References

[1] P.M. Martin, Introduction to Surface Engineering and Functionally Engineered Materials, 2011. https://doi.org/10.1002/9781118171899.

[2] S. Engineering, W. Resistance, Introduction to Surface Engineering for Corrosion and Wear Resistance, in: Surface Engineering for Corrosion and Wear Resistance, ASM International, 2001: pp. 1–10. https://doi.org/10.31399/asm.tb.secwr.t68350001.

[3] G. Koch, J. Varney, N. Thopson, O. Moghissi, M. Gould, J. Payer, International Measures of Prevention , Application , and Economics of Corrosion Technologies Study, NACE International. (2016) 1–216.

[4] Y. Sahan, S. Sudarsono, E. Silviana, Chairul, Wisrayetti, Performance of the electrical generator cell by the ferrous alloys of printed circuit board scrap and Iron Metal 1020, IOP Conference Series: Materials Science and Engineering. 345 (2018) 012038. https://doi.org/10.1088/1757-899X/345/1/012038.

[5] P. Pedeferri, Cathodic protection and cathodic prevention, Construction and Building Materials. 10 (1996) 391–402. https://doi.org/10.1016/0950-0618(95)00017-8.

[6] J.D. SUDBURY, O.L. RIGGS, D.A. SHOCK, Anodic Passivation Studies, Corrosion. 16 (1960) 47t–54t. https://doi.org/10.5006/0010-9312-16.2.91.

[7] D. Chadwick, T. Hashemi, Adsorbed corrosion inhibitors studied by electron spectroscopy: Benzotriazole on copper and copper alloys, Corrosion Science. 18 (1978) 39–51. https://doi.org/10.1016/S0010-938X(78)80074-2.

[8] G.H. Meier, A review of advances in high-temperature corrosion, Materials Science and Engineering A. 120–121 (1989) 1–11. https://doi.org/10.1016/0921-5093(89)90712-0.

[9] A. Popova, Temperature effect on mild steel corrosion in acid media in presence of azoles, Corrosion Science. 49 (2007) 2144–2158. https://doi.org/10.1016/j.corsci.2006.10.020.

[10] M.C. Zhao, M. Liu, G.L. Song, A. Atrens, Influence of pH and chloride ion concentration on the corrosion of Mg alloy ZE41, Corrosion Science. 50 (2008) 3168–3178. https://doi.org/10.1016/j.corsci.2008.08.023.

[11] H. Otmacic Curkovic, E. Stupnisek-Lisac, H. Takenouti, The influence of pH value on the efficiency of imidazole based corrosion inhibitors of copper, Corrosion Science. 52 (2010) 398–405. https://doi.org/10.1016/j.corsci.2009.09.026.

[12] Z.B. Zheng, Y.G. Zheng, Erosion-enhanced corrosion of stainless steel and carbon steel measured electrochemically under liquid and slurry impingement, Corrosion Science. 102 (2016) 259–268. https://doi.org/10.1016/j.corsci.2015.10.014.

[13] S. Jiang, F. Chai, H. Su, C. Yang, Influence of chromium on the flow-accelerated corrosion behavior of low alloy steels in 3.5% NaCl solution, Corrosion Science. 123 (2017) 217–227. https://doi.org/10.1016/j.corsci.2017.04.024.

[14] M. Wasim, S. Shoaib, N.M. Mubarak, Inamuddin, A.M. Asiri, Factors influencing corrosion of metal pipes in soils, Environmental Chemistry Letters. 16 (2018) 861–879. https://doi.org/10.1007/s10311-018-0731-x.

[15] C. Li, Y. Ma, Y. Li, F. Wang, EIS monitoring study of atmospheric corrosion under variable relative humidity, Corrosion Science. 52 (2010) 3677–3686. https://doi.org/10.1016/j.corsci.2010.07.018.

[16] D. Enning, J. Garrelfs, Corrosion of iron by sulfate-reducing bacteria: New views of an old problem, Applied and Environmental Microbiology. 80 (2014) 1226–1236. https://doi.org/10.1128/AEM.02848-13.

[17] C.A. Loto, Microbiological corrosion: mechanism, control and impact—a review, International Journal of Advanced Manufacturing Technology. 92 (2017) 4241–4252. https://doi.org/10.1007/s00170-017-0494-8.

[18] J.T. Busby, G.S. Was, E.A. Kenik, Isolating the effect of radiation-induced segregation in irradiation-assisted stress corrosion cracking of austenitic stainless steels, Journal of Nuclear Materials. 302 (2002) 20–40. https://doi.org/10.1016/S0022-3115(02)00719-5.

[19] Å. Björkbacka, S. Hosseinpour, M. Johnson, C. Leygraf, M. Jonsson, Radiation induced corrosion of copper for spent nuclear fuel storage, Radiation Physics and Chemistry. 92 (2013) 80–86. https://doi.org/10.1016/j.radphyschem.2013.06.033.

[20] M.A. Uusitalo, P.M.J. Vuoristo, T.A. Mäntylä, High temperature corrosion of coatings and boiler steels below chlorine-containing salt deposits, Corrosion Science. 46 (2004) 1311–1331. https://doi.org/10.1016/j.corsci.2003.09.026.

[21] R. Jia, T. Unsal, D. Xu, Y. Lekbach, T. Gu, Microbiologically influenced corrosion and current mitigation strategies: A state of the art review, International Biodeterioration and Biodegradation. 137 (2019) 42–58. https://doi.org/10.1016/j.ibiod.2018.11.007.

[22] A. Popoola, O. Olorunniwo, O. Ige, Corrosion Resistance Through the Application of Anti-Corrosion Coatings, in: Developments in Corrosion Protection, InTech, 2014. https://doi.org/10.5772/57420.

[23] Standard Potentials at 25°C, (n.d.). https://gchem.cm.utexas.edu/data/standard-potentials.php.

[24] A.J. Bard, L.R. Faulkner, ELECTROCHEMICAL METHODS Fundamentals and Applications, 2015. https://doi.org/10.1016/B978-0-08-098353-0.00003-8.

[25] H. Shirakawa, E.J. Louis, A.G. MacDiarmid, C.K. Chiang, A.J. Heeger, Synthesis of electrically conducting organic polymers: Halogen derivatives of polyacetylene, (CH)x, Journal of the Chemical Society, Chemical Communications. (1977) 578–580. https://doi.org/10.1039/C39770000578.

[26] T. David, J.K. Mathad, T. Padmavathi, A. Vanaja, Part-A: Synthesis of polyaniline and carboxylic acid functionalized SWCNT composites for electromagnetic interference shielding coatings, Polymer. 55 (2014) 5665–5672. https://doi.org/10.1016/j.polymer.2014.09.007.

[27] W. Prissanaroon, N. Brack, P.J. Pigram, J. Liesegang, Electropolymerisation of pyrrole on copper in aqueous media, Synthetic Metals. 142 (2004) 25–34. https://doi.org/10.1016/j.synthmet.2003.07.010.

[28] D.W. DeBerry, Modification of the Electrochemical and Corrosion Behavior of Stainless Steels With an Electroactive Coating., Journal of the Electrochemical Society. 132 (1985) 1022–1026. https://doi.org/10.1149/1.2114008.

[29] G. Mengoli, M.M. Musiani, B. Pelli, E. Vecchi, Anodic synthesis of sulfur-bridged polyaniline coatings onto Fe sheets, J Appl Polym Sci. 28 (1983) 1125–1136. https://doi.org/10.1002/app.1983.070280318.

[30] Y. Zhang, Y. Shao, X. Liu, C. Shi, Y. Wang, G. Meng, X. Zeng, Y. Yang, A study on corrosion protection of different polyaniline coatings for mild steel, Prog Org Coat. 111 (2017) 240–247. https://doi.org/10.1016/j.porgcoat.2017.06.015.

[31] J.E.P. da Silva, S.I.C. de Torresi, R.M. Torresi, Polyaniline/poly(methylmethacrylate) blends for corrosion protection: The effect of passivating dopants on different metals, Progress in Organic Coatings. 58 (2007) 33–39. https://doi.org/10.1016/j.porgcoat.2006.11.005.

[32] P.J. Kinlen, V. Menon, Y. Ding, A mechanistic investigation of polyaniline corrosion protection using the scanning reference electrode technique, Journal of the Electrochemical Society. 146 (1999) 3690–3695. https://doi.org/10.1149/1.1392535.

[33] R. Gašparac, C.R. Martin, Investigations of the Mechanism of Corrosion Inhibition by Polyaniline: Polyaniline-Coated Stainless Steel in Sulfuric Acid Solution, Journal of the Electrochemical Society. 148 (2001) 138–145. https://doi.org/10.1149/1.1354615.

[34] M. Shabani-Nooshabadi, F. Karimian-Taheri, Electrosynthesis of a polyaniline/zeolite nanocomposite coating on copper in a three-step process and the effect of current density on its corrosion protection performance, RSC Adv. 5 (2015) 96601–96610. https://doi.org/10.1039/C5RA14333K.

[35] M. Ates, E. Topkaya, Nanocomposite film formations of polyaniline via TiO2, Ag, and Zn, and their corrosion protection properties, Progress in Organic Coatings. 82 (2015) 33–40. https://doi.org/10.1016/j.porgcoat.2015.01.014.

[36] S. Kim, T.H. Le, C.S. Park, G. Park, K.H. Kim, S. Kim, O.S. Kwon, G.T. Lim, H. Yoon, A solution-processable, nanostructured, and conductive graphene/polyaniline hybrid coating for metal-corrosion protection and monitoring, Scientific Reports. 7 (2017) 1–9. https://doi.org/10.1038/s41598-017-15552-w.

[37] B. Ramezanzadeh, M.H. Mohamadzadeh Moghadam, N. Shohani, M. Mahdavian, Effects of highly crystalline and conductive polyaniline/graphene oxide composites on the corrosion protection

performance of a zinc-rich epoxy coating, Chemical Engineering Journal. 320 (2017) 363–375. https://doi.org/10.1016/j.cej.2017.03.061.

[38] Q. Yan, W. Pan, S. Zhong, R. Zhu, G. Li, Effect of solvents on the preparation and corrosion protection of polypyrrole, Progress in Organic Coatings. 132 (2019) 298–304. https://doi.org/10.1016/j.porgcoat.2019.04.014.

[39] M. Eslami, F. Deflorian, C. Zanella, Electrochemical performance of polypyrrole coatings electrodeposited on rheocast aluminum-silicon components, Progress in Organic Coatings. 137 (2019). https://doi.org/10.1016/j.porgcoat.2019.105307.

[40] H.M. Hung, D.K. Linh, N.T. Chinh, L.M. Duc, V.Q. Trung, Improvement of the corrosion protection of polypyrrole coating for CT3 mild steel with 10-camphorsulfonic acid and molybdate as inhibitor dopants, Progress in Organic Coatings. 131 (2019) 407–416. https://doi.org/10.1016/j.porgcoat.2019.03.006.

[41] J. Tan, Z. Zhang, D. Ge, Electrodeposition of Adherent Polypyrrole Film on Titanium Surface with Enhanced Anti-corrosion Performance, MATEC Web of Conferences. 130 (2017) 08007. https://doi.org/10.1051/matecconf/201713008007.

[42] A. V. Syugaev, N. V. Lyalina, A.N. Maratkanova, D.A. Smirnov, Molecular architecture of highly protective coatings of electrodeposited dodecyl sulfate-doped polypyrrole, Progress in Organic Coatings. 131 (2019) 427–434. https://doi.org/10.1016/j.porgcoat.2019.03.018.

[43] Y. Ding, J. Zhong, P. Xie, J. Rong, H. Zhu, W. Zheng, J. Wang, F. Gao, L. Shen, H. He, Z. Cheng, Protection of Mild Steel by Waterborne Epoxy Coatings Incorporation of Polypyrrole Nanowires/Graphene Nanocomposites, Polymers. 11 (2019) 1998. https://doi.org/10.3390/polym11121998.

[44] Q. Zhu, E. Li, X. Liu, W. Song, Y. Li, X. Wang, C. Liu, Epoxy coating with in-situ synthesis of polypyrrole functionalized graphene oxide for enhanced anticorrosive performance, Progress in Organic Coatings. 140 (2020). https://doi.org/10.1016/j.porgcoat.2019.105488.

[45] R. Mohammadkhani, M. Ramezanzadeh, S. Saadatmandi, B. Ramezanzadeh, Designing a dual-functional epoxy composite system with self-healing/barrier anti-corrosion performance using graphene oxide nano-scale platforms decorated with zinc doped-conductive polypyrrole nanoparticles with great environmental stability and non-tox, Chemical Engineering Journal. 382 (2020) 122819. https://doi.org/10.1016/j.cej.2019.122819.

[46] G. Kousik, S. Pitchumani, N.G. Renganathan, Electrochemical characterization of polythiophene-coated steel, Progress in Organic Coatings. 43 (2001) 286–291. https://doi.org/10.1016/S0300-9440(01)00211-9.

[47] A.C.C. De Leon, R.B. Pernites, R.C. Advincula, Superhydrophobic colloidally textured polythiophene film as superior anticorrosion coating, ACS Applied Materials and Interfaces. 4 (2012) 3169–3176. https://doi.org/10.1021/am300513e.

[48] L. Ai, Y. Liu, X.Y. Zhang, X.H. Ouyang, Z.Y. Ge, A facile and template-free method for preparation of polythiophene microspheres and their dispersion for waterborne corrosion protection coatings, Synth Met. 191 (2014) 41–46. https://doi.org/10.1016/j.synthmet.2014.02.004.

[49] S.J. Richard Prabakar, M. Pyo, Corrosion protection of aluminum in LiPF 6 by poly(3,4-ethylenedioxythiophene) nanosphere-coated multiwalled carbon nanotube, Corrosion Science. 57 (2012) 42–48. https://doi.org/10.1016/j.corsci.2011.12.036.

[50] X. Bai, T.H. Tran, D. Yu, A. Vimalanandan, X. Hu, M. Rohwerder, Novel conducting polymer based composite coatings for corrosion protection of zinc, Corrosion Science. 95 (2015) 110–116. https://doi.org/10.1016/j.corsci.2015.03.003.

[51] M. Rohwerder, Conducting polymers for corrosion protection: A review, Zeitschrift Fuer Metallkunde/Materials Research and Advanced Techniques. 100 (2009) 1331. https://doi.org/10.3139/146.110205.

[52] B. Wrssling, Passivation of Metals by Coating with Polyaniline : Corrosion Potential Shift and Morphological Changes, Adv. Mater. 6 (1994) 226–228. https://doi.org/10.1002/cind.7812_19.x.

[53] B. Wessling, Corrosion prevention with an organic metal (polyaniline): Surface ennobling, passivation, corrosion test results, Materials and Corrosion - Werkstoffe Und Korrosion. 47 (1996) 439–445. https://doi.org/10.1002/maco.19960470804.

[54] P.P. Deshpande, N.G. Jadhav, V.J. Gelling, D. Sazou, Conducting polymers for corrosion protection: A review, Journal of Coatings Technology Research. 11 (2014) 473–494. https://doi.org/10.1007/s11998-014-9586-7.

[55] S. De Souza, J.E. Pereira Da Silva, S.I. Córdoba De Torresi, M.L.A. Temperini, R.M. Torresi, Polyaniline based acrylic blends for iron corrosion protection, Electrochemical and Solid-State Letters. 4 (2001) 27–30. https://doi.org/10.1149/1.1381288.

[56] G. Paliwoda-Porebska, M. Stratmann, M. Rohwerder, K. Potje-Kamloth, Y. Lu, A.Z. Pich, H.J. Adler, On the development of polypyrrole coatings with self-healing properties for iron corrosion protection, Corrosion Science. 47 (2005) 3216–3233. https://doi.org/10.1016/j.corsci.2005.05.057.

[57] M. Rohwerder, Conducting polymers for corrosion protection: A Critical review, Zeitschrift Fuer Metallkunde/Materials Research and Advanced Techniques. 100 (2009) 1331. https://doi.org/10.3139/146.110205.

[58] S. Vigneshvar, C.C. Sudhakumari, B. Senthilkumaran, H. Prakash, Recent Advances in Biosensor Technology for Potential Applications – An Overview, Frontiers in Bioengineering and Biotechnology. 4 (2016) 1–9. https://doi.org/10.3389/fbioe.2016.00011.

[59] T.F. McGrath, K. Andersson, K. Campbell, T.L. Fodey, C.T. Elliott, Development of a rapid low cost fluorescent biosensor for the detection of food contaminants, Biosensors and Bioelectronics. 41 (2013) 96–102. https://doi.org/10.1016/j.bios.2012.07.081.

[60] C. Justino, A. Duarte, T. Rocha-Santos, Recent Progress in Biosensors for Environmental Monitoring: A Review, Sensors. 17 (2017) 2918. https://doi.org/10.3390/s17122918.

[61] J. Li, Y. Yu, Y. Wang, J. Qian, J. Zhi, The benzoquinone-mediated electrochemical microbial biosensor for water biotoxicity assay, Electrochimica Acta. 97 (2013) 52–57. https://doi.org/10.1016/j.electacta.2013.02.071.

[62] S.M.Z. Hossain, N. Mansour, Biosensors for on-line water quality monitoring – a review, Arab J Basic Appl Sci. 26 (2019) 502–518. https://doi.org/10.1080/25765299.2019.1691434.

[63] S. Cagnin, M. Caraballo, C. Guiducci, P. Martini, M. Ross, M. SantaAna, D. Danley, T. West, G. Lanfranchi, Overview of Electrochemical DNA Biosensors: New Approaches to Detect the Expression of Life, Sensors. 9 (2009) 3122–3148. https://doi.org/10.3390/s90403122.

[64] D. Yu, B. Blankert, J. Viré, J. Kauffmann, Biosensors in Drug Discovery and Drug Analysis, Analytical Letters. 38 (2005) 1687–1701. https://doi.org/10.1080/00032710500205659.

[65] T. Zhou, H. Han, P. Liu, J. Xiong, F. Tian, X. Li, Microbial fuels cell-based biosensor for toxicity detection: A review, Sensors (Switzerland). 17 (2017) 1–21. https://doi.org/10.3390/s17102230.

[66] N. Bhalla, P. Jolly, N. Formisano, P. Estrela, Introduction to biosensors, Essays in Biochemistry. 60 (2016) 1–8. https://doi.org/10.1042/EBC20150001.

[67] V. Naresh, N. Lee, A review on biosensors and recent development of nanostructured materials-enabled biosensors, Sensors (Switzerland). 21 (2021) 1–35. https://doi.org/10.3390/s21041109.

[68] R. Kumar, S. Sahoo, E. Joanni, R.K. Singh, K.K. Kar, Microwave as a Tool for Synthesis of Carbon-Based Electrodes for Energy Storage, ACS Applied Materials and Interfaces. (2021). https://doi.org/10.1021/acsami.1c15934.

[69] S. Ravichandran, E. Karthikeyan, Microwave synthesis - A potential tool for green chemistry, International Journal of ChemTech Research. 3 (2011) 466–470.

[70] X. Zhang, Z. Liu, Recent advances in microwave initiated synthesis of nanocarbon materials, Nanoscale. 4 (2012) 707–714. https://doi.org/10.1039/C2NR11603K.

[71] G. Kear, B.D. Barker, F.C. Walsh, Electrochemical corrosion of unalloyed copper in chloride media--a critical review, Corrosion Science. 46 (2004) 109–135. https://doi.org/10.1016/S0010-938X(02)00257-3.

[72] A. El Warraky, H.A. El Shayeb, E.M. Sherif, Pitting corrosion of copper in chloride solutions, Anti-Corrosion Methods and Materials. 51 (2004) 52–61. https://doi.org/10.1108/00035590410512735.

[73] M.M. Antonijevic, M.B. Petrovic Mihajlovic, Copper Corrosion Inhibitors. Period 2008-2014. A Review, International Journal of Electrochemical Science. 10 (2015) 1027–1053.

[74] M. Finšgar, I. Milošev, Inhibition of copper corrosion by 1,2,3-benzotriazole: A review, Corrosion Science. 52 (2010) 2737–2749. https://doi.org/10.1016/j.corsci.2010.05.002.

[75] S.M. Milić, M.M. Antonijević, Some aspects of copper corrosion in presence of benzotriazole and chloride ions, Corrosion Science. 51 (2009) 28–34. https://doi.org/10.1016/j.corsci.2008.10.007.

[76] M. Ates, A review on conducting polymer coatings for corrosion protection, Journal of Adhesion Science and Technology. 30 (2016) 1510–1536. https://doi.org/10.1080/01694243.2016.1150662.

[77] U. Riaz, S.M. Ashraf, S. Ahmad, High performance corrosion protective DGEBA/polypyrrole composite coatings, Progress in Organic Coatings. 59 (2007) 138–145. https://doi.org/10.1016/j.porgcoat.2007.02.002.

[78] R. Hasanov, S. Bilgiç, Monolayer and bilayer conducting polymer coatings for corrosion protection of steel in 1 M H2SO4 solution, Progress in Organic Coatings. 64 (2009) 435–445. https://doi.org/10.1016/j.porgcoat.2008.08.004.

[79] P. Hlilser, F. Beck, Electrodeposition of Polypyrrole Powder on Aluminum from Aqueous Electrolytes, J. Electrochem. Soc. 137 (1990) 2067–2069. http://jes.ecsdl.org/content/137/7/2067.full.pdf.

[80] F. Beck, R. Michaelis, F. Schloten, B. Zinger, Filmforming electropolymerization of pyrrole on iron in aqueous oxalic acid, Electrochimica Acta. 39 (1994) 229–234. https://doi.org/10.1016/0013-4686(94)80058-8.

[81] A. Nautiyal, M. Qiao, J.E. Cook, X. Zhang, T.S. Huang, High performance polypyrrole coating for corrosion protection and biocidal applications, Appl Surf Sci. 427 (2018) 922–930. https://doi.org/10.1016/j.apsusc.2017.08.093.

[82] S. Aksu, Electrochemistry of copper in aqueous oxalic acid solutions, Journal of the Electrochemical Society. 152 (2005) 938–943. https://doi.org/10.1149/1.2121737.

[83] J.L. Camalet, J.C. Lacroix, S. Aeiyach, P.C. Lacaze, Characterization of polyaniline films electrodeposited on mild steel in aqueous p-toluenesulfonic acid solution, Journal of Electroanalytical Chemistry. 445 (1998) 117–124. https://doi.org/10.1016/S0022-0728(97)00526-3.

[84] K. Naoi, M. Takeda, H. Kanno, M. Sakakura, A. Shimada, Simultaneous electrochemical formation of Al2O3/polypyrrole layers (I): Effect of electrolyte anion in formation process, Electrochim Acta. 45 (2000) 3413–3421. https://doi.org/10.1016/S0013-4686(00)00423-0.

[85] A.C. Cascalheira, S. Aeiyach, P.C. Lacaze, L.M. Abrantes, Electrochemical synthesis and redox behaviour of polypyrrole coatings on copper in salicylate aqueous solution, Electrochim Acta. 48 (2003) 2523–2529. https://doi.org/10.1016/S0013-4686(03)00295-0.

[86] S. Biallozor, A. Kupniewska, Conducting polymers electrodeposited on active metals, Synth Met. 155 (2005) 443–449. https://doi.org/10.1016/j.synthmet.2005.09.002.

[87] J.L. Camalet, J.C. Lacroix, S. Aeiyach, K. Chane-Ching, P.C. Lacaze, Electrodeposition of protective polyaniline films on mild steel, Journal of Electroanalytical Chemistry. 416 (1996) 179–182. https://doi.org/10.1016/S0022-0728(96)01012-1.

[88] J. Petitjean, S. Aeiyach, J.C. Lacroix, P.C. Lacaze, Ultra-fast electropolymerization of pyrrole in aqueous media on oxidizable metals in a one-step process, Journal of Electroanalytical Chemistry. 478 (1999) 92–100. https://doi.org/10.1016/S0022-0728(99)00418-0.

[89] P. Herrasti, A.I. del Rio, J. Recio, Electrodeposition of homogeneous and adherent polypyrrole on copper for corrosion protection, Electrochim Acta. 52 (2007) 6496–6501. https://doi.org/10.1016/j.electacta.2007.04.074.

[90] L.M. Martins Dos Santos, J.C. Lacroix, K.I. Chane-Ching, A. Adenier, L.M. Abrantes, P.C. Lacaze, Electrochemical synthesis of polypyrrole films on copper electrodes in acidic and neutral aqueous media, Journal of Electroanalytical Chemistry. 587 (2006) 67–78. https://doi.org/10.1016/j.jelechem.2005.10.015.

[91] A.C. Cascalheira, S. Aeiyach, J. Aubard, P.C. Lacaze, L.M. Abrantes, Electropolymerization of pyrrole on oxidizable metals: Role of salicylate ions in the anodic behavior of copper, Russian Journal of Electrochemistry. 40 (2004) 294–298. https://doi.org/10.1023/B:RUEL.0000019667.90230.22.

[92] A.C. Cascalheira, L.M. Abrantes, The electrochemical behaviour of copper in sodium salicylate aqueous solutions, Electrochim Acta. 49 (2004) 5023–5028. https://doi.org/10.1016/j.electacta.2004.05.046.

[93] K. Shah, J. Iroh, Electrochemical synthesis and corrosion behavior of poly (N -ethyl aniline) coatings on Al-2024 alloy, Synth Met. 132 (2002) 35–41. https://doi.org/10.1016/S0379-6779(02)00213-8.

[94] T. Ohtsuka, Corrosion protection of steels by conducting polymer coating, International Journal of Corrosion. 2012 (2012). https://doi.org/10.1155/2012/915090.

[95] D.K. Ariyanayagamkumarappa, I. Zhitomirsky, Electropolymerization of polypyrrole films on stainless steel substrates for electrodes of electrochemical supercapacitors, Synth Met. 162 (2012) 868–872. https://doi.org/10.1016/j.synthmet.2012.03.020.

[96] S. Kim, L.K. Jang, H.S. Park, J.Y. Lee, Electrochemical deposition of conductive and adhesive polypyrrole-dopamine films, Sci Rep. 6 (2016) 1–8. https://doi.org/10.1038/srep30475.

[97] S. Chen, I. Zhitomirsky, Influence of dopants and carbon nanotubes on polypyrrole electropolymerization and capacitive behavior, Mater Lett. 98 (2013) 67–70. https://doi.org/10.1016/j.matlet.2013.01.123.

[98] B.H. Cruz, J.M. Díaz-Cruz, C. Ariño, M. Esteban, Heavy metal binding by tannic acid: A voltammetric study, Electroanalysis. 12 (2000) 1130–1137. https://doi.org/10.1002/1521-4109(200010)12:14<1130::AID-ELAN1130>3.0.CO;2-7.

[99] Z. Fu, R. Chen, Study of complexes of tannic acid with Fe(III) and Fe(II), J Anal Methods Chem. 2019 (2019). https://doi.org/10.1155/2019/3894571.

[100] B. Zhu, S. Wang, L. Wang, Y. Yang, J. Liang, B. Cao, Preparation of Hydroxyapatite/Tannic Acid Coating to Enhance the Corrosion Resistance and Cytocompatibility of AZ31 Magnesium Alloys, Coatings. 7 (2017) 105. https://doi.org/10.3390/coatings7070105.

[101] A.M. Beccaria, E.D. Mor, Inhibitive effect of tannic acid on the corrosion of copper in acid solutions, British Corrosion Journal. 11 (1976) 156–160. https://doi.org/10.1179/000705976798320007.

[102] E. Kusmierek, E. Chrzescijanska, Tannic acid as corrosion inhibitor for metals and alloys, Materials and Corrosion. 66 (2015) 169–174. https://doi.org/10.1002/maco.201307277.

[103] B. Doɨru Mert, Corrosion protection of aluminum by electrochemically synthesized composite organic coating, Corrosion Science. 103 (2016) 88–94. https://doi.org/10.1016/j.corsci.2015.11.008.

[104] M. Sharifirad, A. Omrani, A.A. Rostami, M. Khoshroo, Electrodeposition and characterization of polypyrrole films on copper, Journal of Electroanalytical Chemistry. 645 (2010) 149–158. https://doi.org/10.1016/j.jelechem.2010.05.005.

[105] M. Bazzaoui, J.I. Martins, E.A. Bazzaoui, T.C. Reis, L. Martins, Pyrrole electropolymerization on copper and brass in a single-step process from aqueous solution, J Appl Electrochem. 34 (2004) 815–822. https://doi.org/10.1023/B:JACH.0000035610.10869.43.

[106] K. Rajar, R.A. Soomro, Z.H. Ibupoto, Sirajuddin, A. Balouch, Tannic acid assisted copper oxide nanoglobules for sensitive electrochemical detection of bisphenol A, International Journal of Food Properties. 20 (2017) 1359–1367. https://doi.org/10.1080/10942912.2016.1209776.

[107] A.M. Kumar, R.S. Babu, S. Ramakrishna, A.L.F. de Barros, Electrochemical synthesis and surface protection of polypyrrole-CeO2nanocomposite coatings on AA2024 alloy, Synth Met. 234 (2017) 18–28. https://doi.org/10.1016/j.synthmet.2017.10.003.

[108] V. Annibaldi, A.D.D. Rooney, C.B.B. Breslin, Corrosion protection of copper using polypyrrole electrosynthesised from a salicylate solution, Corrosion Science. 59 (2012) 179–185. https://doi.org/10.1016/j.corsci.2012.03.014.

[109] Y. Jafari, S.M. Ghoreishi, M. Shabani-Nooshabadi, Polyaniline/Graphene nanocomposite coatings on copper: Electropolymerization, characterization, and evaluation of corrosion protection performance, Synthetic Metals. 217 (2016) 220–230. https://doi.org/10.1016/j.synthmet.2016.04.001.

[110] U. Carragher, C.B. Breslin, Polypyrrole doped with dodecylbenzene sulfonate as a protective coating for copper, Electrochimica Acta. 291 (2018) 362–372. https://doi.org/10.1016/j.electacta.2018.08.155.

[111] S. Wan, C.H. Miao, R.M. Wang, Z.F. Zhang, Z.H. Dong, Enhanced corrosion resistance of copper by synergetic effects of silica and BTA codoped in polypyrrole film, Progress in Organic Coatings. 129 (2019) 187–198. https://doi.org/10.1016/j.porgcoat.2019.01.014.

[112] Afaf M. Abd El-Hameed, Y. A. Abdel-Aziz, Aluminium Alloys in Space Applications: A Short Report, Journal of Advanced Research in Applied Sciences and Engineering Technology. 22 (2021) 1–7. https://doi.org/10.37934/araset.22.1.17.

[113] R.L. Twite, G.P. Bierwagen, Review of alternatives to chromate for corrosion protection of aluminum aerospace alloys, Prog Org Coat. 33 (1998) 91–100. https://doi.org/10.1016/S0300-9440(98)00015-0.

[114] F. Peltier, Review of Cr-Free Coatings for the Corrosion Protection of, (2022) 1–27.

[115] J. Sinko, Challenges of chromate inhibitor pigments replacement in organic coatings, Prog Org Coat. 42 (2001) 267–282. https://doi.org/10.1016/S0300-9440(01)00202-8.

[116] M. Mrad, Y. Ben Amor, L. Dhouibi, F. Montemor, Electrochemical study of polyaniline coating electropolymerized onto AA2024-T3 aluminium alloy: Physical properties and anticorrosion performance, Synth Met. 234 (2017) 145–153. https://doi.org/10.1016/j.synthmet.2017.11.002.

[117] N. Jadhav, M.B. Jensen, V. Gelling, Tungstate and vanadate-doped polypyrrole / aluminum flake composite coatings for the corrosion protection of aluminum 2024-T3, 12 (2015) 259–276. https://doi.org/10.1007/s11998-014-9633-4.

[118] L. Jiang, J.A. Syed, H. Lu, X. Meng, In-situ electrodeposition of conductive polypyrrole-graphene oxide composite coating for corrosion protection of 304SS bipolar plates, J Alloys Compd. 770 (2019) 35–47. https://doi.org/10.1016/j.jallcom.2018.07.277.

[119] R. Ansari, Polypyrrole Conducting Electroactive Polymers: Synthesis and Stability Studies, E-Journal of Chemistry. 3 (2006) 186–201. https://doi.org/10.1155/2006/860413.

[120] X. Hong, Y. Liu, Y. Li, X. Wang, J. Fu, X. Wang, Application progress of polyaniline, polypyrrole and polythiophene in lithium-sulfur batteries, Polymers (Basel). 12 (2020). https://doi.org/10.3390/polym12020331.

[121] Y. Huang, H. Li, Z. Wang, M. Zhu, Z. Pei, Q. Xue, Y. Huang, C. Zhi, Nanostructured Polypyrrole as a flexible electrode material of supercapacitor, Nano Energy. 22 (2016) 422–438. https://doi.org/10.1016/j.nanoen.2016.02.047.

[122] R. Jain, N. Jadon, A. Pawaiya, Polypyrrole based next generation electrochemical sensors and biosensors: A review, TrAC - Trends in Analytical Chemistry. 97 (2017) 363–373. https://doi.org/10.1016/j.trac.2017.10.009.

[123] G. Kaur, R. Adhikari, P. Cass, M. Bown, P. Gunatillake, Electrically conductive polymers and composites for biomedical applications, RSC Adv. 5 (2015) 37553–37567. https://doi.org/10.1039/c5ra01851j.

[124] B. Alshammary, F.C. Walsh, P. Herrasti, C. Ponce de Leon, Electrodeposited conductive polymers for controlled drug release: polypyrrole, Journal of Solid State Electrochemistry. 20 (2016) 839–859. https://doi.org/10.1007/s10008-015-2982-9.

[125] M.K. Zadeh, M. Yeganeh, M.T. Shoushtari, A. Esmaeilkhanian, Corrosion performance of polypyrrole-coated metals: A review of perspectives and recent advances, Synth Met. 274 (2021) 116723. https://doi.org/10.1016/j.synthmet.2021.116723.

[126] S. Sadki, P. Schottland, N. Brodie, G. Sabouraud, The mechanisms of pyrrole electropolymerization, Chem Soc Rev. 29 (2000) 283–293. https://doi.org/10.1039/a807124a.

[127] A.S. Liu, M.A.S. Oliveira, Corrosion control of aluminum surfaces by polypyrrole films: Influence of electrolyte, Materials Research. 10 (2007) 205–209. https://doi.org/10.1590/S1516-14392007000200018.

[128] L. Jiang, J.A. Syed, Y. Gao, Q. Zhang, J. Zhao, H. Lu, X. Meng, Electropolymerization of camphorsulfonic acid doped conductive polypyrrole anti-corrosive coating for 304SS bipolar plates, Appl Surf Sci. 426 (2017) 87–98. https://doi.org/10.1016/j.apsusc.2017.07.077.

[129] R. Vera, R. Schrebler, P. Grez, H. Romero, The corrosion-inhibiting effect of polypyrrole films doped with p-toluene-sulfonate, benzene-sulfonate or dodecyl-sulfate anions, as coating on stainless steel in NaCl aqueous solutions, Prog Org Coat. 77 (2014) 853–858. https://doi.org/10.1016/j.porgcoat.2014.01.015.

[130] W. Zhou, K. Wu, K. Zhang, Z. Wang, Z. Liu, S. Hu, Y. Fang, C. He, Studies on Corrosion Behaviors of Q235 Steel Coated by the Polypyrrole Films Doped with different dopants, Int J Electrochem Sci. 15 (2020) 2594–2603. https://doi.org/10.20964/2020.03.49.

[131] L.M. Vračar, D.M. Draži, Adsorption and corrosion inhibitive properties of some organic molecules on iron electrode in sulfuric acid, Corros Sci. 44 (2002) 1669–1680. https://doi.org/10.1016/S0010-938X(01)00166-4.

[132] P. Hu, Z. Wu, J. Wang, Y. Huang, Q. Liu, S.F. Zhou, Corrosion inhibiting performance and mechanism of protic ionic liquids as green brass inhibitors in nitric acid, Green Energy and Environment. 5 (2020) 214–222. https://doi.org/10.1016/j.gee.2019.11.003.

[133] L.F. Warren, J.A. Walker, D.P. Anderson, C.G. Rhodes, L.J. Buckley, A Study of Conducting Polymer Morphology: The Effect of Dopant Anions Upon Order, J Electrochem Soc. 136 (1989) 2286–2295. https://doi.org/10.1149/1.2097303.

[134] L. Qu, G. Shi, F. Chen, J. Zhang, Electrochemical growth of polypyrrole microcontainers, Macromolecules. 36 (2003) 1063–1067. https://doi.org/10.1021/ma021177b.

[135] T. Patois, B. Lakard, S. Monney, X. Roizard, P. Fievet, Characterization of the surface properties of polypyrrole films: Influence of electrodeposition parameters, Synth Met. 161 (2011) 2498–2505. https://doi.org/10.1016/j.synthmet.2011.10.003.

[136] A.A. Arrieta Almario, R.L. Tarazona Cáceres, Study of kinetic formation and the electrochemical behavior of polypyrrole films, Journal of the Chilean Chemical Society. 54 (2009) 14–19. https://doi.org/10.4067/S0717-97072009000100004.

[137] K.R.L. Castagno, D.S. Azambuja, V. Dalmoro, Polypyrrole electropolymerized on aluminum alloy 1100 doped with oxalate and tungstate anions, J Appl Electrochem. 39 (2009) 93–100. https://doi.org/10.1007/s10800-008-9640-1.

[138] K.R.L.L. Castagno, V. Dalmoro, D.S. Azambuja, Characterization and corrosion of polypyrrole/sodium dodecylbenzene sulfonate electropolymerised on aluminum alloy 1100, Mater Chem Phys. 130 (2011) 721–726. https://doi.org/10.1016/j.matchemphys.2011.07.052.

[139] K.L. Levine, D.E. Tallman, G.P. Bierwagen, The Mediated Electrodeposition of Polypyrrole on Aluminium Alloy, Aust J Chem. 58 (2005) 294. https://doi.org/10.1071/CH04289.

[140] N. Kizilyar, L. Toppare, A. Önen, Y. Yağci, Conducting copolymers of polypyrrole/polytetrahydrofuran, Polymer Bulletin. 40 (1998) 639–645. https://doi.org/10.1007/s002890050302.

[141] L.T.T. Kim, C. Gabrielli, A. Pailleret, H. Perrot, Ions/solvent exchanges and electromechanical processes in hexasulfonated calix[6]arene doped polypyrrole films: Towards a relaxation mechanism, Electrochemical and Solid-State Letters. 14 (2011). https://doi.org/10.1149/2.022111esl.

[142] A. Shukla, K. Sen, D. Das, Studies on electrolytic and doping behavior of different compounds and their combination on the electrical resistance of polypyrrole film via electrochemical polymerization, J Appl Polym Sci. 139 (2022). https://doi.org/10.1002/app.52793.

[143] A. Santos Liu, M. Cristina Bezerra, L. Yao Cho, Electrodeposition of Polypyrrole Films on Aluminum Surfaces from a p-toluene Sulfonic Acid Medium, 2009.

[144] D.E. Tallman, C. Vang, G.G. Wallace, G.P. Bierwagen, Direct Electrodeposition of Polypyrrole on Aluminum and Aluminum Alloy by Electron Transfer Mediation, J Electrochem Soc. 149 (2002) C173. https://doi.org/10.1149/1.1448820.

[145] V. Shinde, A.B. Gaikwad, P.P. Patil, Synthesis and corrosion protection study of poly(o-ethylaniline) coatings on copper, Surf Coat Technol. 202 (2008) 2591–2602. https://doi.org/10.1016/j.surfcoat.2007.09.025.

[146] I.A. Kartsonakis, E.P. Koumoulos, A.C. Balaskas, G.S. Pappas, C.A. Charitidis, G.C. Kordas, Hybrid organic-inorganic multilayer coatings including nanocontainers for corrosion protection of metal alloys, Corros Sci. 57 (2012) 56–66. https://doi.org/10.1016/j.corsci.2011.12.034.

[147] M. Menkuer, H. Ozkazanc, Anticorrosive polypyrrole/zirconium-oxide composite film prepared in oxalic acid and dodecylbenzene sulfonic acid mix electrolyte, Prog Org Coat. 147 (2020). https://doi.org/10.1016/j.porgcoat.2020.105815.

[148] A.C. Balaskas, I.A. Kartsonakis, G. Kordas, A.M. Cabral, P.J. Morais, Influence of the doping agent on the corrosion protection properties of polypyrrole grown on aluminium alloy 2024-T3, Prog Org Coat. 71 (2011) 181–187. https://doi.org/10.1016/j.porgcoat.2011.02.011.

[149] S.H.H. Mortazavi, M. Yeganeh, A. Etemad, M. Saremi, Corrosion behavior of polypyrrole (Ppy)coating modified by polyethylene glycol (PEG)doped ammonium bifluoride on AZ31

magnesium alloy, Prog Org Coat. 134 (2019) 22–32. https://doi.org/10.1016/j.porgcoat.2019.04.054.

[150] N. Zhu, D. Zhang, W. Wang, X. Li, B. Yang, J. Song, X. Zhao, B. Huang, W. Shi, R. Lu, P. Niu, F. Zhan, X. Ma, D. Wang, W. Xu, G. Wu, G.F. Gao, W. Tan, A Novel Coronavirus from Patients with Pneumonia in China, 2019, New England Journal of Medicine. 382 (2020) 727–733. https://doi.org/10.1056/nejmoa2001017.

[151] F. Wu, S. Zhao, B. Yu, Y.-M. Chen, W. Wang, Z.-G. Song, Y. Hu, Z.-W. Tao, J.-H. Tian, Y.-Y. Pei, M.-L. Yuan, Y.-L. Zhang, F.-H. Dai, Y. Liu, Q.-M. Wang, J.-J. Zheng, L. Xu, E.C. Holmes, Y.-Z. Zhang, A new coronavirus associated with human respiratory disease in China, Nature. 579 (2020) 265–269. https://doi.org/10.1038/s41586-020-2008-3.

[152] O. Gaidai, Y. Xing, A Novel Multi Regional Reliability Method for COVID-19 Death Forecast, Engineered Science. (2022) 1–16. https://doi.org/10.30919/es8d799.

[153] O. Gaidai, Y. Yihan, A novel bio-system reliability approach for multi-state COVID-19 epidemic forecast, Engineered Science. (2022) 1–18. https://doi.org/10.30919/es8d797.

[154] A.P. Chaudhary, N.S. Sonar, J. TR, M. Banerjee, S. Yadav, Impact of the COVID-19 Pandemic on the Mental Health of College Students in India: Cross-sectional Web-Based Study, JMIRx Med. 2 (2021) e28158. https://doi.org/10.2196/28158.

[155] W. Guan, Z. Ni, Y. Hu, W. Liang, C. Ou, J. He, L. Liu, H. Shan, C. Lei, D.S.C. Hui, B. Du, L. Li, G. Zeng, K.-Y. Yuen, R. Chen, C. Tang, T. Wang, P. Chen, J. Xiang, S. Li, J. Wang, Z. Liang, Y. Peng, L. Wei, Y. Liu, Y. Hu, P. Peng, J. Wang, J. Liu, Z. Chen, G. Li, Z. Zheng, S. Qiu, J. Luo, C. Ye, S. Zhu, N. Zhong, Clinical Characteristics of Coronavirus Disease 2019 in China, New England Journal of Medicine. 382 (2020) 1708–1720. https://doi.org/10.1056/NEJMoa2002032.

[156] X. Yang, Y. Yu, J. Xu, H. Shu, J. Xia, H. Liu, Y. Wu, L. Zhang, Z. Yu, M. Fang, T. Yu, Y. Wang, S. Pan, X. Zou, S. Yuan, Y. Shang, Clinical course and outcomes of critically ill patients with SARS-CoV-2 pneumonia in Wuhan, China: a single-centered, retrospective, observational study, Lancet Respir Med. 8 (2020) 475–481. https://doi.org/10.1016/S2213-2600(20)30079-5.

[157] C. Zhang, J. Sun, S. Lyu, Z. Lu, T. Li, Y. Yang, B. Li, H. Han, B. Wu, H. Sun, D. Li, J. Huang, D. Sun, Poly(lactic acid)/artificially cultured diatom frustules nanofibrous membranes with fast and controllable degradation rates for air filtration, Advanced Composites and Hybrid Materials. 5 (2022) 1221–1232. https://doi.org/10.1007/s42114-022-00474-7.

[158] P. Rai, B.K. Kumar, V.K. Deekshit, I. Karunasagar, I. Karunasagar, Detection technologies and recent developments in the diagnosis of COVID-19 infection, Applied Microbiology and Biotechnology. 105 (2021) 441–455. https://doi.org/10.1007/s00253-020-11061-5.

[159] A. Liu, K. Wang, S. Weng, Y. Lei, L. Lin, W. Chen, X. Lin, Y. Chen, Development of electrochemical DNA biosensors, TrAC Trends in Analytical Chemistry. 37 (2012) 101–111. https://doi.org/10.1016/j.trac.2012.03.008.

[160] K. Kerman, M. Kobayashi, E. Tamiya, Recent trends in electrochemical DNA biosensor technology, Meas Sci Technol. 15 (2004) R1–R11. https://doi.org/10.1088/0957-0233/15/2/R01.

[161] K.J. Odenthal, J.J. Gooding, An introduction to electrochemical DNA biosensors., The Analyst. 132 (2007) 603–10. https://doi.org/10.1039/b701816a.

[162] A. Sassolas, B.D. Leca-Bouvier, L.J. Blum, DNA biosensors and microarrays., Chem Rev. 108 (2008) 109–39. https://doi.org/10.1021/cr0684467.

[163] M. Lv, Y. Liu, J. Geng, X. Kou, Z. Xin, D. Yang, Engineering nanomaterials-based biosensors for food safety detection, Biosens Bioelectron. 106 (2018) 122–128. https://doi.org/10.1016/j.bios.2018.01.049.

[164] G. Mishra, A. Barfidokht, F. Tehrani, R. Mishra, Food Safety Analysis Using Electrochemical Biosensors, Foods. 7 (2018) 141. https://doi.org/10.3390/foods7090141.

[165] M.L. Sin, K.E. Mach, P.K. Wong, J.C. Liao, Advances and challenges in biosensor-based diagnosis of infectious diseases, Expert Rev Mol Diagn. 14 (2014) 225–244. https://doi.org/10.1586/14737159.2014.888313.

[166] E.B. Aydin, M. Aydin, M.K. Sezginturk, Biosensors in Drug Discovery and Drug Analysis, Curr Anal Chem. 15 (2019) 467–484. https://doi.org/10.2174/1573411014666180912131811.

[167] N. Izyumskaya, A. Tahira, Z.H. Ibupoto, N. Lewinski, V. Avrutin, Ü. Özgür, E. Topsakal, M. Willander, H. Morkoç, Review—Electrochemical Biosensors Based on ZnO Nanostructures, ECS Journal of Solid State Science and Technology. 6 (2017) Q84–Q100. https://doi.org/10.1149/2.0291708jss.

[168] T.G. Drummond, M.G. Hill, J.K. Barton, Electrochemical DNA sensors, Nat Biotechnol. 21 (2003) 1192–1199. https://doi.org/10.1038/nbt873.

[169] J.I.A. Rashid, N.A. Yusof, The strategies of DNA immobilization and hybridization detection mechanism in the construction of electrochemical DNA sensor: A review, Sens Biosensing Res. 16 (2017) 19–31. https://doi.org/10.1016/j.sbsr.2017.09.001.

[170] Y.-H. Wang, L.-L. He, K.-J. Huang, Y.-X. Chen, S.-Y. Wang, Z.-H. Liu, D. Li, Recent advances in nanomaterial-based electrochemical and optical sensing platforms for microRNA assays, Analyst. 144 (2019) 2849–2866. https://doi.org/10.1039/C9AN00081J.

[171] Z. Shakoori, S. Salimian, S. Kharrazi, M. Adabi, R. Saber, Electrochemical DNA biosensor based on gold nanorods for detecting hepatitis B virus., Anal Bioanal Chem. 407 (2015) 455–61. https://doi.org/10.1007/s00216-014-8303-9.

[172] M. Chen, C. Hou, D. Huo, M. Yang, H. Fa, An ultrasensitive electrochemical DNA biosensor based on a copper oxide nanowires/single-walled carbon nanotubes nanocomposite, Appl Surf Sci. 364 (2016) 703–709. https://doi.org/10.1016/j.apsusc.2015.12.203.

[173] X. Wu, F. Mu, Y. Wang, H. Zhao, Graphene and Graphene-Based Nanomaterials for DNA Detection: A Review, Molecules. 23 (2018) 2050. https://doi.org/10.3390/molecules23082050.

[174] A. Bonanni, M. Pumera, Graphene Platform for Hairpin-DNA-Based Impedimetric Genosensing, ACS Nano. 5 (2011) 2356–2361. https://doi.org/10.1021/nn200091p.

[175] X. Li, Z. Qin, H. Fu, T. Li, R. Peng, Z. Li, J.M. Rini, X. Liu, Enhancing the performance of paper-based electrochemical impedance spectroscopy nanobiosensors: An experimental approach, Biosens Bioelectron. 177 (2021) 112672. https://doi.org/10.1016/j.bios.2020.112672.

[176] G. Seo, G. Lee, M.J. Kim, S.-H. Baek, M. Choi, K.B. Ku, C.-S. Lee, S. Jun, D. Park, H.G. Kim, S.-J. Kim, J.-O. Lee, B.T. Kim, E.C. Park, S. Il Kim, Rapid Detection of COVID-19 Causative Virus (SARS-CoV-2) in Human Nasopharyngeal Swab Specimens Using Field-Effect Transistor-Based Biosensor, ACS Nano. 14 (2020) 5135–5142. https://doi.org/10.1021/acsnano.0c02823.

[177] Z. Song, Y. Ma, M. Chen, A. Ambrosi, C. Ding, X. Luo, Electrochemical Biosensor with Enhanced Antifouling Capability for COVID-19 Nucleic Acid Detection in Complex Biological Media, Analytical Chemistry. 93 (2021) 5963–5971. https://doi.org/10.1021/acs.analchem.1c00724.

[178] Z. Liu, L. Zhang, S. Poyraz, J. Smith, V. Kushvaha, H. Tippur, X. Zhang, An ultrafast microwave approach towards multi-component and multi-dimensional nanomaterials, RSC Adv. 4 (2014) 9308. https://doi.org/10.1039/c3ra47086e.

[179] F. Meng, H. Wang, F. Huang, Y. Guo, Z. Wang, D. Hui, Z. Zhou, Graphene-based microwave absorbing composites: A review and prospective, Composites Part B: Engineering. 137 (2018) 260–277. https://doi.org/10.1016/j.compositesb.2017.11.023.

[180] C. Hwang, N. Park, E.S. Kim, M. Kim, S.D. Kim, S. Park, N.Y. Kim, J.H. Kim, Ultra-fast and recyclable DNA biosensor for point-of-care detection of SARS-CoV-2 (COVID-19), Biosensors and Bioelectronics. 185 (2021) 113177. https://doi.org/10.1016/j.bios.2021.113177.

[181] B.S. Vadlamani, T. Uppal, S.C. Verma, M. Misra, Functionalized TiO2 Nanotube-Based Electrochemical Biosensor for Rapid Detection of SARS-CoV-2., Sensors (Basel, Switzerland). 20 (2020) 5871. https://doi.org/10.3390/s20205871.

[182] B. Mojsoska, S. Larsen, D.A. Olsen, J.S. Madsen, I. Brandslund, F.A. Alatraktchi, Rapid SARS-CoV-2 Detection Using Electrochemical Immunosensor, Sensors. 21 (2021) 390. https://doi.org/10.3390/s21020390.

[183] S. Ramanathan, S.C.B. Gopinath, Z.H. Ismail, M.K. Md Arshad, P. Poopalan, Aptasensing nucleocapsid protein on nanodiamond assembled gold interdigitated electrodes for impedimetric SARS-CoV-2 infectious disease assessment., Biosensors & Bioelectronics. 197 (2022) 113735. https://doi.org/10.1016/j.bios.2021.113735.

[184] M. Amouzadeh Tabrizi, P. Acedo, An Electrochemical Impedance Spectroscopy-Based Aptasensor for the Determination of SARS-CoV-2-RBD Using a Carbon Nanofiber–Gold Nanocomposite Modified Screen-Printed Electrode, Biosensors. 12 (2022) 142. https://doi.org/10.3390/bios12030142.

[185] M.A. Ali, C. Hu, F. Zhang, S. Jahan, B. Yuan, M.S. Saleh, S.-J. Gao, R. Panat, N protein-based ultrasensitive SARS-CoV-2 antibody detection in seconds via 3D nanoprinted, microarchitected

array electrodes, Journal of Medical Virology. 94 (2022) 2067–2078. https://doi.org/10.1002/jmv.27591.

[186] A. Raziq, A. Kidakova, R. Boroznjak, J. Reut, A. Öpik, V. Syritski, Development of a portable MIP-based electrochemical sensor for detection of SARS-CoV-2 antigen., Biosensors & Bioelectronics. 178 (2021) 113029. https://doi.org/10.1016/j.bios.2021.113029.

[187] S. Mahari, A. Roberts, D. Shahdeo, S. Gandhi, eCovSens-Ultrasensitive Novel In-House Built Printed Circuit Board Based Electrochemical Device for Rapid Detection of nCovid-19 antigen, a spike protein domain 1 of SARS-CoV-2, BioRxiv. (2020) 2020.04.24.059204. https://doi.org/https://doi.org/10.1101/2020.04.24.059204.

[188] A.M. Atta, G.A. El-Mahdy, H.A. Al-Lohedan, Corrosion inhibition efficiency of modified silver nanoparticles for carbon steel in 1 M HCL, International Journal of Electrochemical Science. 8 (2013) 4873–4885.

[189] M. Beikmohammadi, L. Fotouhi, A. Ehsani, M. Naseri, Potentiodynamic and electrochemical impedance spectroscopy study of anticorrosive properties of p-type conductive polymer/TiO2 nanoparticles, Solid State Ionics. 324 (2018) 138–143. https://doi.org/10.1016/j.ssi.2018.06.018.

[190] F. Fekri, M. Shahidi Zandi, M.M. Foroughi, Polypyrrole coatings for corrosion protection of Al alloy2024: influence of electrodeposition methods, solvents, and ZnO nanoparticle concentrations, Iranian Polymer Journal (English Edition). 28 (2019) 577–585. https://doi.org/10.1007/s13726-019-00726-2.

[191] M. Menkuer, H. Ozkazanc, Anticorrosive polypyrrole/zirconium-oxide composite film prepared in oxalic acid and dodecylbenzene sulfonic acid mix electrolyte, Progress in Organic Coatings. 147 (2020) 105815. https://doi.org/10.1016/j.porgcoat.2020.105815.